MEASUREMENTS OF MAGNETIC FIELD FLUCTUATIONS IN THE CALTECH RESEARCH TOKAMAK

Thesis by

Mark Allen Hedemann

In Partial Fulfillment of the Requirements

for the Degree of

Doctor of Philosophy

California Institute of Technology

Pasadena, California

1982

(Submitted July 28, 1981)

ACKNOWLEDGEMENTS

I wish to express my thanks and appreciation to my advisor, Dr. Roy W. Gould, for his suggestions leading to this research topic and for his help and encouragement during the course of this study. I acknowledge also many useful discussions on theory and experimental background with Dr. Paulett C. Liewer and Dr. Stewart J. Zweben.

I gratefully acknowledge the many direct and indirect contributions of Dr. Bruce S. Levine, with whom it was a distinct pleasure to work, and Eric D. Fredrickson, whose willingness to help is greatly appreciated. I sincerely thank Amy Wendt for her many hours spent with the computer analyzing the data. I am indebted to Frank Cosso for his circuit designs and troubleshooting skills as well as his tutorials on electronics. I also thank Glenn J. Greene for his work which enhanced the operation of the tokamak.

I cannot properly thank my parents, Lester and Elizabeth, for giving me the freedom to chart the course I chose in life. I reserve my greatest thanks for my wife Kathy. Her continued love, patience, and support can never be repaid. Finally, I thank my son Stephen, whose arrival inspired me to accelerate my work.

ABSTRACT

An experimental investigation of magnetic field fluctuations in a research tokamak plasma has been performed. The fluctuations were measured with movable probes inserted directly into the plasma. Estimates of the fluctuating field strength, power spectral density, and correlation lengths have been made by calculations on the raw data. The fluctuations were found to be of comparable strength for the radial and poloidal components, while the toroidal component was found to be at least a factor of 5 weaker in strength. The fluctuating field strength showed no apparent dependence on plasma current and safety factor at the edge, but increased with electron density during gas puffing and as the minor radius of measurement was decreased.

The power spectral density indicated that the fluctuations could be divided into two frequency regions. The low frequency region ($f<100$ kHz) was dominated by coherent MHD modes with correlation lengths on the order of the tokamak size. The high frequency ($f>100$ kHz) region appeared to be turbulent in nature with short correlation lengths in the poloidal direction ($<.01$m), but longer correlation lengths in the radial direction ($>.04$m). The high frequency region showed a roll-off in frequency of δB_r of approximately $f^{-2.5}$.

The results are compared with theories of fluctuation sources and the effects of fluctuations on

anomalous electron thermal transport. The best fit to the high frequency region spectral density is given by a statistical theory of fluctuations. The fluctuating field strength appears to be more than an order of magnitude too small to account for the anomalous electron thermal transport using stochastic field theory.

TABLE OF CONTENTS

I. INTRODUCTION

The tokamak is one of the leading magnetic confinement devices in fusion research. One can view the tokamak as a toroidal magnetic container for a plasma requiring the simultaneous presence of three magnetic fields. The first is a poloidal field (figure 1) produced by a toroidal current flowing in the plasma (I_p). As with any current carrying conductor, the Lorentz force due to the interaction of the current and the magnetic field it produces is inwardly directed everywhere on the plasma surface, thus confining the plasma. The current in the plasma is induced by transformer action. The loop of plasma is the secondary of the transformer whose primary coil is called the Ohmic heating coil, since the current in the plasma serves not only to confine the plasma, but also to heat it through Ohmic losses. With this single field, however, the confinement is not stable, as an analysis of simple perturbations can show.

As an example of such a perturbation, consider a situation in which the current channel shrinks slightly at one location (figure 2a). The poloidal field at the surface of the plasma is inversely proportional to the plasma channel radius, so that the field at the point of perturbation is stronger, providing a stronger Lorentz force. This reinforces the perturbation, which will grow until the plasma channel pinches off. This is often called the "sausage" instability. Another example is the

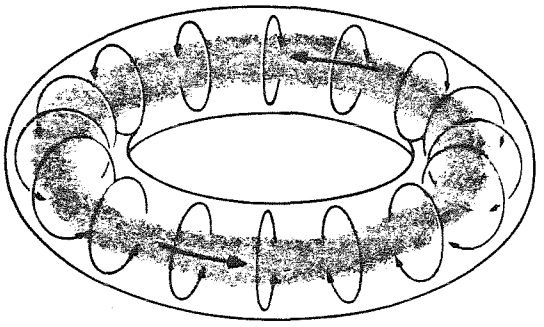

Figure 1. The poloidal magnetic field produced by a toroidal current (from Bishop [1], p.23).

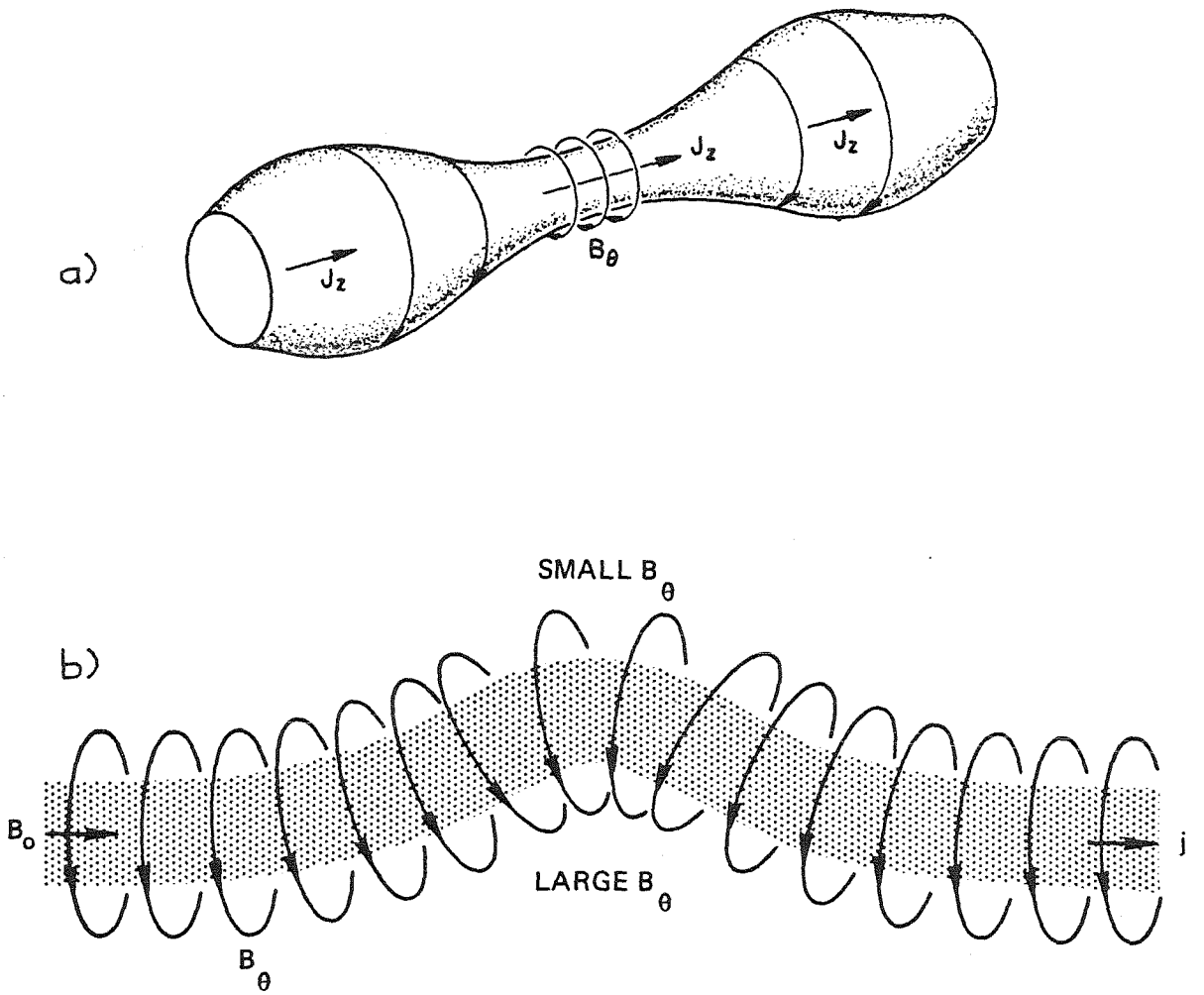

Figure 2. a) The "sausage" instability (from Bateman [2], p.105), and b) the "kink" instability (from Chen [3], p. 286).

so-called "kink" instability (figure 2b). It arises from a perturbation in which the plasma bends outward at some point. Due to the curvature of the current channel, the field, and hence the Lorentz force, is weakened on the outside of the bend and strengthened on the inside of the bend. This serves to reinforce the perturbation, and the kink grows.

The second field of a tokamak is needed to prevent the growth of these instabilities. It is parallel to the plasma current and is called the toroidal field. Since the plasma is a good conductor, fluid motion perpendicular to the toroidal field tends to drag the field lines of force along (the field lines would be "frozen in" in a perfectly conducting fluid)[2]. Provided that this toroidal field is strong enough, its resistance to compression or stretching of field lines is sufficient to stabilize the instabilities due to the poloidal field.

In the presence of these two fields, the plasma still has a tendency to expand outward in major radius. Due to the toroidal shape of the plasma current, the poloidal field is sufficiently stronger on the inside portion of the torus than on the outside to produce a net outward force on the plasma. The third field, called the equilibrium field or vertical field, since the plane of the torus is normally horizontal, serves to weaken the poloidal field on the inside of the torus and strengthen it on the outside of the torus, thus balancing the force on the

plasma. A portion of this field is normally produced by currents induced by the plasma current in the conducting walls of the containment vessel. The remainder is produced by an external coil producing a curved field (figure 3a) whose main component is vertical. The horizontal components serve to restore the current channel to its equilibrium position by $\underset{\sim}{J} \times \underset{\sim}{B}$ forces if the column drifts upward or downward. These three fields -- poloidal, toroidal, and vertical -- form a nested set of closed magnetic field surfaces.

In the presence of these three fields, one should be able to predict how well the plasma particles and energy are confined by the tokamak. Fusion plasmas of interest consist of fully ionized isotopes of hydrogen. In tokamak plasmas produced to date, only a small fraction of the particles are neutral particles, so that the majority of particles are confined by the magnetic field. Impurity concentrations are kept low to prevent loss of energy by radiation from partially ionized species. Temperature and density profiles typically peak at the center of the discharge. Energy can flow by conduction to the walls due to the temperature gradient. However, because of the density gradient, energy confinement is limited by the diffusion of particles to the wall, so that an understanding of the limit to energy confinement in tokamaks can be obtained by understanding the transport of charged particles across the closed magnetic field

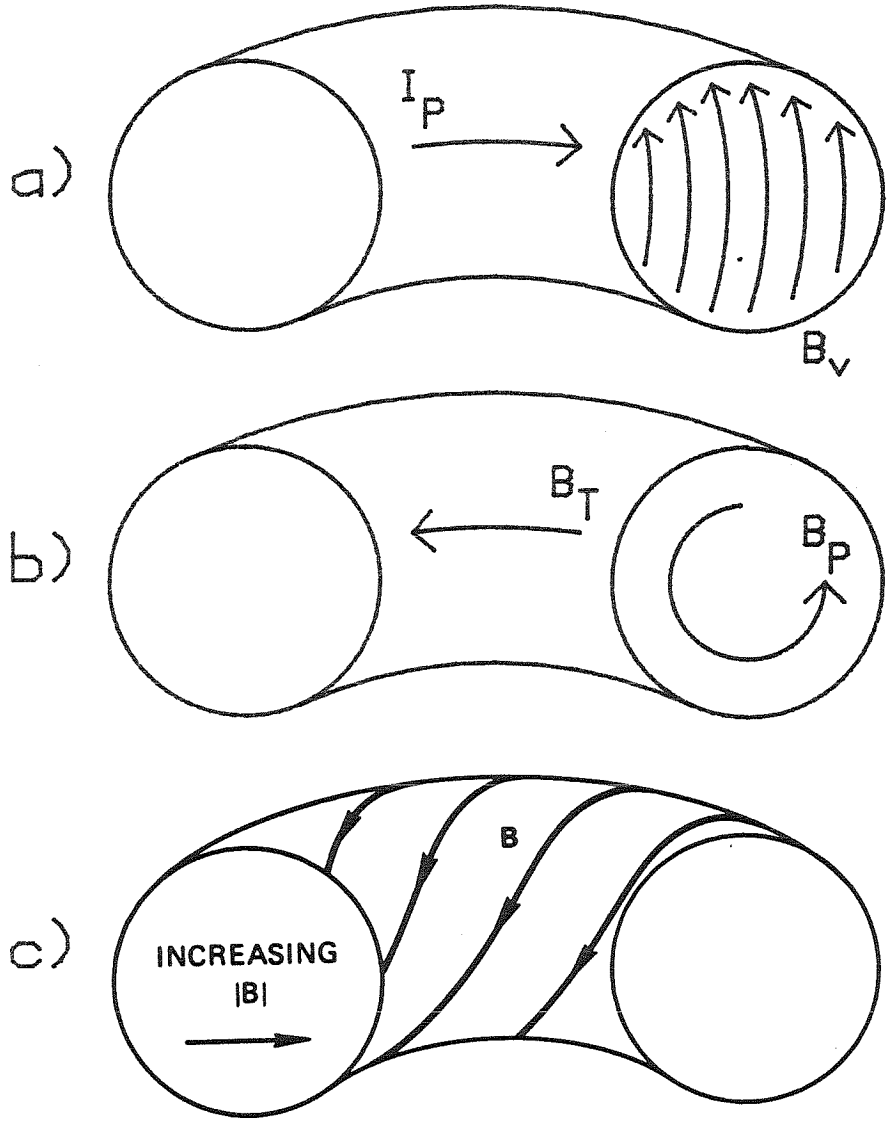

Figure 3. a) The vertical field, b) the toroidal and poloidal fields, and c) the twisting field pattern arising from the combination of fields (from Chen [3], p. 172).

surfaces.

A charged particle in a uniform magnetic field is free to move parallel to the lines of magnetic field, but experiences a Lorentz force,

$$\underset{\sim}{F} = Ze\underset{\sim}{v} \times \underset{\sim}{B} \qquad (1.1)$$

when moving perpendicular to the field lines. No energy is gained or lost by the particle since the force is perpendicular to the direction of motion. Thus, the projection of the particle orbit on a plane perpendicular to the magnetic field is a circle whose radius, called the Larmor radius, is given by:

$$\rho_L = |mv_\perp / ZeB| \qquad (1.2)$$

where m is the particle mass, $v_\perp$ is the magnitude of its perpendicular velocity, Ze is its charge, and B is the magnetic field strength. The center of this orbit is referred to as the guiding center. The particle orbit will remain centered on the same magnetic field line until the particle experiences a collision with another particle. After the particle has collided, it will again move in an orbit whose projection on a plane perpendicular to the field is a circle, but this orbit will be centered on another field line. In this manner the particle can move across the field lines. One can estimate a diffusion coefficient for this process as being of order [4]

$$D_k \sim \nu_k \rho_L^2 \qquad (1.3)$$

where ρ_L is the radius of the particle orbit and ν_k is the Braginskii 90 degree collision frequency given

by

$$\nu_i = (n_i e^4 \ln\Lambda)/[12\varepsilon_o^2 m_i^{1/2}(\pi k T_i)^{3/2}] \qquad (1.4a)$$

for the ions, or

$$\nu_e = (n_e e^4 \ln\Lambda)/[6\varepsilon_o^2 (2m_e)^{1/2}(\pi k T_e)^{3/2}] \qquad (1.4b)$$

for the electrons, where $n_{i(e)}$ is the particle density, e is the unit electronic charge, $m_{i(e)}$ is the particle mass, and $T_{i(e)}$ is the average particle temperature [5]. Here Λ is the Coulomb scattering cross-section [4]

$$\Lambda = (12/Ze^3)(\pi^2 k^3 T_e^3 \varepsilon_o^2/n_e)^{1/2} \qquad (1.5)$$

In a tokamak, however, one does not have a uniform field in which the particles reside. In particular, the combination of toroidal, poloidal, and vertical fields gives rise to field lines which twist as one follows them around the torus (figure 3c). The strength of the field varies as the inverse of the major radius, so that the strength of the field varies as one follows a field line around the torus. Figure 4a shows a particle moving along a field line in its Larmor orbit approaching a region of higher field strength. In this transition region, there is a component of field directed inwardly which, coupled with the motion of the particle, produces a Lorentz force which will give an acceleration of the particle toward the low field region. This can also be viewed as a transfer of parallel motion velocity into perpendicular motion velocity as the total energy of the particle remains constant. One can define the magnetic moment [3]

$$\mu = mv_\perp^2/2B \qquad (1.6)$$

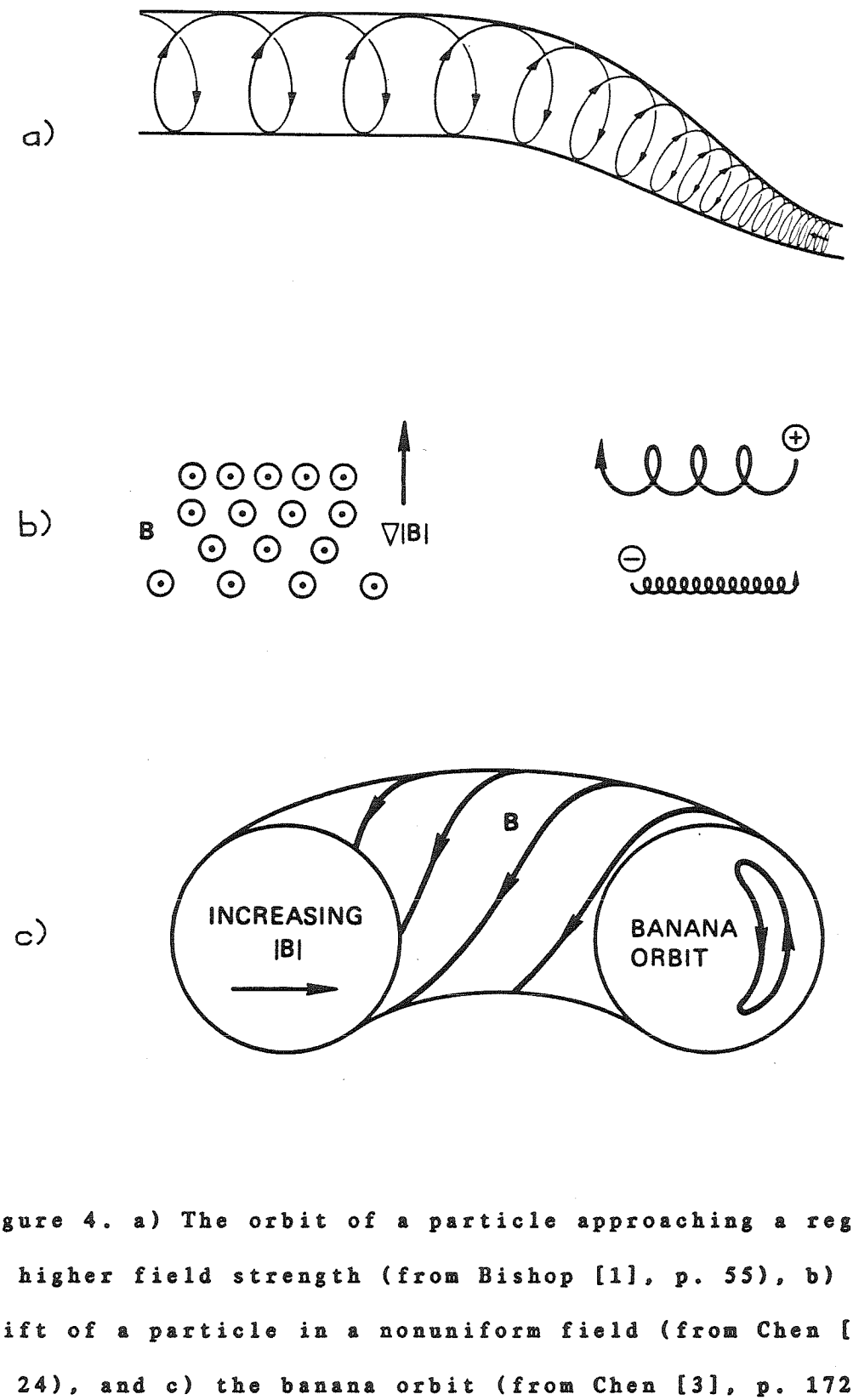

Figure 4. a) The orbit of a particle approaching a region of higher field strength (from Bishop [1], p. 55), b) the drift of a particle in a nonuniform field (from Chen [3], p. 24), and c) the banana orbit (from Chen [3], p. 172).

and show that it is a constant of the motion, so that as the particle enters the stronger field region, $v_\perp$ increases and $v_\parallel$ decreases since $v_\perp^2+v_\parallel^2$ is also a constant. If B_m is the maximum field strength along the line of force, and the particle starts in a region of field strength B_0 with $v_{\perp 0}$ and $v_{\parallel 0}$, it will be reflected as it travels along the line of force if

$$(v_{\perp 0}^2+v_{\parallel 0}^2)/v_{\perp 0}^2 < B_m/B_0 \qquad (1.7)$$

If a collection of particles whose velocities initially are isotropically distributed in velocity space start in a weak field region of field strength B_0, then a fraction of these particles equal to

$$f = (1-B_0/B_m)^{1/2} \qquad (1.8)$$

will be reflected when entering a strong field region with maximum field strength B_m. In a tokamak, then, a fraction of the particles will be trapped in mirror fields rather than continue to move around the torus along field lines. Since the toroidal field, B_T, is proportional to $1/R$, then

$$B_0/B_m \cong (R-r)/(R+r) \qquad (1.9)$$

where r is the minor radius of the field line, and $f \cong (2r/R)^{1/2}$ if r is small compared to R.

The fact that the toroidal field in a tokamak has an inwardly directed gradient gives rise to another effect on the motion of particles. Since the Larmor radius is inversely proportional to the field strength, the orbit radius will be smaller on the inside portion of the orbit

than on the outside (figure 4b). Averaged over the orbit, the particle has a net motion of the guiding center in the direction mutually perpendicular to the field and the field gradient. The velocity of this guiding center drift is given by

$$v_{\nabla B drift} = \pm(v_\perp \rho_L / 2B^2) \underset{\sim}{B} \times \underset{\sim}{\nabla} B \qquad (1.10)$$

where the sign denotes the charge of the particle.

Figure 4c shows the projection of the motion of the guiding center for a trapped particle in a tokamak on a single azimuthal plane, taking into account the gradient drift. From the shape of the projection, this has become known as a banana orbit. The width of the orbit at the midplane is approximately

$$\Delta r \cong (r/R)^{1/2} \rho_L B_T / B_\theta \qquad (1.11)$$

where B_θ is the poloidal field. Hence, for a fraction of the particles, the effective step size in a collision leading to diffusion across the toroidal field is of the order of Δr rather than ρ_L, which is in general smaller. If collisions are infrequent enough so that the trapped particles trace out many banana orbits between collisions, then the diffusion coefficient is enhanced by a factor [5]

$$(R/r)^{3/2} q^2 \qquad (1.12)$$

where $q=q(r)=rB_T/RB_\theta$, and ranges from a value of 1 to 4 over the cross-section of a typical tokamak discharge (q is called the "safety factor," since it is a measure of the relative stiffness of the toroidal field and its ability

to prevent the instabilities previously mentioned). This is called the neoclassical "collisionless" or "banana" regime, with a diffusion coefficient of

$$D \sim \nu \rho_L^2 q^2 (R/r)^{3/2} \qquad (1.13)$$

It is of interest at this point to compare neoclassical theory with experimental results obtained in tokamaks for the electron energy confinement time. Figure 5 shows such a comparison for the Alcator tokamak. Only at high densities are the theory and experiment approaching agreement. There is also a disagreement between experiment and theory on the dependence on density. The dependence on density in neoclassical theory enters in the diffusion coefficient through the collision frequency where D is proportional to n_e (ignoring a mild dependence on n_e in $\ln\Lambda$). This would predict an energy confinement time (assuming no radiation losses -- energy is carried out with the particles) proportional to $1/n_e$. Experiments on various tokamaks as illustrated by the Alcator results show confinement time roughly proportional to $\bar{n}_e$, where $\bar{n}_e$ is the average density along a minor diameter of the plasma. Various scaling laws have been developed to show the connection between experimentally measured tokamak parameters. One of these, the Alcator scaling law, shows the relationship between plasma density, size, and confinement, to be [6]

$$\tau_E = 6 \times 10^{-21} \bar{n}_e a^2 \qquad (1.14)$$

where τ_E is the energy confinement time and a is the

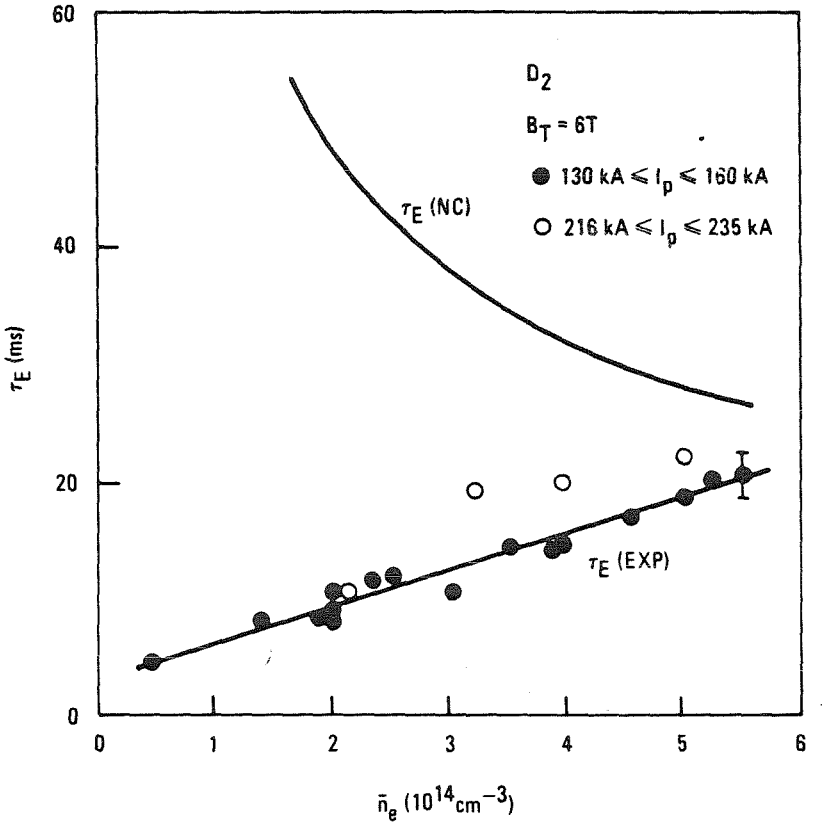

Figure 5. The variation of τ_E with line average density compared with the neoclassical prediction for Alcator (from Gondhaleker [7]).

minor radius of the plasma.

A crude estimate can be made of neoclassical energy confinement and experimentally observed confinement in the Caltech Research Tokamak (BIGMAK, whose parameters are discussed in chapter 2). If D is the diffusion coefficient, then the energy confinement time will be of order L^2/D where L is some characteristic length of the system. Using half the minor radius as a characteristic length, so that r = a/2, and using an estimate of D at that radius as the characteristic diffusion coefficient, the neoclassical energy confinement time in BIGMAK is approximately .5 seconds.

Experimentally, the energy confinement time can be estimated as

$$\tau_E \sim E / (dE/dt) \qquad (1.15)$$

where E is the total contained energy in the plasma, and dE/dt represents the power lost from the plasma. An estimate for the power lost can be obtained from a measurement of the input power at a time when $dI_p/dt=0$. If, at that time, the plasma profile and position are not changing significantly, then one can assume that the input power is in balance with the output power and is not being used to change the inductive energy of the plasma. Under these assumptions, an estimate of the confinement time in BIGMAK gives $\tau_E \sim .3$ msec. This is consistent with Alcator scaling, $\tau_E \sim .27$ msec, but is three orders of magnitude less than neoclassical theory would predict.

This discrepancy is common to all tokamaks, and indicates that some other mechanism is responsible for the rates of energy transport observed.

A great deal of theoretical work has been done in order to explain this observed anomalous transport as resulting from small perturbations in the magnetic fields [8-22]. Much work has also been done in order to explain the origin of such perturbations if they exist [14-25]. If these perturbations lead to stochastic field regions, then diffusion of particles and the energy they carry across the field lines can be significantly enhanced above the neoclassical prediction. One way to visualize a stochastic field region is to consider two field lines which are close to each other and to follow these field lines around the torus several times. In a stochastic field region, these lines will diverge from each other, even if they begin arbitrarily close to each other. Rather than forming a set of closed, nested magnetic surfaces, the field lines now wander in a random walk fashion in radius while transiting the machine in the toroidal direction. In a stochastic field region, an individual field line can eventually wander from the center of the machine to the wall. Such field regions can arise quite easily in tokamaks from the overlapping of saturated large-scale instabilities or from the simultaneous presence of many microinstabilities [8, 9, 10, 14, 18, 26]. Estimates of the strength of perturbations needed to produce stochastic field regions show that the

perturbation field strength is small. Perturbations of order

$$|\delta B_r/B_T| \cong 10^{-4} \qquad (1.16)$$

where δB_r is the root mean square perturbation field strength, are sufficient to produce the cross-field transport seen in tokamaks [10]. Although it may be difficult to understand how such small perturbations can lead to such large particle and energy losses compared to neoclassical theory, one should consider that particle mobility along field lines is very great compared with mobility across field lines. In neoclassical theory, particles depend on collisions in order to diffuse across the field, so that $D_\perp$ is proportional to n. In the stochastic field theory, the diffusion across the field is produced by particles free-streaming along the field lines while the field lines make small radial excursions. Hence, D is proportional to $D_\parallel \sin^2\theta$, where $\sin\theta = \delta B_r/B_T$, and $D_\parallel$ is the diffusion coefficient along the field lines. Note that $D_\parallel$, in contrast to $D_\perp$, is limited by, rather than being dependent on, collisions, and so is inversely proportional to n. Typically $D_\parallel$ is many orders of magnitude greater than $D_\perp$, so that D can be much greater than $D_\perp$ even if $|\delta B_r/B_T|$ is small. One can also see that this form of D gives a confinement time proportional to n (ignoring any dependence of $\delta B_r/B_T$ on n), which is in agreement with experiments.

The explanation of anomalous transport by magnetic field perturbations can be seen in a simple random walk model. One can envision particles freely streaming along field lines, but taking "steps" at a characteristic frequency ν. This frequency may be the collision frequency for the particles, at which time the trajectories are randomly altered. This frequency may also be the frequency associated with the correlation length for fluctuations in a stochastic field region, that is, the inverse of the time it takes a free streaming particle to travel a correlation length. For each step, then, a particle will travel a distance $z=v_{th}/\nu$ along the field line and a distance $s=z(\delta B_r/B_T)$ radially on the average. Using half the minor radius as a characteristic length a particle must walk to leave the plasma, a particle on average must take N steps where $a/2 = N^{1/2}s$. The confinement time is simply $\tau_E = N/\nu$ which becomes

$$\tau_E = \nu a^2/4v_{th}^2(\delta B_r/B_T)^2 \qquad (1.17)$$

Estimating τ_E from typical BIGMAK parameters, using the electron collision frequency as an estimate of ν, and the electron thermal speed for v_{th}, one finds a fluctuating field strength of

$$|\delta B_r/B_T| \tilde{=} 3 \times 10^{-4} \qquad (1.18)$$

is sufficient to explain the observed confinement time. It is of interest to note that using the collision frequency in this estimate gives τ_E proportional to $\bar{n}_e a^2$ -- Alcator scaling. This also introduces a

strong temperature dependence ($T_e^{-5/2}$), but the dependence of τ_E on T_e is thought to be much weaker.

Although much theoretical work has been done in the area of magnetic field fluctuations and anomalous transport, very few measurements of fluctuations have been made. In this thesis, measurements of magnetic field fluctuations on BIGMAK will be presented.

II. EXPERIMENTAL APPARATUS

A. Vacuum Chamber

The measurements presented in this thesis were all made on BIGMAK. The plasma resides within a toroidal stainless steel vacuum chamber with a major radius of .46 m and a minor radius of .15 m. Unlike many other tokamaks, there is no limiter for the plasma current channel within the chamber. The major axis of the torus is vertical. The port access to the vacuum chamber is rather limited. In the midplane of the torus is a vertical port of width .051 m and height .102 m. This port is used exclusively for the pumping system for the torus. Also in the midplane are 4 vertical ports .025 m wide and .102 m high 45°, 115°, 180°, and 285° away from the pumping port. A pair of .013 m diameter ports in the midplane view the center of the vacuum chamber tangentially 180° away from the pumping port. These ports are all on the outside rim of the torus. A pair of .013 m diameter ports, one at the pumping port location and one 180° away, are also present on the inside of the chamber. A pair of .025 m x .038 m rectangular ports are located on the top and bottom of the chamber 285° away from the pumping port for the microwave interferometer antennae. Pairs of .025 m diameter ports are located on the top and bottom of the chamber at the location of the pumping port as well as 45°, 75°, 115°, and 180° away.

The chamber is kept under vacuum by a

Leybold-Heraeus Turbovac 450 turbomolecular pump. This type of pump was chosen because of the high pumping rates for all gases except hydrogen, thus limiting the impurity concentrations in the chamber. Typical base pressures obtained are near 10^{-7} torr. The high pressure side of the turbomolecular pump is itself pumped on by a Leybold-Heraeus model D60A forepump vented to the atmosphere. Hydrogen gas used to fill the chamber for plasmas is leaked into the foreline between the two pumps. A zeolite trap is also located in the foreline to help minimize the back flow of oil impurities into the chamber.

B. Field Coils and Power Supplies

The toroidal field coil is wound directly on the vacuum chamber and consists of 480 turns of #1/0 gauge, 600 volt insulated copper wire of type MTW/THHN/THWN. The coil is energized from a 4.8 mF, 10 kV rated capacitor bank. The bank is charged by a Universal Voltronics power supply and is fired into the coil through ignitron switches. The quarter cycle time of the bank and coil combination, $t_{qc} = (\pi/2)(LC)^{1/2}$, is 9.55 msec. A voltage sensing circuit triggers an ignitron to short the capacitor bank when its voltage drops to zero. The current in the winding, and resulting field, then decay with an L/R time, $t_{L/R}$, of approximately 35 msec.

Systematic errors in the winding of the toroidal field coil led to a non-toroidal error field in the vacuum

chamber. A coil to correct this error field was designed in the following manner. Twelve one-turn toroidal loops of wire, evenly spaced poloidally, were wound at a minor radius of .30 m, the closest easily accesible location. The induced voltage for each loop was measured when the toroidal field was fired, this voltage being proportional to the net error flux through the loop. The toroidal field coil was then modelled as consisting of a perfect toroidal winding with no error field and a small number of toroidal currents at the minor radius of the winding whose net toroidal current was zero. A trial and error procedure of adjusting the number of currents, their position, and their relative strength produced a good fit to the experimentally measured error fluxes. The model then gave the error field strength and direction at every point in the vacuum chamber, and a correction coil was easily designed to match the field pattern. The error field was found to be nearly horizontal, so that the correction coil will be referred to in this thesis as the horizontal field coil. This coil is connected in series with the toroidal field coil. A trimming coil providing approximately 15 percent of the error correction produces the same field pattern, but is powered from a Hewlett-Packard model 6453A direct current power supply.

The effects of the horizontal field coil are dramatic. Without the correction coil, the plasma discharge obtains a maximum current of 5 kA and a maximum

duration of 2 msec. Discharges with currents to 30 kA and 20 msec in duration are easily obtained with the correction coil connected.

The ohmic heating winding consists of 40 toroidal turns of #1 gauge wire all at a minor radius of .28 m. The poloidal spacing of the windings minimizes to a large degree the flux in the vacuum chamber. This was accomplished using the following design procedure. First the coil was modelled by several toroidal currents near the center of the vacuum chamber whose position and strength were varied until a nearly toroidal flux surface was produced with a minor radius the same as the actual coil. In the model the toroidal currents were then replaced by a sheet of toroidal current on the toroidal flux surface, with the strength of the sheet current everywhere proportional to the field strength previously produced by the individual toroidal currents. The fields outside the sheet current were unchanged, but the field inside went to zero, which can be shown by application of Ampere's law. In moving from the model to the actual coil, the sheet current was replaced by 40 discrete turns whose winding density was proportional everywhere to the sheet current strength. In this approximation to the model, the maximum field strength from the coil in the vacuum chamber was found to be less than one percent of the field strength on the toroidal axis at the equatorial plane.

The ohmic heating winding is energized by three

different capacitor banks. The first, called the preionization bank, has 1 μF of capacitance and is charged to approximately 8 kV. This bank is fired 1.1 msec before the actual tokamak discharge through an ignitron switch. This circuit is highly underdamped with a characteristic oscillation frequency of approximately 6 kHz. The neutral gas in the chamber has a small number of free electrons which are accelerated by this oscillating field and produce more free electrons by collisions with neutral atoms. This supply of electrons is augmented by electrons from a tungsten filament located in one of the ports of the vacuum chamber. The filament is biased to approximately -10 V with respect to the vacuum chamber. With this larger number of free electrons present, the second bank, called the ohmic heating fast bank, is fired, defining the beginning of the tokamak discharge. The fast bank has a capacitance of 432 μF and is typically charged to 1.2 kV. As this bank discharges, the electrons see an accelerating voltage in one direction only, and through collisions with neutral atoms, the gas is fully ionized. When the fast bank voltage reaches zero, the third bank, called the ohmic heating slow bank, is fired. This occurs approximately .7 msec into the discharge. The slow bank has 208 mF of capacitance and is typically charged to 330 V. It is designed to keep the induced voltage in the plasma positive as long as practical, thus maintaining the discharge. Typically the induced voltage remains positive for 10 msec,

while the discharge continues for up to 22 msec.

The vertical field winding consists of 40 toroidal turns of #1 gauge wire all at a minor radius of .27 m, with the 20 turns toward the inside of the chamber wound in the opposite sense to the 20 turns toward the outside of the chamber. The field produced by the coil has some curvature such that the field index at the center of the vacuum chamber, $(R/B_V)(dB_V/dR)$, is equal to $-.5$. This curvature gives rise to appropriately directed horizontal components of the field such that the interaction of the plasma current with the field always produces a vertical restoring force toward the center of the vacuum chamber.

The vertical field winding is energized by a two capacitor bank power supply. The first bank, called the vertical field fast bank, has 1.92 μF of capacitance and is typically charged to 130 V. It is fired through an SCR switch at the same time as the ohmic heating fast bank. The second bank, called the vertical field slow bank, has 396 μF of capacitance and is typically charged to 50 V. It is held off from the circuit by a diode, and takes over when the fast bank voltage drops to the value of the slow bank voltage. The fast bank can be thought of as establishing the current in the winding while the slow bank maintains the current throughout the discharge. As much as half of the current in the vertical field winding, however, is induced by the current in the plasma. The capacitances of the two banks have been trimmed so that, under normal

operating conditions, the current waveform in the winding roughly tracks the current waveform in the plasma, thus maintaining a reasonable equilibrium. A cross-section of the various field coils is shown in figure 6.

C. Diagnostics

Pressure in the vacuum chamber is monitored by a Bayard-Alpert gauge controlled by a Veeco model APC-110 gauge controller. Such gauges will measure pressures from 10^{-9} torr to approximately $5x10^{-4}$ torr. The gauge and controller are calibrated for use in nitrogen. All readings in hydrogen must be divided by a correction factor. Reported measurements of its value vary from .38 to .46. Due to this small discrepancy, all pressures quoted in this thesis will be uncorrected values unless otherwise specified.

The composition of the gas in the vacuum chamber is monitored by a Varian model 978-1000 quadrupole gas analyzer (QGA). After the hydrogen peak at mass number 2, the most prominent peak in the mass spectrum under normal conditions is at mass 18, which is assumed to be water vapor. Peaks are also seen at masses 14, 15, 16, 17, 19, and 28. Mass 28 is assumed to be molecular nitrogen. The others are assumed to be various combinations of hydrogen, oxygen, carbon, and nitrogen. Severe leaks in the vacuum chamber can cause mass 28 to dominate. If pump oil contamination occurs from the foreline, this can be seen by

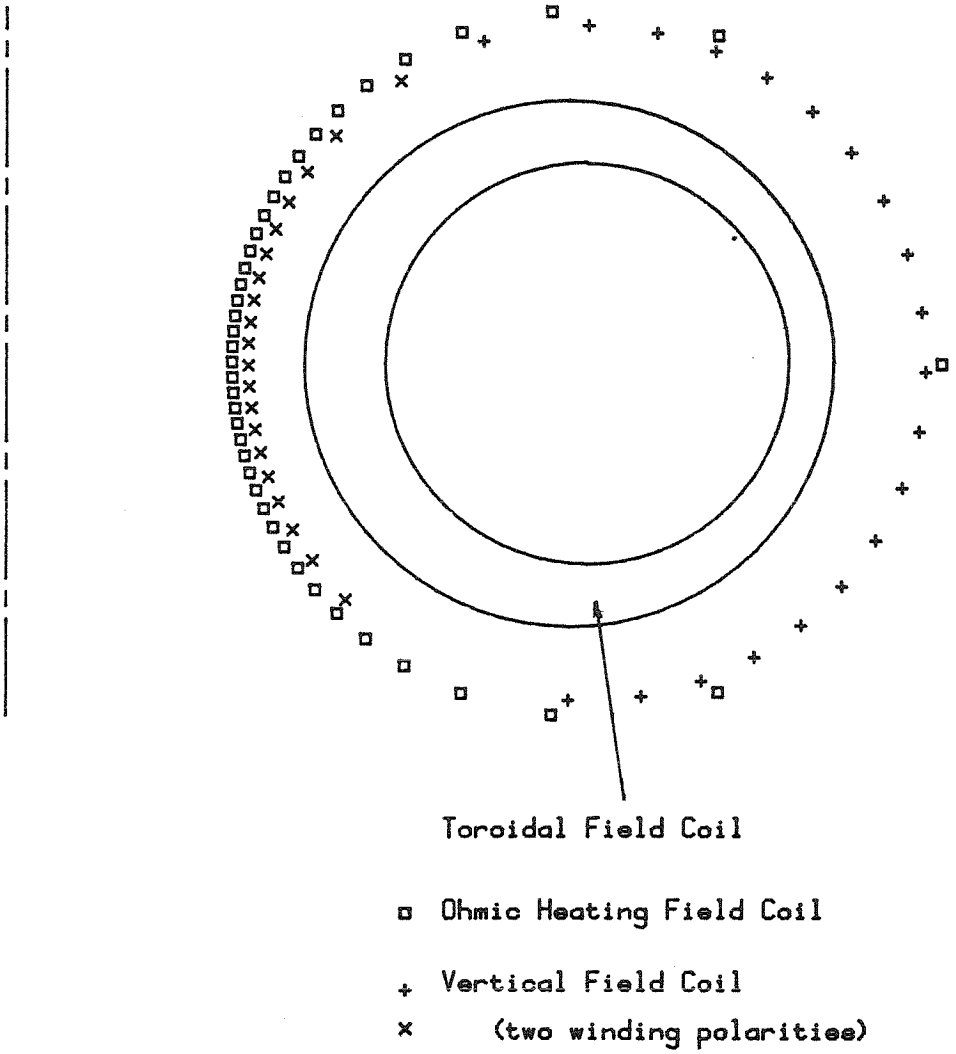

Figure 6. A cross-section of the toroidal field coil, the ohmic heating field coil, and the vertical field coil.

the appearance of peaks in the mass range of 35 to 100.

The plasma current can be monitored by the use of a Rogowski coil (figure 7). The Rogowski coil on the Caltech tokamak is a simple uniform toroidal winding with approximately 1200 turns, a major radius of .22 m, and a minor radius of 8 mm. It is mounted on the vacuum chamber so that the plasma current flows along its central axis. Current in the plasma produces poloidal flux linking the turns of the Rogowski coil. The change in flux as the plasma current changes produces a voltage at the coil leads proportional to dI_p/dt. This is electronically integrated to monitor the plasma current as a function of time. The integrator gain is adjusted to produce .5 V signal for each kiloampere of plasma current. Smaller Rogowski coils are also used to measure the current flowing in each of the field windings on the tokamak.

Similar coils whose winding density is roughly proportional to sin θ or cos θ, where θ is the poloidal angle, are used to monitor the horizontal or vertical position of the plasma in the chamber. These are called the in-out and up-down coils respectively. Since the in-out coil is designed to monitor horizontal changes in the plasma position, it is also very sensitive to the vertical field. This effect is compensated for electronically when the signal is integrated by subtracting a signal proportional to the vertical field strength from the in-out signal. Both coils also have electronic

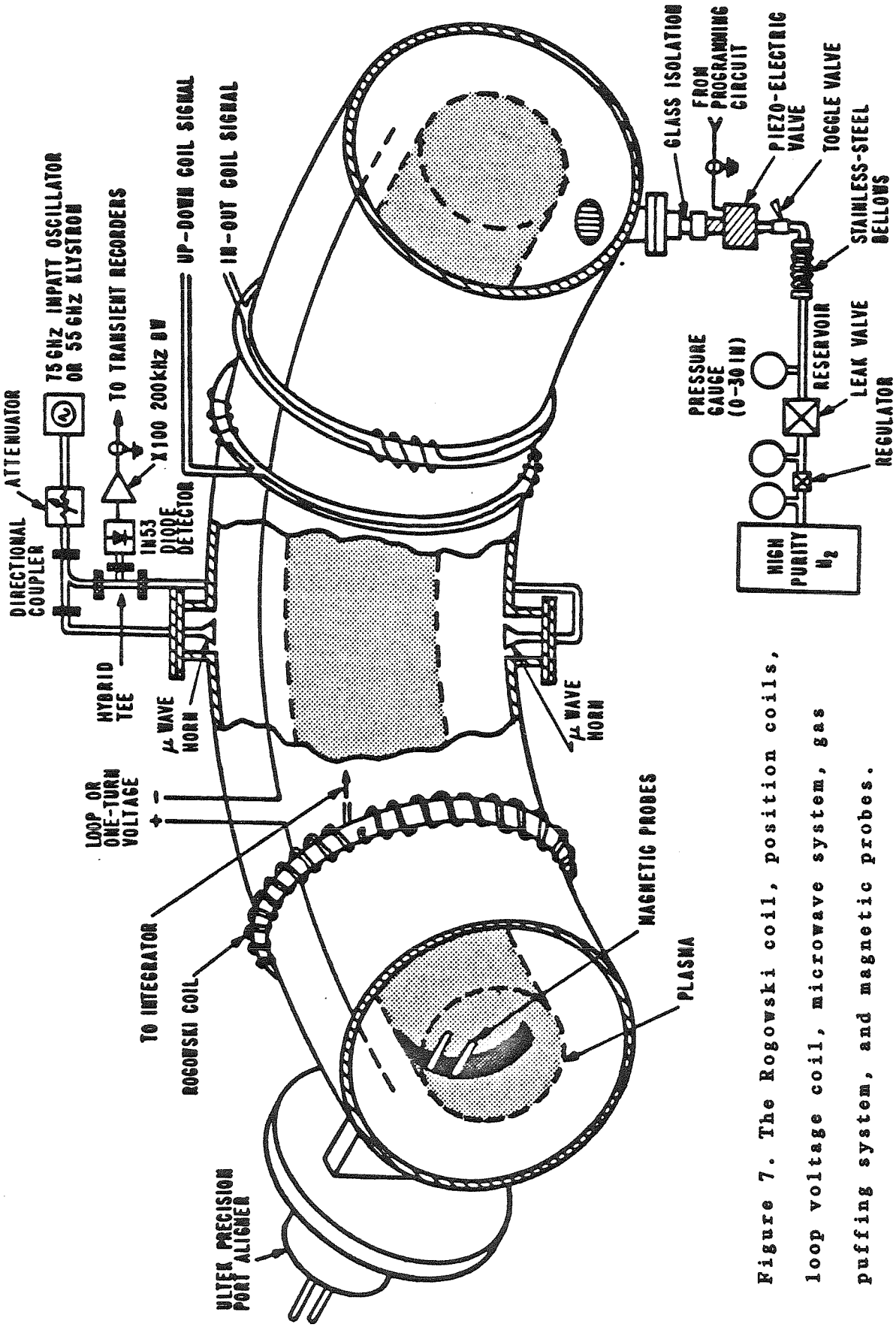

Figure 7. The Rogowski coil, position coils, loop voltage coil, microwave system, gas puffing system, and magnetic probes.

compensation for stray pickup of the loop voltage and toroidal field since their sensitivity to these is greater than that of the Rogowski coil. Since the signals are proportional to the plasma current, the integrated signals are divided electronically by I_p. The integrator gains are adjusted to produce .1 V signal for each centimeter of horizontal or vertical deflection.

The one-turn voltage, or loop voltage, seen by the plasma is monitored by a single toroidal loop of wire at a minor radius of .22 m and 30 degrees above the midplane on the inside of the torus. This coil encloses nearly the same ohmic heating coil flux as the plasma. Instruments with high input impedance (1 MΩ) are used to measure the voltage on this coil.

A microwave interferometer operating at 75 GHz with 4 mm waveguide is used to measure the line average density along a vertical diameter of the plasma. For electromagnetic waves propagating in a plasma with the electric field parallel to the static magnetic field, the dispersion relation is [4]

$$\omega^2 = \omega_{pe}^2 + k^2c^2 \qquad (2.1)$$

where

$$\omega_{pe}^2 = (n_e e^2)/(\varepsilon_o m_e) \qquad (2.2)$$

is the square of the electron plasma frequency. At a fixed ω, k is a function of the electron density n_e. If the plasma has a minor radius a, and k_o is the wavenumber without the plasma present, and k_p is the

wave number with the plasma present, then the shift in phase caused by the introduction of the plasma will be

$$\Delta\Psi = 2a(k_p - k_o) \tag{2.3a}$$

$$= (2a\omega/c)[(1-\omega_{pe}^2/\omega^2)^{1/2}-1] \tag{2.3b}$$

$$\simeq -a\omega_{pe}^2/\omega c \tag{2.3c}$$

$$= (-ae^2/\omega c\varepsilon_o m_e)n_e \tag{2.3d}$$

if $\omega_{pe}^2 << \omega^2$. Allowing n_e to have a spatial profile gives a phase shift

$$\Delta\Psi \simeq \frac{-1}{2\omega c}\int_{-a}^{a} \omega_{pe}^2(r)dr \tag{2.4a}$$

$$= \frac{-e^2}{2\omega c\varepsilon_o m_e}\int_{-a}^{a} n_e(r)dr \tag{2.4b}$$

Since the interferometer only measures $\Delta\Psi$ and not any profile information, one normally refers to the line averaged density given by

$$\bar{n}_e = |\omega c\varepsilon_o m_e \Delta\Psi/ae^2| \tag{2.5}$$

For typical BIGMAK operating conditions, a phase shift of up to 12π occurs, which is easily observed. The density will peak near $7 \times 10^{18} m^{-3}$, depending on the neutral gas filling pressure, and will fall within a few milliseconds to approximately $2 \times 10^{18} m^{-3}$, where it remains fairly constant throughout the remainder of the discharge. This drop in plasma density is not due to recombination of ions and electrons such that the plasma is only partially ionized. Significant radiation would be observed from the plasma were this the case. It is due, however, to recombination near the wall with the subsequent adhering of a large fraction of neutral particles to the

the wall.

The density can be raised again during the discharge by providing a source of neutral gas which ionizes upon entering the discharge. This is accomplished in BIGMAK by introducing hydrogen into an active discharge through a Veeco model PV-10 piezoelectric valve which can be opened or closed in approximately one millisecond. This process is commonly referred to as "gas puffing." Densities of up to $10^{19} m^{-3}$ have been achieved in BIGMAK using this system.

Relative impurity levels in BIGMAK are monitored by two diagnostics. The first monitors the oxygen impurity level by following the intensity of radiation from a spectral line of doubly ionized oxygen, which has an ionization potential of 35.15 eV. One reasonably intense line is at 464.914 nm, and it is monitored by a Jarrell-Ash .25 m monochrometer viewing the plasma through a glass port.

The second diagnostic for impurities is a simple ultraviolet (UV) light detector working on the principle of the photoelectric effect [22]. The detector consists of a small tungsten disk, 4 mm in diameter, which is 1 mm behind a copper grid. The disk is biased to -15 V with respect to the grid. The disk and grid are contained within an open ended iron cylinder to shield out magnetic fields, and the entire detector is mounted inside the vacuum chamber in a port .12 m from the edge of the plasma. The radiation

intensity is monitored by measuring the photoelectric current from electrons travelling from the plate to the grid. The detector is most sensitive to radiation in the range from 30 nm to 100 nm. The detector signal can be interpreted as a measure of the oxygen impurity level, although a strong signal is seen from hydrogen near the beginning of the discharge as it is being ionized. A hydrogen signal is also observed later in the discharge during the puffing of neutral gas.

A similar monitor often employed on BIGMAK is a visible light monitor, consisting of a simple photodiode circuit which responds to the intensity of light in the visible range of frequencies as viewed through a glass port. The interpretation of this signal is not simple, however, as which species of ion or neutral particle radiation the detector is responding to has not been determined.

D. Magnetic Probes and Data Acquisition System

The local magnetic field fluctuations which are the topic of this thesis are measured with probes inserted directly into the plasma. A diagram of a typical probe is shown in figure 8. The sensing coil consists of 4 to 10 turns of #30 or #38 gauge magnet wire wound on a grooved Lucite or Teflon base. The coil diameter is 3 to 6 mm with a width less than 2 mm. The coils can be oriented to receive any component of magnetic field desired, and more

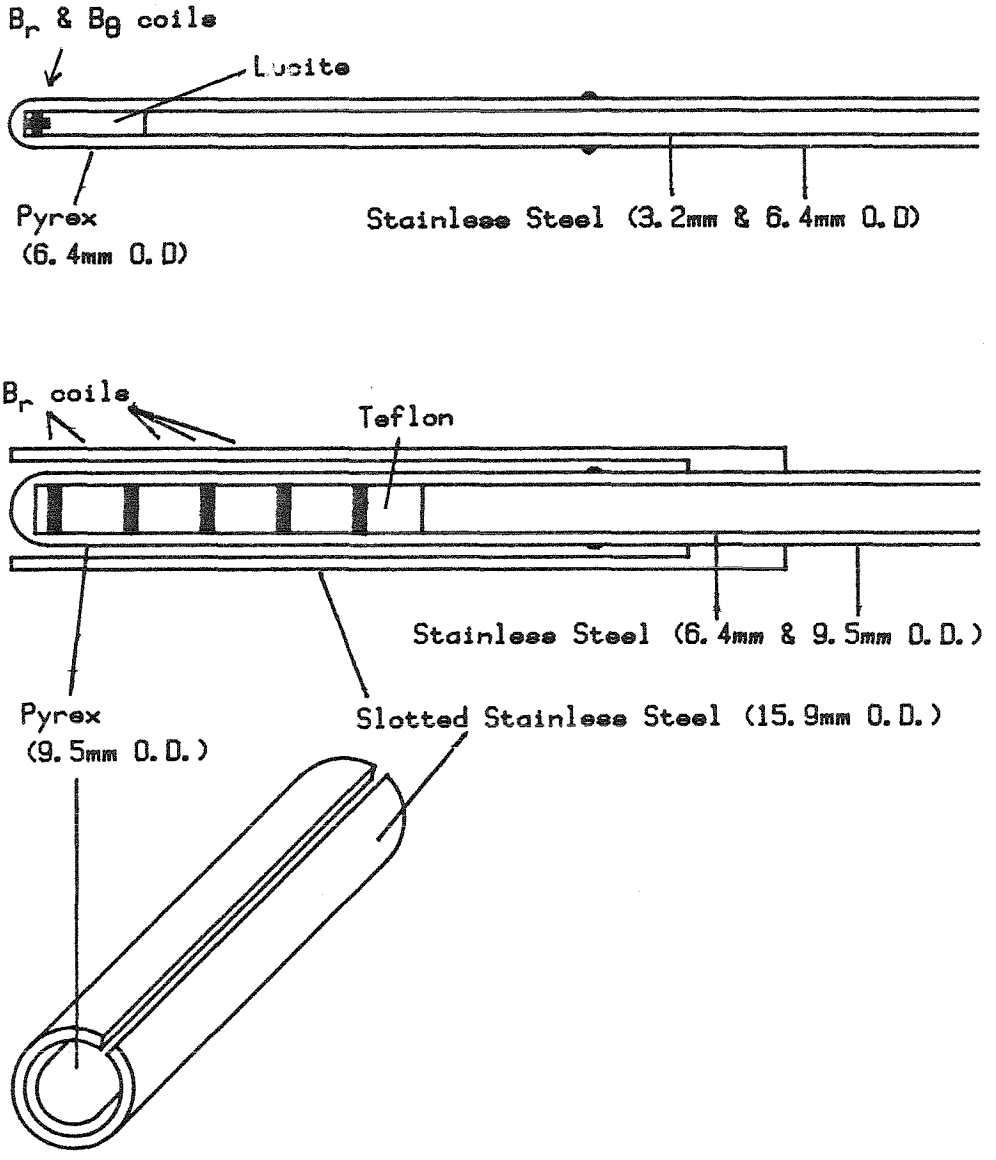

Figure 8. Typical magnetic probe constructions.

than one coil can be placed in a given probe. Twisted pair leads approximately .5 m long carry the signals to preamplifiers. The leads are shielded by 3 mm stainless steel tubing grounded through the receiving system. Care must be exercised to prevent grounding through the tokamak at the probe since the vacuum chamber is grounded through the turbomolecular pump. Ground loop signals can easily develop due to the flux from the ohmic heating coil. This precaution is necessary for all circuits near the chamber. Structural support for the probe is given by a surrounding 6 mm stainless steel tube. A transition is made to Pyrex in this tube .08 m from the end, and the end is sealed. The probe passes through an o-ring providing the vacuum seal. The probe is normally inserted along, or nearly along, a minor radius of the plasma. A pair of probes can be inserted from a side port. The tip of one can be arbitrarily adjusted with respect to the tip of the other by mounting one in a precision port aligner, which allows movement of the probe within a 10 degree cone. Probes which are used strictly for measuring the radial component of fluctuating field often have a protective stainless steel jacket outside the Pyrex with a longitudinal slot to prevent signal distortion. The jacket offers protection against runaway electrons, which can severely damage the Pyrex and produce vacuum leaks. The runaway electrons can heat the Pyrex, or cause pieces to flake off, providing an abundant source of oxygen impurities which quench the

discharge.

The probe signals are fed into preamplifiers near the tokamak. The preamplifiers have an input impedance of 50 ohms, which is designed to reduce capacitive pickup of electrostatic signals. The preamplifiers are two-stage amplifiers using LM301 operational amplifier chips. Each stage has 20 dB of gain. The compensation of the amplifiers is such that an overall gain of 40 dB flat to 1.5 MHz is achieved with circuit noise below the voltage step size of the analog to digital convertors used for data storage. The output stage of the preamplifiers includes an LH0002 line driver chip used to drive approximately 15 meters of RG58 coaxial cable between the preamplifiers and storage devices. The output impedance is approximately 1 ohm, so that the cable does not limit the bandwidth of the system.

A fast preamplifier has also been employed having a frequency response flat to 10 MHz, with a gain of up to 40 dB. The preamplifier employs an LM733 video amplifier with an LH0002 line driver in the feedback loop as in the case of the slower preamplifiers. The circuit noise is higher for this preamplifier, but it is useful in order to verify the observed high frequency portion of the spectra presented in chapter 5.

All time-varying electronic signals measured during the discharge are recorded digitally in 8 bit resolution format. Signals with slow variation, such as the Rogowski

signal, are recorded by a Biomation model 1015 waveform recorder or by several units employing analog to digital (A/D) conversion chips. The Biomation recorder has four channels of 1024 bytes (1 Kbyte) each with a maximum sampling rate of 100 kHz. Digital to analog (D/A) convertors allow continuous visual monitoring of stored waveforms on cathode ray tube displays. Twelve units with 1 Kbyte of storage each provide twelve channels with a maximum sampling rate of 200 kHz. Four additional units provide 1 Kbyte of storage each sampled at a maximum rate of 1 MHz. All sixteen units also include D/A convertors for continuous monitoring of stored waveforms.

The signals from the magnetic probes are recorded by four LeCroy model 2264 waveform recorders. Each unit has 32 Kbytes of storage and can sample at a rate of up to 4 MHz. The signals from the preamplifiers first pass through an impedance and voltage matching unit before entering the LeCroy modules. The matching unit allows input levels up to +12 V and provides flat output response to 2 MHz into the LeCroy modules' 50 ohm inputs.

Probe signals from the fast preamplifiers can also be fed directly into two LeCroy model 2256 waveform recorders. Each unit has 1 Kbyte of storage and can sample at a rate of up to 20 MHz. The frequency response of the acquisition system is shown in figure 9.

Permanent storage of signals is achieved through an interface to a Vector Graphics 1+ microcomputer. Data from

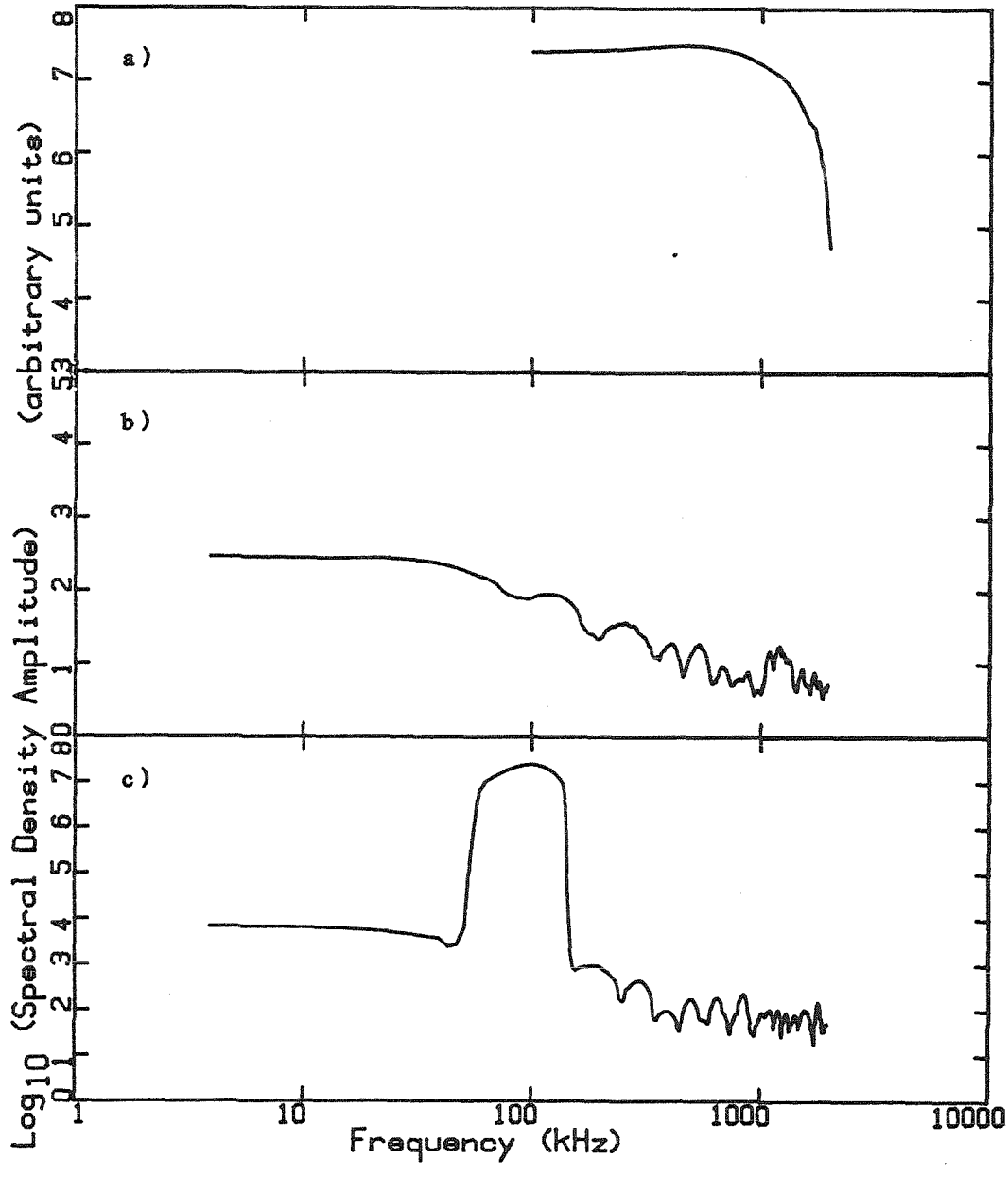

Figure 9. a) The spectral density amplitude versus frequency for the data acquisition system (excluding probes) for uniform amplitude input signals to the preamplifiers, b) the spectral density amplitude versus frequency with no input signal, and c) the spectral density amplitude versus frequency for a 100 kHz input signal to the preampliers, with Gaussian frequency averaging over 56 kHz full width at half maximum.

all units can be recorded between discharges on minifloppy diskettes. Data analysis is performed off line on an LSI-11/03 or an LSI-11/23 computer system. Details of the analysis procedure are given in chapter 3.

E. Discharge Cleaning Procedure

In order to obtain tokamak discharges with reasonably low impurity levels, the vacuum chamber walls must first be conditioned by a discharge cleaning procedure. The toroidal field coil is connected to a direct current supply which produces a 140 gauss field in the center of the chamber. The ohmic heating winding is connected to a 3-5 kW oscillator whose frequency is approximately 35 kHz. The oscillator operates with a duty cycle of approximately 10 percent, having two 50 msec pulses per second. The chamber is filled with hydrogen at approximately 3×10^{-4} torr. Although the discharge cleaning procedure is not totally understood, it is believed that the cool, poorly confined hydrogen plasma interacts with impurities such as carbon and oxygen at or near the surface of the walls forming gaseous products which are easily pumped out of the system. Carbon and oxygen can severely alter the characteristics of the hot tokamak plasma discharge due to severe line radiation from partially ionized atoms. Monitoring of the quadrupole gas analyzer shows that carbon is removed from the walls as methane much more quickly than oxygen is removed as water

vapor, so that the removal of oxygen sets the time frame for adequate cleanliness. Typically five hours of discharge cleaning is required to remove the daily influx of oxygen from vacuum chamber leaks, while twenty-four hours is required if the chamber has been opened to the atmosphere.

The effect of discharge cleaning on the tokamak discharges is as radical as the effect of the horizontal field nentioned previously. With clean walls, a discharge lasting 22 msec with a peak current of 30 kA is easily possible. With walls which have not been cleaned, discharges will rarely exceed 5 msec in length or 10 kA in current. Large signals can be observed from the monochrometer (monitoring the 464.9 nm oxygen line), the UV detector, and the visible light monitor. Also, an external safety monitor for x-ray radiation shows a larger signal for dirty discharges than for clean discharges.

F. Typical Discharge Characteristics

Figure 10 shows the plasma current, loop voltage, line average electron density, 464.9 nm oxygen line intensity, and UV detector signal for a typical tokamak discharge without the puffing of neutral gas. The filling pressure for this discharge is 1.4×10^{-4} torr. The plasma current peaks at approximately 8 msec into the discharge. At this point, if one assumes that the inductive energy of the plasma is not changing, one can

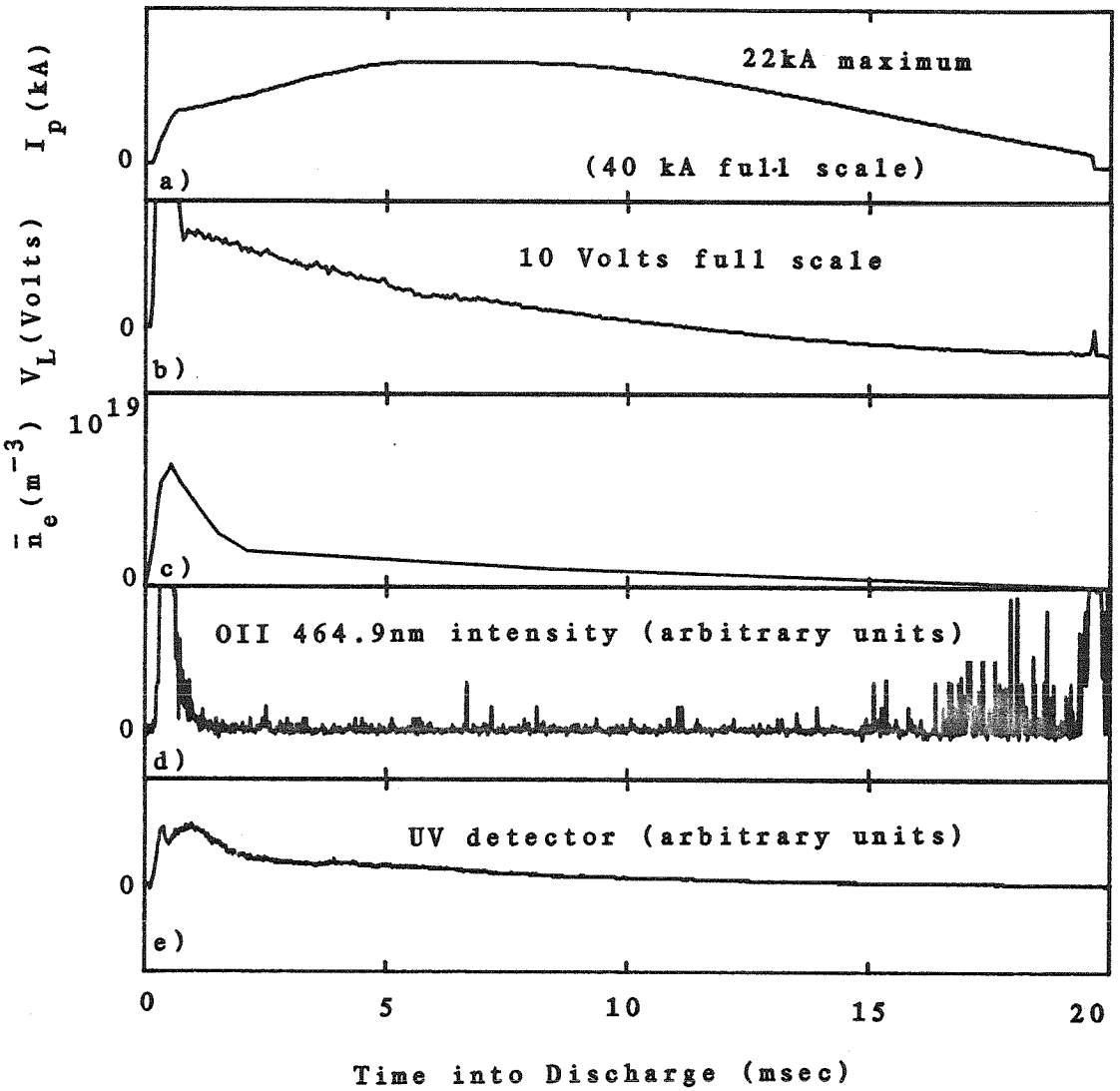

Figure 10. a) The plasma current, b) loop voltage, c) line average density, d) 464.9 nm oxygen line intensity, and e) UV detector signal for a typical discharge without gas puffing.

measure the resistance of the plasma. In particular, the resistance has a strong dependence on electron temperature, where the resistivity of the plasma is given by [3]

$$\eta = (1.65 \times 10^{-9}) Z_{eff} T_e^{-3/2} \ln\Lambda \quad \text{ohm-m} \qquad (2.6)$$

where T_e is measured in keV, and

$$Z_{eff} = (\sum_k n_{ik} Z_k)/n_i \qquad (2.7)$$

is the effective ionic charge of the plasma. Figure 11 shows temperature versus conductance of the plasma where the various curves are for different values of Z_{eff}. The figure assumes parabolic profiles of n_e and T_e in minor radius. These profiles cannot be measured on BIGMAK with available diagnostics, but similar profiles have been measured on other tokamaks. The peak temperature for the discharge shown in figure 10 is 105 eV if $Z_{eff} = 1$.

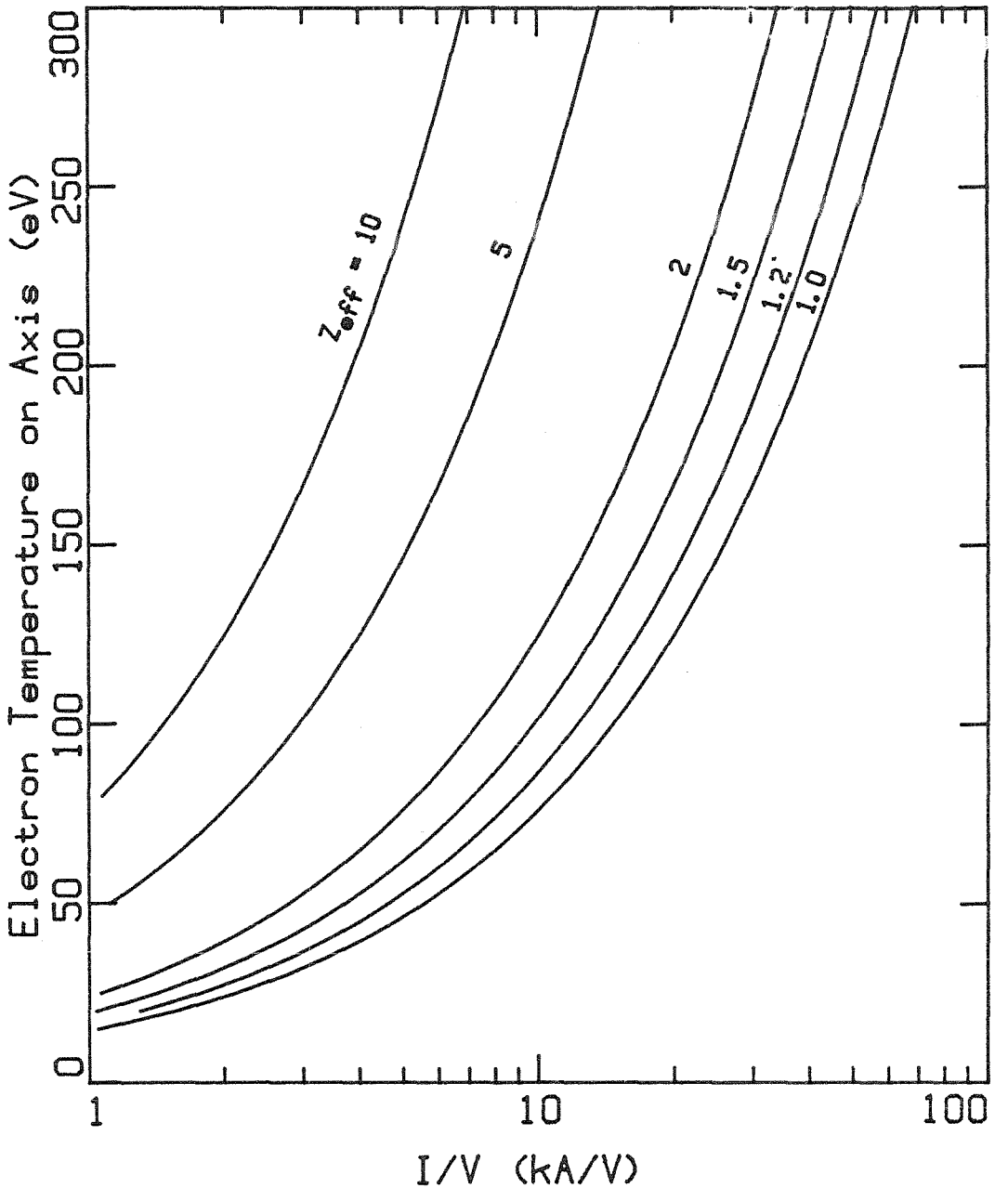

Figure 11. The central electron temperature versus plasma conductivity for various Z_{eff} assuming parabolic radial profiles of density and electron temperature.

III. COMPUTATIONAL TECHNIQUES

A. Introduction

All data obtained from BIGMAK are stored in digital 8-bit resolution format. These numbers represent the voltage of a signal sampled at regular intervals during the discharge. In particular, the fluctuating signals from the magnetic probes are stored in this format. A typical raw signal from a probe is shown in figure 12. The fluctuation level appears to be higher during the initial breakdown phase of the discharge than later. In order to elicit more information from the probe signals, certain analysis techniques are applied to the data. Due to the sampled nature of the data and its finite length, these techniques produce only estimates of functions which are properly defined only for continuous, infinite functions. Where it is appropriate, the subscript "E" is used to indicate that a function is only an estimate of the true function in question.

B. Root Mean Square Fluctuating Field Strength

The first of these techniques involves a calculation of the root mean square fluctuating field level, δB_{rms}. The raw signal is the amplified voltage across the sensing coil in the plasma, given by

$$V = -\frac{d\Phi}{dt} \qquad (3.1a)$$

$$= -A\frac{dB}{dt} \qquad (3.1b)$$

where Φ is the magnetic flux through the coil and A is the

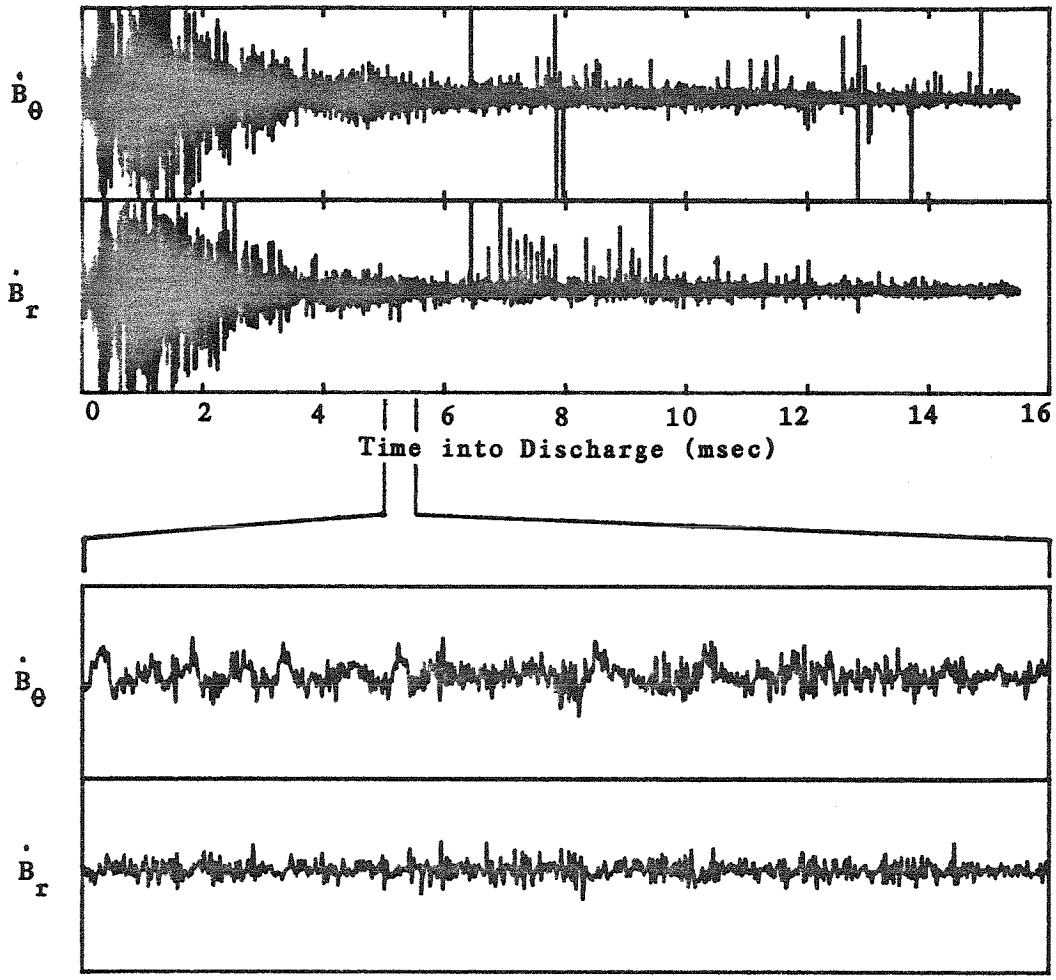

Figure 12. Typical raw probe signals for both poloidal and radial components. The lower traces are 512 μsec in duration with 1024 sampled points each.

coil area. Implicit in equation 3.1b is the assumption that B does not vary across the coil, which is true if the characteristic wavelengths associated with the fluctuations are larger than the coil diameter. The raw signal then is not a measure of the magnetic field, but rather the time derivative of the magnetic field at a given spatial point. In order to calculate δB_{rms}, the signal must be integrated. The integration is carried out in the following manner. A piece of the time record is taken, and the non-fluctuating part of the magnetic field is assumed to be stationary, that is, there are no trends in the data such that the magnetic field is found to be greater at the end of the integration than at the beginning. This is equivalent to subtracting the average value of the signal from the signal before integrating. If $\dot{B}_k$ is the signal known at N consecutive points, and $\dot{B}_{av}$ is the average value of the signal for these points, and Δt is the time interval between points, then the fluctuating field, δB_k, is given by

$$\delta B_k = \delta B_{k-1} + (\dot{B}_k - \dot{B}_{av})\Delta t \qquad (3.2)$$

with δB_0 chosen so that the average fluctuating field is zero. The root mean square fluctuating field level is then given by

$$\delta B_{rms} = \left[\frac{1}{N}\sum_{k=1}^{N}(\delta B_k^2)\right]^{1/2} \qquad (3.3)$$

There are several precautions to be taken when applying this integration technique. The data are assumed here to be

stationary, which is not always true in the discharge, particularly near the beginning when parameters are changing rapidly. The data may also fail to be stationary if minor disruptions occur during the record which is analyzed. Care must also be taken to avoid data records which have switching transients from the field power supplies superimposed on the data. It should be noted here that sufficient scatter in the data is observed to require ensemble averaging in order to estimate δB_{rms}. With these precautions in mind, a refinement of the crude integration technique employed is not justified.

C. Probability Density Estimates

Another technique which can be applied to the data is to compute the probability density function for the data given by [28]

$$p(x) = \lim_{\Delta \to 0} \frac{\text{Prob}[x < x(t) < x+\Delta x]}{\Delta x} \qquad (3.4)$$

which is a measure of how likely it is to find the signal within a given range of values. Although this function is not a definitive test of the noiselike character of the signal, it approaches the classic Gaussian shape centered on the mean value as the signal becomes more like random noise in character, and so it can be useful in indicating whether or not a signal is likely to be composed of random noise or not. With the raw signals consisting of a string of integers ranging in value from 0 to 255, this function is easily approximated as the number of points in a given

data record with each possible value.

D. Correlation Function Estimates

It is often useful to know how well correlated two signals are. In particular, signals from two coils at two different locations are often recorded during the same discharge. The normalized correlation function of two signals with zero mean is given by [29]

$$C(\tau) = \frac{\lim_{T\to\infty} \frac{1}{T}\int_{-T/2}^{T/2} f(t)g(t+\tau)dt}{\left[\lim_{T\to\infty} \frac{1}{T}\int_{-T/2}^{T/2} f^2(t)dt \lim_{T\to\infty} \frac{1}{T}\int_{-T/2}^{T/2} g^2(t)dt\right]^{1/2}} \quad (3.5)$$

where f(t) and g(t) are the two signals. The correlation function which is computed from data records is only an approximation to the true correlation function, $C(\tau)$, in that the data are only known for a finite interval and are sampled data rather than continuous data. Hence, an estimate of the correlation function is

$$C_E(\tau) = C_E(n\Delta t) = \frac{\frac{1}{N-n}\sum_{k=1}^{N-n} f(t_k)g(t_{k+n})}{\left[\frac{1}{N}\sum_{k=1}^{N} f^2(t_k) \frac{1}{N}\sum_{k=1}^{N} g^2(t_k)\right]^{1/2}} \quad n>0 \quad (3.6a)$$

$$C_E(\tau) = C_E(n\Delta t) = \frac{\frac{1}{N-n}\sum_{k=1-n}^{N} f(t_k)g(t_{k+n})}{\left[\frac{1}{N}\sum_{k=1}^{N} f^2(t_k)\ \frac{1}{N}\sum_{k=1}^{N} g^2(t_k)\right]^{1/2}} \qquad n<0 \qquad (3.6b)$$

If $C_E(\tau) = 1$ for a given value of τ, the signals are perfectly correlated (identical). If f(t) and g(t) are the same signal, that is, from the same coil, $C_E(0) = 1$, and one can measure a time τ_c such that $C_E(\tau)<\xi$ for $|\tau|>\tau_c$. Here τ_c is called the autocorrelation time, and $C_E(\tau)$ becomes $C_{Ea}(\tau)$, which is an estimate of the autocorrelation or autocovariance function. The choice of ξ is somewhat arbitrary and depends on the number of points N. If the signal is decorrelated in time τ, then statistically one could expect $C_E(\tau)$ to have a root mean square value near $(N)^{-1/2}$. If one chooses ξ to be a few times $(N)^{-1/2}$, then one can expect $C_E(\tau)<\xi$ for most of the points $|\tau|>\tau_c$.

E. Power Spectral Density Estimates

Perhaps the most powerful analysis tool used on the data is the technique of computing power spectra. Given a continuous function f(t) and its Fourier transform

$$F_T(\omega) = \int_{-T/2}^{T/2} f(t)e^{-i\omega t}dt \qquad (3.7)$$

then the power spectral density of f(t) is defined as [29]

$$P(\omega) = \lim_{T\to\infty} \frac{1}{T} F_T^*(\omega) F_T(\omega) = \lim_{T\to\infty} \frac{1}{T} |F_T^2(\omega)| \qquad (3.8)$$

It is also true that

$$P(\omega) = \int_{-\infty}^{\infty} C(\tau) e^{-i\omega\tau} d\tau \qquad (3.9)$$

$P(\omega)$ is a real, even function of ω. Its usefulness becomes clear when it is considered in the case where f(t) is a sampled function of finite length rather than a continuous, infinite function. The $P_E(\omega)$ thus calculated is an estimate of the true power spectrum. However, it is rather straightforward to refine the estimate to any degree of accuracy required if sufficient data are available. This is not in general true for other estimates made from sampled data of finite length [29].

Since the data are sampled at discrete time intervals Δt for a period of time T, the Fourier transform can now only be estimated at discrete frequencies with a frequency interval $\Delta\omega = 2\pi/T$. The sampled nature of the data sets a maximum limit to the frequency in the transform, $\omega_{max} = \pi/\Delta t$. This maximum frequency arises from the fact that waveforms with frequencies higher than ω_{max} are indistinguishable from waveforms with frequencies lower than ω_{max}. This is the phenomenon of aliasing. The maximum frequency allowed is not so much a restriction on the analysis as it is a restriction on the data acquisition system that the sampling interval be sufficiently short that ω_{max} is well above any

frequencies present in the signals.

The finite length of the data modifies the transform in another way. The transform is not of an infinite function f(t), but rather of f'(t) = f(t)u(t), where u(t) is a "window function" given by

$$\begin{aligned} u(t) &= 0 \quad |t|>T/2 \\ &= 1 \quad |t|<T/2 \end{aligned} \tag{3.10}$$

if the data are centered on t=0. The transform is modified, then, by convolving $F_E(\omega)$ with $U_E(\omega)$, the transform of u(t), that is [30]

$$F'_E(\omega) = \int_{-\infty}^{\infty} F_E(\omega')U_E(\omega-\omega')d\omega' \tag{3.11}$$

where

$$U(\omega) = (2/\omega)\sin(\omega T/2) \tag{3.12}$$

This convolution can be thought of as mixing frequencies in the transform, that is, $F'_E(\omega)$ at a given ω contains many weighted contributions from a broad range of frequencies in $F_E(\omega)$.

This broad range of frequencies can be narrowed considerably by using a window function other than u(t). One particularly good choice is the Hanning function, given by

$$\begin{aligned} h(t) &= 0 \quad |t|>T/2 \\ &= [1 + \cos(2\pi t/T)]/2 \quad |t|<T/2 \end{aligned} \tag{3.13}$$

with a Fourier transform

$$H(\omega) = (1/\omega)\sin(\omega T/2) + \frac{T}{4}\left[\frac{\sin[\pi-(\omega T/2)]}{\pi-(\omega T/2)} + \frac{\sin[\pi+(\omega T/2)]}{\pi-(\omega T/2)}\right] \tag{3.14}$$

Although it is not immediately obvious that H(ω) is a

good choice, it provides a very low amount of frequency mixing when the transform is discrete. Only the nearest neighbor frequencies are mixed in with a given frequency component. If the transform gives values at discrete frequencies ω_i, then the transform of f(t)h(t) in terms of $F_E(\omega_i)$ is

$$F'_E(\omega_i) = .25F_E(\omega_{i-1})+.5F_E(\omega_i)+.25F_E(\omega_{i+1}) \qquad (3.15)$$

This gives an effective resolution which is twice that of the separation of frequencies in the transform.

It was previously stated that the power spectral density computed from a finite length of discretely sampled data is only an estimate of the true power spectrum of the signal, because the data are subject to systematic and random errors in sampling. Since the fluctuations observed rarely exhibit strong peaks, the most important errors are random errors. The normalized root mean square error for any point in the computed power spectrum is given by [28]

$$W = (R_e T)^{-1/2} \qquad (3.16)$$

where R_e is the effective frequency resolution of the spectrum in cycles per second and T is the length of the data used to compute the spectrum. Obviously the error can be reduced by averaging over adjacent frequencies or by ensemble averaging of many spectra from data obtained under similar conditions. This is necessary since W=1 for a spectrum from a single data record without frequency averaging ($R_e = 1/T$). It should be noted that W given above reflects the range within which approximately 70

percent of the points will be found. An estimate of the range within which 90 percent of the points will be found is given by

$$W = 1.6\ (R_e T)^{-1/2} \tag{3.17}$$

The power spectral density estimates discussed so far have been from a single time signal. It is also useful to estimate the power spectral density from two time signals. This spectral density is called the cross power spectral density defined by

$$P_C(\omega) = \lim_{T\to\infty} \frac{1}{T} F_T^*(\omega) G_T(\omega) \tag{3.18}$$

where $F_T(\omega)$ and $G_T(\omega)$ are the Fourier transforms of f(t) and g(t) respectively. The function $P_C(\omega)$ is a complex function having a magnitude and a phase. As in the case of the spectral density of a single function of time, the fact that the data are sampled and of finite length leads to computations of $P_{CE}(\omega)$, which is an estimate of the true cross power spectral density. If f(t) and g(t) represent signals from two coils at different locations in the discharge, then an estimate of the phase relationship between the two coils can be made, giving a component of the phase velocity. The confidence in this estimate can be obtained from an estimate of the coherence function

$$\gamma_E(\omega) = \frac{|\langle F_E^*(\omega) G_E(\omega)\rangle|}{\left[\langle |F_E^2(\omega)|\rangle \langle |G_E^2(\omega)|\rangle\right]^{1/2}} \tag{3.19}$$

where the brackets ($\langle\rangle$) indicate either frequency or ensemble averaging, and $\gamma_E(\omega)$ lies between 0 and 1.

The physical significance of the coherence function can best be illustrated by considering the case of ensemble averaging over many measurements of f(t) and g(t). The quantities in the denominator are not affected by changes in the phase from measurement to measurement. However, the numerator is averaging complex numbers, and so is very dependent on phase. If a coherent signal is reproducibly propagating from one coil to another at frequency ω, the phase will not change appreciably during the averaging, and $\gamma_E(\omega)$ will be nearly equal to one. Whereas, if the signal is incoherent, the value of $\gamma_E(\omega)$ will be lower, reflecting the statistics of averaging random phases. Thus $\gamma_E(\omega)$ is often called the frequency resolved correlation function, since coherence may only be present for a small range of frequencies. A coherent mode may be found from $\gamma_E(\omega)$ even though $C_E(\tau)$ shows two signals to be uncorrelated.

IV. MAGNETIC FLUCTUATIONS - BACKGROUND

A. Introduction

This chapter is concerned with giving a background on 1) the theoretical backing for making fluctuation measurements and 2) the related experiments previously reported. The theoretical discussion is divided into two sections. The first deals with the theory of possible sources for fluctuations, while the second looks at the effects of fluctuations on transport. The discussion is not limited to magnetic field fluctuations, but also includes electrostatic fluctuations since they may play a role in transport in tokamaks. Historically, the electrostatic fluctuations were considered first. Attention shifted to magnetic fluctuations when Callen [14] showed that the magnetic fluctuations can cause more transport than the electrostatic fluctuation part of drift waves under the appropriate conditions. It is as yet unclear which phenomenon dominates in tokamaks. The section on experimental background is limited to magnetic fluctuation measurements in tokamaks. It should be mentioned here that Langmuir probes have been routinely used to measure local potentials, densities, and temperatures in cool plasma devices for many years. Also, laser scattering measurements and microwave scattering measurements of density fluctuations have been made in recent years on several tokamaks [31-37].

B. Theory of Fluctuation Sources

One of the most fruitful models for describing a tokamak plasma is that provided by the magnetohydrodynamic (MHD) model. In this model, the plasma is treated as a single electrically active fluid governed by the fluid equations, Maxwell's equations, and Ohm's law. In the limit of a perfectly conducting fluid, these become [2]:

the continuity equation

$$\partial\rho/\partial t = -\underset{\sim}{\nabla}\cdot(\rho\underset{\sim}{v}) \tag{4.1}$$

the momentum equation

$$\rho(\partial\underset{\sim}{v}/\partial t) = -\underset{\sim}{\nabla}p + \underset{\sim}{J} \times \underset{\sim}{B} \tag{4.2}$$

Faraday's law

$$\partial\underset{\sim}{B}/\partial t = -\underset{\sim}{\nabla} \times \underset{\sim}{E} \tag{4.3}$$

Ampere's law

$$\mu_o\underset{\sim}{J} = \underset{\sim}{\nabla} \times \underset{\sim}{B} \tag{4.4}$$

and Ohm's law

$$\underset{\sim}{E} = -\underset{\sim}{v} \times \underset{\sim}{B} \tag{4.5}$$

This set of equations can be closed by an equation of state

$$p\rho^{-5/3} = \text{constant} \tag{4.6}$$

Here $\underset{\sim}{v}$ is the macroscopic fluid velocity, $\underset{\sim}{B}$ is the magnetic field, p is the thermal pressure, ρ is the mass density, $\underset{\sim}{E}$ is the electric field measured in the laboratory frame of reference, and $\underset{\sim}{J}$ is the current density. The MHD equations assume that the plasma is quasineutral, that is, the charge density $\sigma = 0$ for scale lengths longer than the Debye length [4]

$$\lambda_D = (\varepsilon_o kT_e/ne^2)^{1/2} \qquad (4.7)$$

which is typically very small compared to the dimensions of the plasma. The equations also neglect the displacement current, $\partial D/\partial t$, which is valid if the Alfvén speed given by

$$v_A = B/(\mu_o \rho)^{1/2} \qquad (4.8)$$

is much less than the speed of light.

This MHD model has been used successfully to predict the equilibria of plasmas in many configurations, in particular the tokamak configuration. The model predicts a magnetic topology consisting of simply nested, ergodically covered toroidal magnetic surfaces with occasional rational surfaces where field lines close on themselves without covering the surface. The model provides a more precise definition of the safety factor $q(r)$ as

$$q(r) = d\Psi_{tor}/d\Psi_{pol} \qquad (4.9)$$

where Ψ_{tor} the magnetic flux through a cross section of the torus and Ψ_{pol} is the flux through any surface spanning the hole in the center of the torus. The formula

$$q(r) = (rB_T)/(RB_\theta) \qquad (4.10)$$

is an approximation to equation 4.9. MHD theory can be used to show how the plasma cross section can be shaped by external currents. The model also shows the need for the vertical field given in chapter 1 and can be used to compute the strength of field needed for equilibrium. The concept of magnetic field lines being frozen into a

perfectly conducting plasma follows from MHD theory.

The MHD model can also be used to predict the susceptibility of the plasma to various instabilities. Kink modes have been investigated for plasmas with a boundary at r=a and a vacuum region for r>a [38-43]. The modes can be characterized by a poloidal mode number m where the perturbations vary as $e^{im\theta}$. The m=0 mode is the sausage instability mentioned in chapter 1. A physical picture of the m=1 mode has been given by Johnson, Oberman, Kulsrud, and Frieman [38]. Consider the helical perturbation shown in figure 13, where the two ends of the cylindrical section shown are one quarter wavelength apart, and consider the perturbation of the magnetic field accompanying the plasma position perturbation. The angle ϕ is the angle subtended by the equilibrium field line around the axis in moving from one cross section to another. The angle $\phi+\phi^1$ is the angle subtended by the perturbed field line. The case shown is for $\phi>90^o$. If $\phi>90^o$, then $\phi+\phi^1>\phi$ and the perturbed field will have a stronger poloidal component than the equilibrium field. This larger poloidal field increases the $\underset{\sim}{J}$ x $\underset{\sim}{B}$ force on the plasma enhancing the perturbation. Similarly, if $\phi<90^o$, then $\phi+\phi^1<\phi$ and the perturbation field has a weaker poloidal component than the equilibrium field. This results in a weaker $\underset{\sim}{J}$ x $\underset{\sim}{B}$ force and the perturbation is stabilized. The angle ϕ is simply related to the safety factor q. The m=1

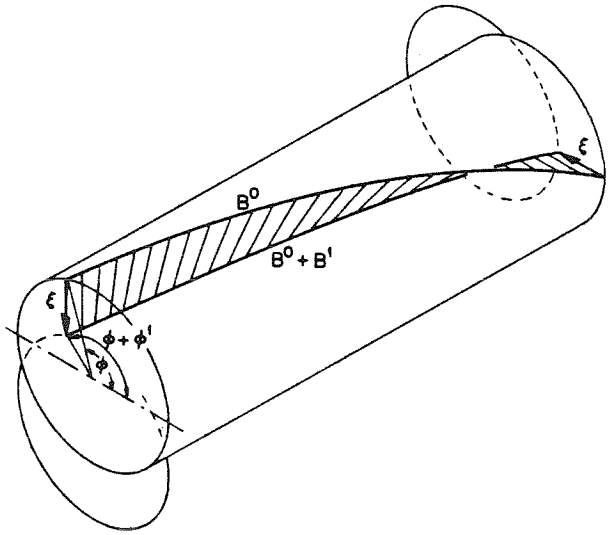

Figure 13. The kink instability in a fat plasma (from Johnson, et.al. [38]).

mode is stable for $q>1$ and unstable for $q<1$. This condition for stability on q at the edge is known as the Kruskal-Shafranov stability criterion, which sets a limit to the toroidal current for a given toroidal magnetic field. Higher order kink modes are also possible with mode numbers m and n, where $e^{inz/R}$ is the variation in the toroidal direction. These modes are unstable for $q<m/n$. This stability criterion is derived for a sharp discontinuity in the current profile at the plasma edge. Typical tokamak current profiles taper off smoothly near the edge, and this has a stabilizing influence on kink modes.

A different class of instabilities is possible if one considers not a perfectly conducting plasma, but one with finite resistivity. Although resistivity might be thought of as simply a dissipative term which would serve only to reduce the growth rates of instabilities in a perfectly conducting plasma, resistivity in fact relaxes some of the restrictions imposed by the ideal MHD theory [2]. In particular, the field lines can now break and reconnect into a new magnetic topology which has a lower potential energy. This leads to the formation of magnetic islands as shown in figure 14. A magnetic island is a topologically independent subset of the plasma with nested flux surfaces around a magnetic axis. Figure 15 shows a schematic view of how islands are formed. In figure 15b and 15c the torus is opened up into a slab geometry, with

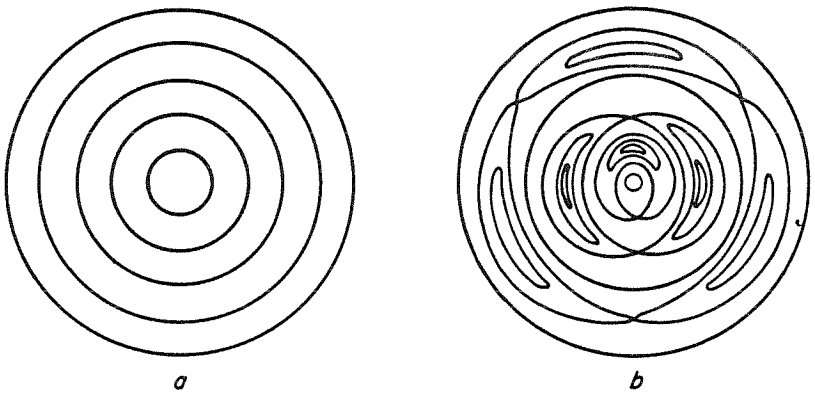

Figure 14. a) Simply nested flux surfaces, and b) flux surfaces with m = 1, 2, and 3 island structures (from Bateman [2], p. 192).

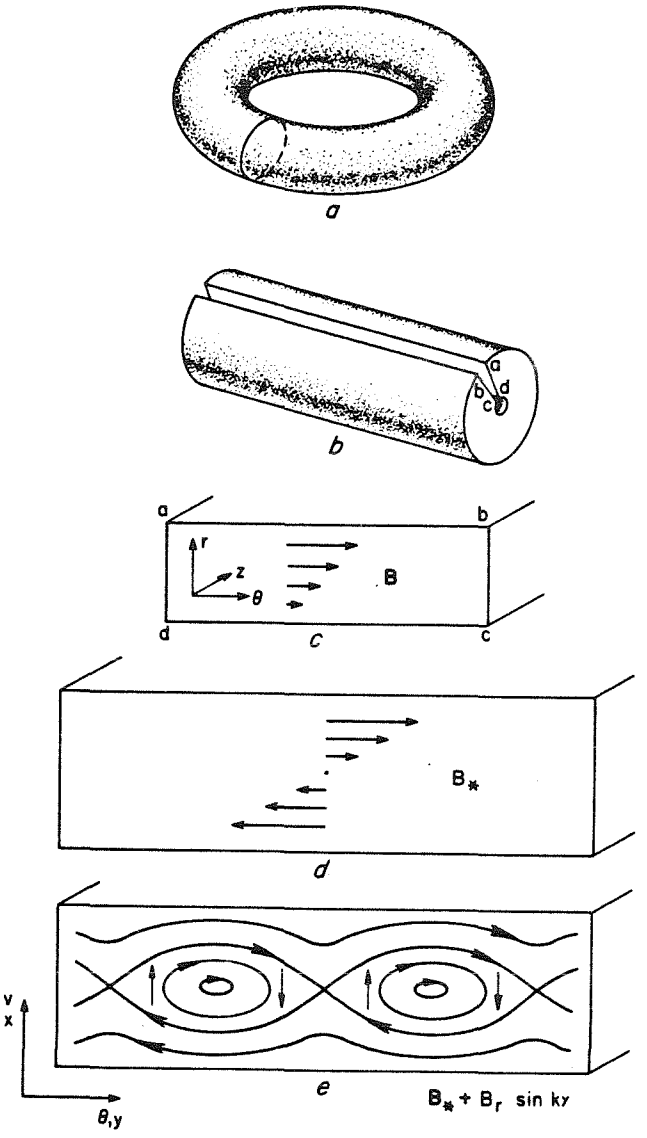

Figure 15. A schematic of magnetic islands. a) A toroidal plasma, b) cut open, and c) laid out flat, d) with the zero shear field subtracted, and e) a radial perturbation added showing the formation of the islands (from Bateman [2], p. 194).

the total poloidal field shown in figure 15c. The zero shear component of poloidal field has been subtracted in figure 15d. If a small radial magnetic field perturbation with sin(ky) dependence is added to this sheared field, the configuration of figure 15e is obtained. Taking the boundary conditions of the toroidal plasma into account, these radial field perturbations will grow at mode rational surfaces, that is, surfaces where q=m/n, m and n being integers. The perturbations cannot occur without finite resistivity, since a finite electric field parallel to the field lines is required from Maxwell's equations. Such an electric field is not allowed in the ideal MHD model, but simply produces parallel current flow with finite resistivity. The formation of islands reduces the magnetic energy, with the difference in energy being transferred to the plasma by these currents.

The instability which is responsible for the island formation is called the resistive tearing mode, which has been studied extensively theoretically [23,44-54]. From nonlinear growth rate calculations it has been shown that a magnetic island should saturate in size when the radial width is a few tenths of the plasma radius.

High-m drift-tearing modes, or microtearing modes, have also been recently studied [19,20,22,25]. These modes have a radial component of magnetic field which leads to the formation of small, densely packed magnetic islands similar to those formed by the resistive tearing mode. The

qualitative difference lies in the source of energy for the modes. The resistive tearing mode is unstable because it results in a decrease in the total magnetic energy. Microtearing modes exist only in a region with an electron temperature gradient, drawing their energy from the expansion of thermal energy in the presence of the mode. Microtearing modes are believed to be unstable for frequencies less than ν_{ei}, the electron-ion collision frequency, with a maximum growth rate at a frequency near $.1\nu_{ei}$.

An alternative mechanism to microtearing modes which would lead to the formation of small magnetic islands is the "magnetic flutter" associated with high mode number drift waves. This mechanism was pointed out by Callen [14].

The theory of magnetic fluctuation sources is still being actively pursued. One intriguing new theory by C. Chu [21] seeks to describe the magnetic turbulence in a current carrying plasma with a statistical black-body model in which the external circuits act as a heat bath for the magnetic fields in the plasma. The model predicts a spectrum of radial fluctuations

$$B_r(\omega) \propto \left[\frac{(\omega/\omega_T)}{\exp[(\omega/\omega_T)^{1/2}]-1}\right]^{1/2} \qquad (4.11)$$

where ω_T depends on the energy confinement time τ_E and the "magnetic temperature" of the heat bath.

C. Theory of Fluctuation Effects - Transport

It is interesting to estimate to what extent the various sources of magnetic fluctuations contribute to transport. Magnetic islands can enhance global transport in that transport across an island is nearly infinite. In neoclassical theory, particles stay within a small distance of a flux surface until suffering a collision. However, both the inner and outer boundaries of an island are the same flux surface, so that collisions are not needed for a particle to traverse the island. In chapter 1, the neoclassical confinement time was estimated as $a^2/4D$, where a is the plasma minor radius and D is the diffusion coefficient. A crude estimate of the effect of islands on transport can be obtained by replacing a with $a' = a-s$, where s is the sum of the widths of the islands present. Although a single island structure may saturate with a width of order .3a, it is not likely that non-overlapping islands can account for a sufficient fraction of the minor radius in order to put the neoclassical estimate in line with experimentally observed confinement times. Also, the dependence of τ_E on n_e is not changed from neoclassical theory, which is in disagreement with observations.

If the magnetic islands overlap, the picture of diffusion is considerably altered. The simply nested flux surfaces of ideal MHD theory which become more complicated structures with simple islands have now been totally

destroyed. The points of intersection of a field line with a cross sectional plane of the torus no longer trace out a smooth curve, but rather fill the volume with a sequence of irregular points. This is known as a stochastic field region. The electron thermal diffusion coefficient has been estimated by Rechester and Rosenbluth [10]. In the collisionless case, where the mean free path of the electrons λ is much greater than the correlation length of the field lines L_c, the diffusion coefficient is given by

$$D \sim (\delta v_r)^2 \tau_c \tilde{=} v_{the}^2 \tau_c (\delta B_r / B_T)^2 \tilde{=} v_{the} \pi R (\delta B_r^2 / B_T). \qquad (4.12)$$

Here, δv_r is the average fluctuating velocity, τ_c is the correlation time associated with an electron moving a correlation length along the field line at the thermal velocity v_{the}, and πR is taken as a crude estimate of the correlation length, L_c. If the plasma is collisional, i.e., $\lambda << L_c$, then D is reduced by a factor of λ / L_c from the collisionless case. The diffusion coefficient of equation 4.12 provides a better estimate of the energy confinement time than that given by equation 1.17. In BIGMAK, with a typical T_e of 100 eV, using πR as an estimate of L_c, fluctuations of order

$$\delta B_r / B_T \sim 2 \times 10^{-3} \qquad (4.13)$$

are required to explain the observed confinement time.

The dependence of this stochastic field diffusion coefficient on plasma parameters is of interest. There is no explicit dependence on the density, and the diffusion is

apparently greater for higher electron temperatures. The coefficient is very strongly dependent on $\delta B_r/B_T$. However, the origin of the fluctuations is not yet described by a suitable theory, so that the dependence of $\delta B_r/B_T$ on n_e and T_e is not clear. If the stochastic field diffusion explains anomalous transport as observed in tokamaks, then $L_c(\delta B_r/B_T)^2$ should be proportional to n_e^{-1}.

The microtearing mode theory [19,20,22,25] also explains transport in terms of magnetic island overlap. This theory, however, also provides for a source of magnetic fluctuations and estimates their saturation amplitude. The growth and damping rates balance for

$$\delta B_r/B_T \sim \rho_e/L_T \qquad (4.14)$$

where ρ_e is the electron Larmor radius and L_T is the scale length of the temperature gradient. The theory then predicts a diffusion coefficient [19]

$$D \sim (v_{the}^2/\nu_{ei})(\delta B_r/B_T)^2 \qquad (4.15)$$

where ν_{ei} is the electron-ion collision frequency. Note that this is the same as the diffusion coefficient used in the simple model from which equation 1.17 was derived. This theory is valid only in the collisional regime. As the plasma becomes collisionless, this diffusion process is limited by the correlation length of the field fluctuations. That is, the factor v_{the}/ν_{ei}, which is the mean free path of the electron, can be no larger than L_c. It is easy to see

that the diffusion predicted by equation 4.15 can be no greater than that predicted by equation 4.12. This same argument applies to the diffusion coefficient which went into the estimate of equation 1.17, so that equation 1.18 is overly optimistic in estimating diffusion from a given fluctuating field level. Equation 4.13 does provide a better estimate for the level of fluctuations required to produce the energy confinement time observed in BIGMAK. Note that this estimate could be lowered if $L_c > \pi R$, but must be raised if $L_c < \pi R$.

As with microtearing modes, the drift wave produced magnetic flutter [14] also depends on island overlap to explain transport, so that equation 4.12 again provides an upper bound for the estimate of diffusion.

The black-body model of Chu [21] also provides an estimate for the radial diffusion coefficient as

$$D \sim (B_T/3\mu_o n_e e)(\delta B_r/B_T) \qquad (4.16)$$

requiring $\delta B_r/B_T$ to be only 6×10^{-5} to explain the observed confinement time. The model also provides for the correct dependence of τ_E on n_e. The model, however, assumes isotropic fluctuations and transport. Further refinements of the model which account for the anisotropic tokamak geometry will probably revise the estimate for the level of $\delta B_r/B_T$ necessary to explain the observed transport.

An alternate source of transport may be found from fluctuating electric fields rather than magnetic fields.

The stochastic magnetic field transport theory depends heavily on the fluctuating radial velocity, $\delta v_r = v_{the}(\delta B_r/B_T)$. Such a fluctuating velocity could also be produced from a poloidal electric field fluctuation, giving

$$\delta v_r = \delta E_\theta / B_T \qquad (4.17)$$

This velocity follows simply from the fact that a charged particle in perpendicular electric and magnetic fields experiences alternate accelerations and decelerations in its Larmor orbit leading to a drift in the direction mutually perpendicular to the fields. At 100 eV and 4 kG, typical BIGMAK parameters, an electric field δE_θ of 160 V/m produces the same δv_r as $\delta B_r/B_T = 10^{-4}$.

D. Experimental Measurements of Magnetic Field Fluctuations in Tokamaks

The first reported measurements of magnetic field fluctuations in tokamaks were those by Mirnov and Semenov [55]. The measurements were made with coils inside the conducting liner but outside of the plasma column. Helical structures with m=2-6 and n=1 were observed. Oscillations of this type are now routinely observed in tokamaks and are referred to as Mirnov oscillations. They are believed to be caused by rotating magnetic island structures. Different theoretical models [54,56,57] indicate that the island structure should rotate in the toroidal direction at

v_{the} or in the poloidal direction at the electron diamagnetic drift velocity,

$$\underset{\sim}{v}_{De} = -(\underset{\sim}{\nabla}p \times \underset{\sim}{B})/(en_e B^2) \qquad (4.18)$$

Experimental observations of the rotation of an island structure must also take into account the possible rotation of the plasma due to a static radial electric field. The alternate acceleration and deceleration of all the particles in their Larmor orbits leads to the $\underset{\sim}{E} \times \underset{\sim}{B}$ rotation velocity given by

$$v_{\underset{\sim}{E} \times \underset{\sim}{B}} = (\underset{\sim}{E} \times \underset{\sim}{B})/B^2 \qquad (4.19)$$

Measurements of magnetic fields with probes inserted directly into the plasma column have been carried out on several tokamaks. Probes were used to measure the radial current profile and to verify the presence of m=1,2,3 modes in MINIMAK at the University of Tokyo (R=.23 m, a=.06 m, B_T=.7-1.4 kG, I_p=4.3-5.2 kA, T_e=6 eV)[58]. The modes were identified as kink modes and resistive tearing modes. The modes were also seen to propagate in the ion diamagnetic drift direction consistent with an $\underset{\sim}{E} \times \underset{\sim}{B}$ rotation of the plasma column, since the measured space potential of the plasma was positive.

A multicoil probe was used to measure current profiles during disruptive discharges in the Australian LT-3 tokamak [59]. The probe could be inserted approximately two thirds of the minor radius without severely affecting the discharge characteristics such as

total current and loop voltage. A strongly peaked current profile was observed shortly before disruptions, with a redistribution of current from the q=1 surface region to the q=2 surface region.

Magnetic island structures have been mapped out in low temperature discharges in the TOSCA tokamak (R=.3 m, a=.085 m, B_T=4-6 kG, I_p=10-15 kA, T_e=30 eV)[60], where probing .05 m in from the edge was possible without altering global discharge characteristics. Islands with m=2,3,4 and n=1 were observed. The m=2 island reached .03 m in width just prior to major disruptions. The m=3 island saturated with a width of $<$.02 m and $\delta B_r/B_\theta < .03$. Also observed, but not extensively studied, were high frequency fluctuations in the range of 100-400 kHz superimposed on the low frequency modes. The amplitude of these fluctuations was $\delta B_r/B_\theta \tilde{=} .001$, while the cross-field correlation length was on the order of .01 m.

Magnetic islands have also been observed in the fast repetition rate ENCORE tokamak at Caltech (R=.38 m, a=.12 m, B_T=.2-1.5 kG, I_p=.5-6 kA, $n_e = 2 \times 10^{18} m^{-3}$, T_e = 5-10 eV)[61]. The m=2,3 islands have been mapped out and have been seen to correlate strongly with fluctuations in the density as measured by ion saturation current from a Langmuir probe and with fluctuations in the density as measured by a microwave interferometer.

High frequency magnetic field fluctuations have been studied in the MACROTOR tokamak at UCLA (R=.9 m, a=.45 m, B_T = 2-3 kG, I_p = 50 kA, n_e = 10^{18}-$10^{19}m^{-3}$, T_e = 100 eV) using probes [62,63]. The plasma discharge parameters did not change with the insertion of probes up to .15 m into the discharge. There was no rise in UV light emission near the probes. Changes in probe size from .006 m to .02 m in diameter did not affect the spectra of fluctuations below 100 kHz. A low frequency coherent structure at 7 kHz was often observed. The spectra could be characterized by $|\delta B_r| \propto f^{-n}$ with n = 1-2. For the high frequency fluctuations, measurements showed $\delta B_r/B_T \tilde{=} 10^{-4}$-$10^{-5}$. Fluctuations in the poloidal direction were of the same magnitude and had the same general spectral shape as those in the radial direction. The magnitude of fluctuations in the toroidal direction was less than ten percent of the magnitude of the radial or poloidal fluctuations. The fluctuations also showed cross-field correlation lengths $<$.05 m, indicating that they were not due to global modes. The amplitude of the fluctuations was observed to increase proportional to the plasma current at fixed B_T. However, neither the amplitude nor the spectrum changed during gas puffing for n_e increasing from $10^{18}m^{-3}$ to $>5 \times 10^{18}m^{-3}$.

V. EXPERIMENTAL RESULTS

A. Introduction

This chapter is concerned with the results obtained from probe measurements of fluctuating magnetic fields in BIGMAK. The order of presentation follows the ordering of computational techniques given in chapter 3. It is important to note here that all results presented in this chapter are estimates which have been derived from computations on sampled data of finite length. The raw data encompass over 12 Mbytes from 189 discharges. Ensemble averaging is necessarily employed , and the word "typical" is often used in cases where ensemble averaging, or alternatively presentation of all the data available, is not practical.

B. δB_{rms} Calculations

The diffusion coefficients derived from magnetic field fluctuations are very sensitive to the fluctuating field strength, so that accurate measurements are required to compare the theoretical confinement time with the observed confinement time. From the raw signals shown in figure 12, it is easy to see that the fluctuating field strength is maximum near the beginning of the discharge when gas puffing is not employed. Figure 16 shows the typical time evolution of δB_r for discharges without gas puffing. Particular note should be taken of the fluctuating field strength near 7 msec into the discharge.

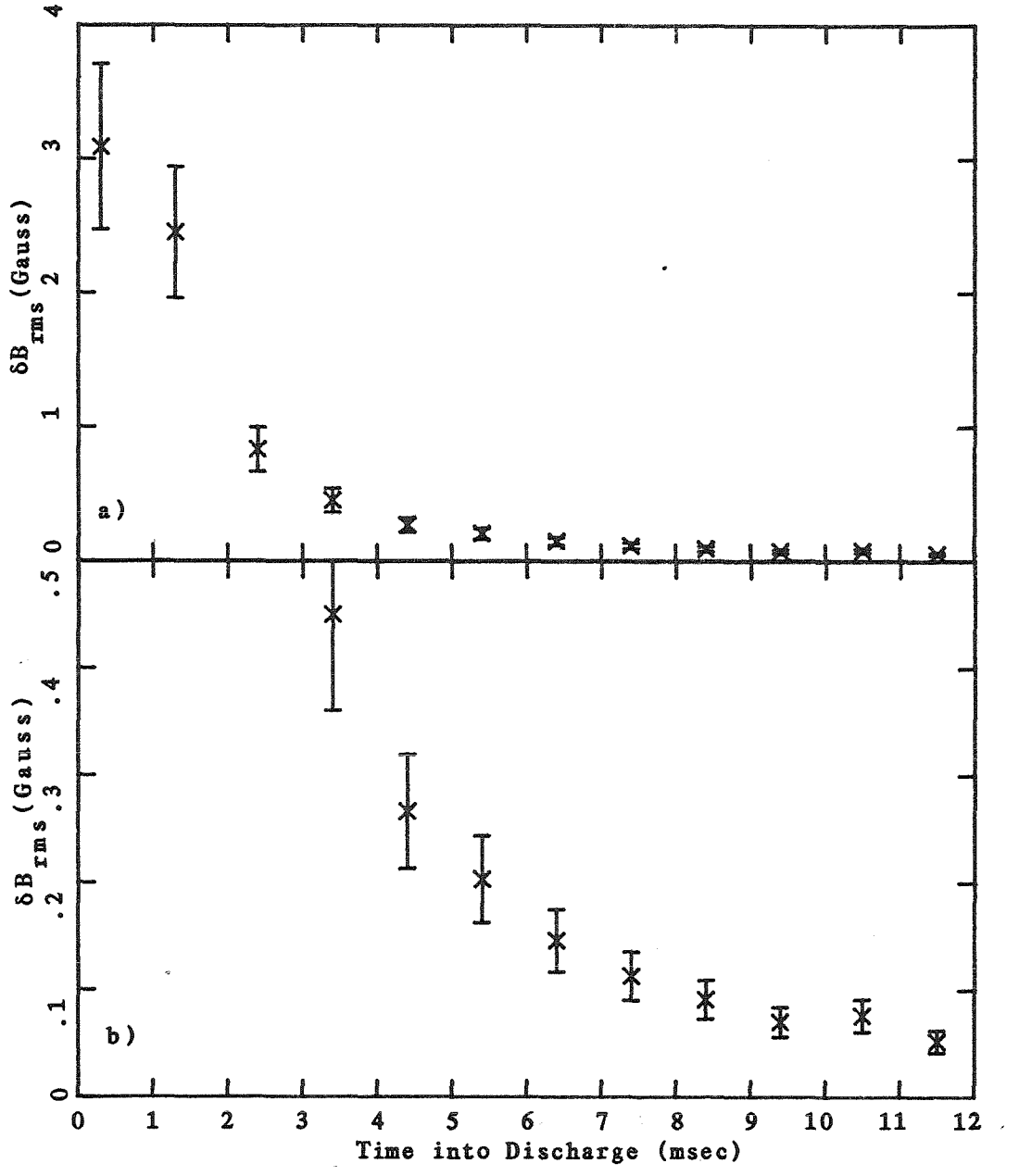

Figure 16. The fluctuating field strength of the radial component versus time into the discharge a) normal scale, and b) expanded scale.

This is the time of maximum plasma current when the measurement of τ_E is made. The measurements shown are for a probe at r = .13 m (.02 m in from the vacuum chamber wall). For the values shown, $\delta B_r/B_T$ at this radius is approximately 4×10^{-5}.

The fluctuating field strength is not observed to depend on the value of q at the edge of the plasma in the range 3.0 - 5.9, or on the plasma current itself in the range 14 kA - 25 kA. This is illustrated in figure 17. The discharges from which these data are taken are adjusted so that the current maximum occurs at approximately 4 msec into the discharge. Comparison beyond t = 5 msec is not possible since the low q discharges terminate in major disruptions at this time. The q value comparisons are obtained by keeping all power supplies constant except for the toroidal field. The global features of the plasma, such as plasma current, loop voltage, and line average density appear to be unchanged unless the toroidal field is so low as to cause disruptions. Precursors in the range of 40 kHz - 200 kHz are observed just prior to these disruptions. The fluctuating field strength is lower during the initial breakdown phase for lower current discharges. However, after the initial density decay, there is no apparent dependence of the fluctuating field strength on plasma current.

The fluctuating field strength is not isotropic. There is no difference in strength between the radial and

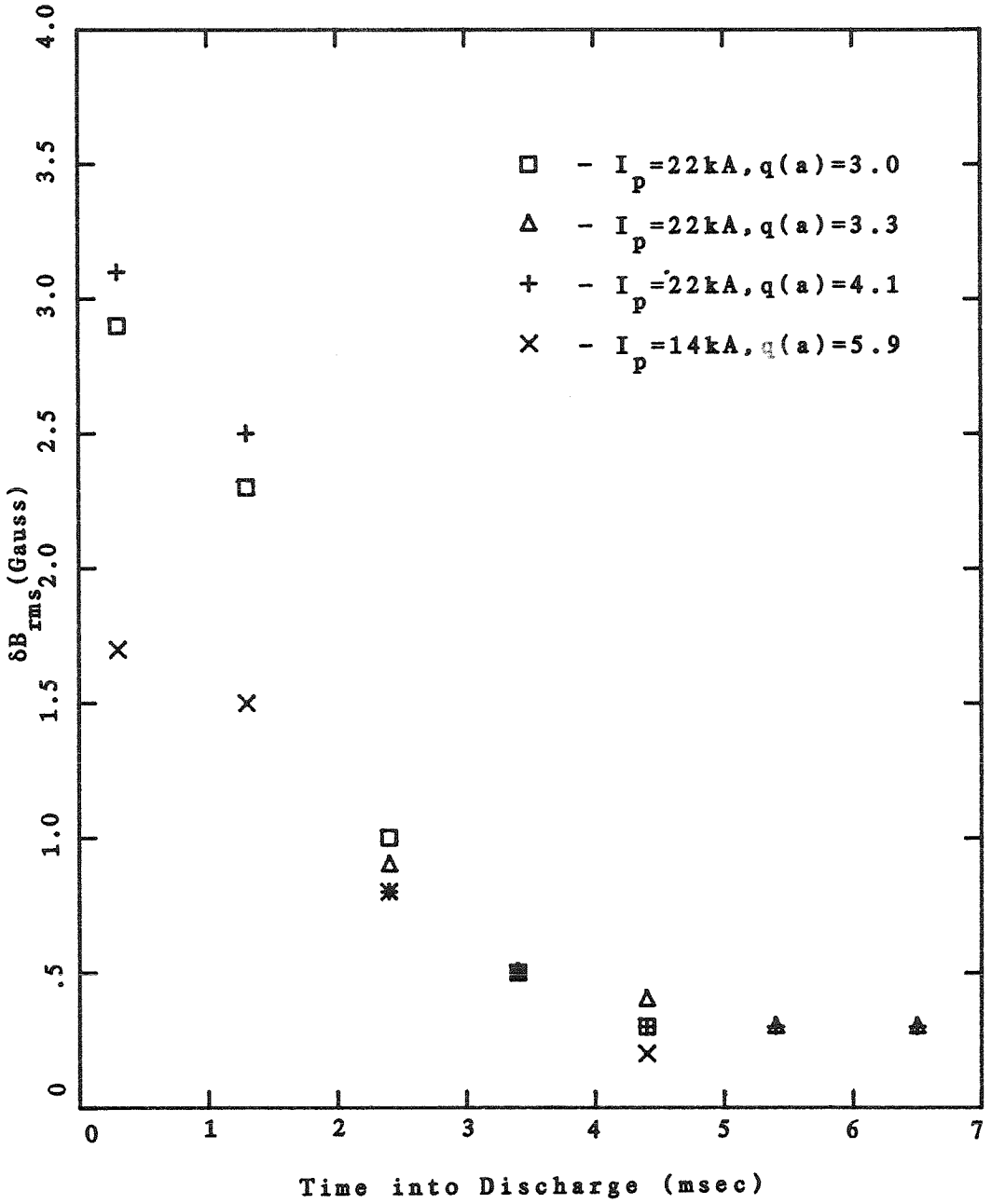

Figure 17. The fluctuating field strength of the radial component versus time into the discharge for various values of q(a) and I_p.

poloidal components of the fluctuating field. However, the toroidal component is at least less than 20 per cent of the other components. The measurements are not inconsistent with a component of fluctuating field along the unperturbed field lines of zero. Two measurement limitations are important here. First, it is difficult to align the probes exactly in the direction of the field lines. More accurate probe construction techniques could avoid this difficulty if the direction of the unperturbed field lines were known. The second limitation, however, makes this unnecessary. Any endeavor to align a stationary probe along the unperturbed field lines will fail since the direction of the unperturbed field lines at any point in the plasma changes during the discharge. This can be easily seen from the fact that the toroidal field strength and plasma current magnitude do not track each other during the discharge, so that the q value at any point in the plasma is constantly changing.

Figure 18 shows the dependence of fluctuating field strength on density during gas puffing. There is a very abrupt increase in the level with the onset of the puff. The loop voltage is only slightly affected by the gas puff. The plasma current is prematurely flattened and subsequently obtains a maximum of only 23 kA versus a maximum of 26 kA which would have been obtained without the gas puff. Hence in estimating τ_E from equation 1.15, the dE/dt term is only slightly changed while the E term

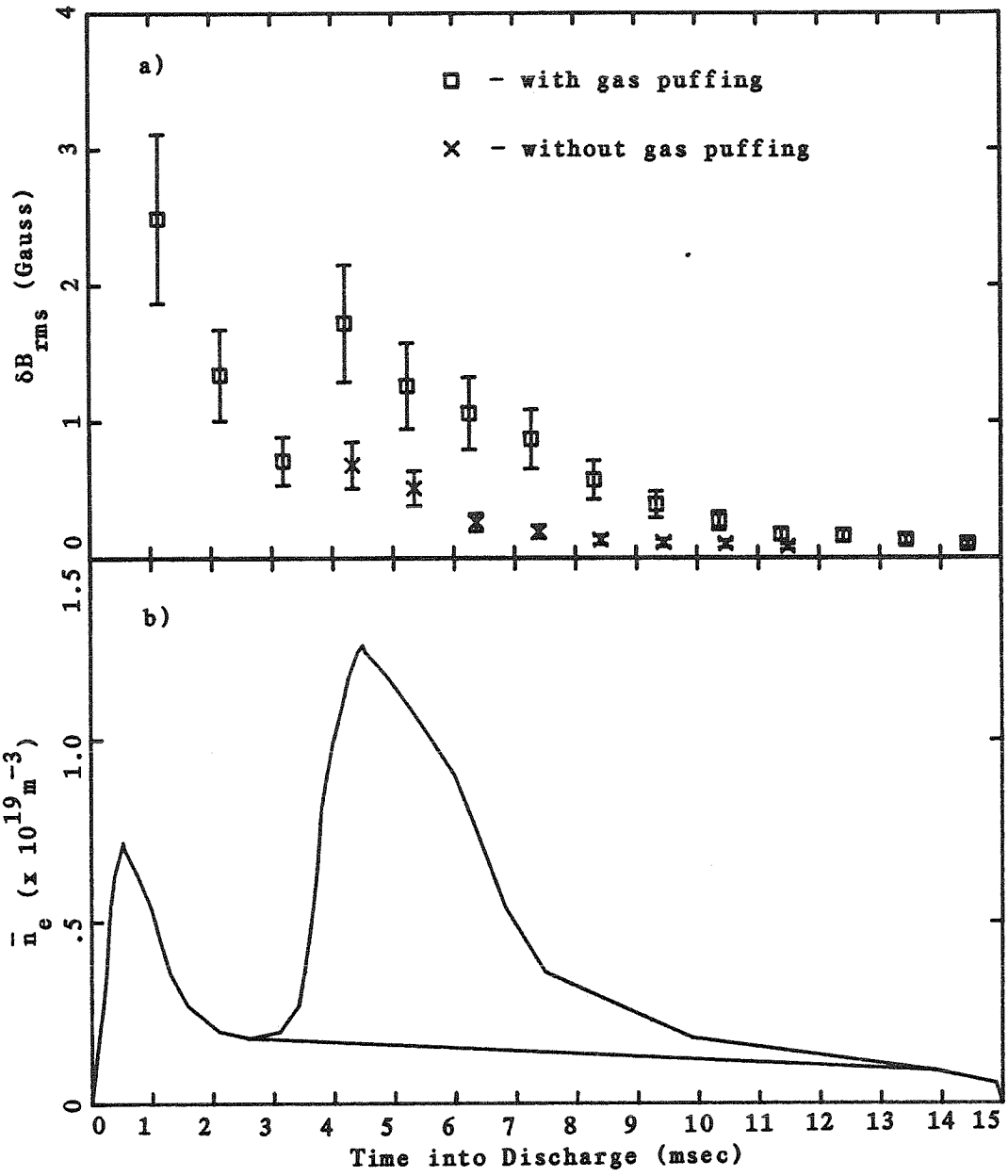

Figure 18. a) The fluctuating field strength of the radial component versus time into the discharge with and without neutral gas puffing. b) The corresponding line average density versus time.

has increased significantly due to the increase in plasma density. An estimate of τ_E from the discharge parameters yields $\tau_E \tilde{=} 1.2$ msec, an increase of approximately a factor of 4 from the non-gas puffing case. This measurement does not support the stochastic field theories of anomalous electron thermal transport in which the energy confinement time should be lower if the fluctuating field level is higher. It should also be noted here that these measurements are not consistent with the results obtained on MACROTOR [62,63], where the fluctuating field strength was observed to depend on I_p and $q(a)$ but not on $\bar{n}_e$.

The dependence of δB_r on minor radius is shown in figure 19. The measurements are made at the time of plasma current maximum, in this case 7 msec into the discharge. Probing beyond .05 m from the edge produces noticeable changes in the plasma current and loop voltage. The vertical field charging voltage must be lowered approximately 5 per cent in order to maintain horizontal position of the plasma when probing between .03 m and .05 m in from the edge. Sharp spikes also develop in the data if the probe is inserted beyond .05 m. Because of these limitations, it is not clear at what radius the fluctuating field strength is maximum. For r = .10 m, the value of $\delta B_r/B_T$ for this series of discharges is 2.3×10^{-4}. If the data are extrapolated to r = a/2 = .075 m, a level of $\delta B_r/B_T \tilde{=} 3.5 \times 10^{-4}$ is

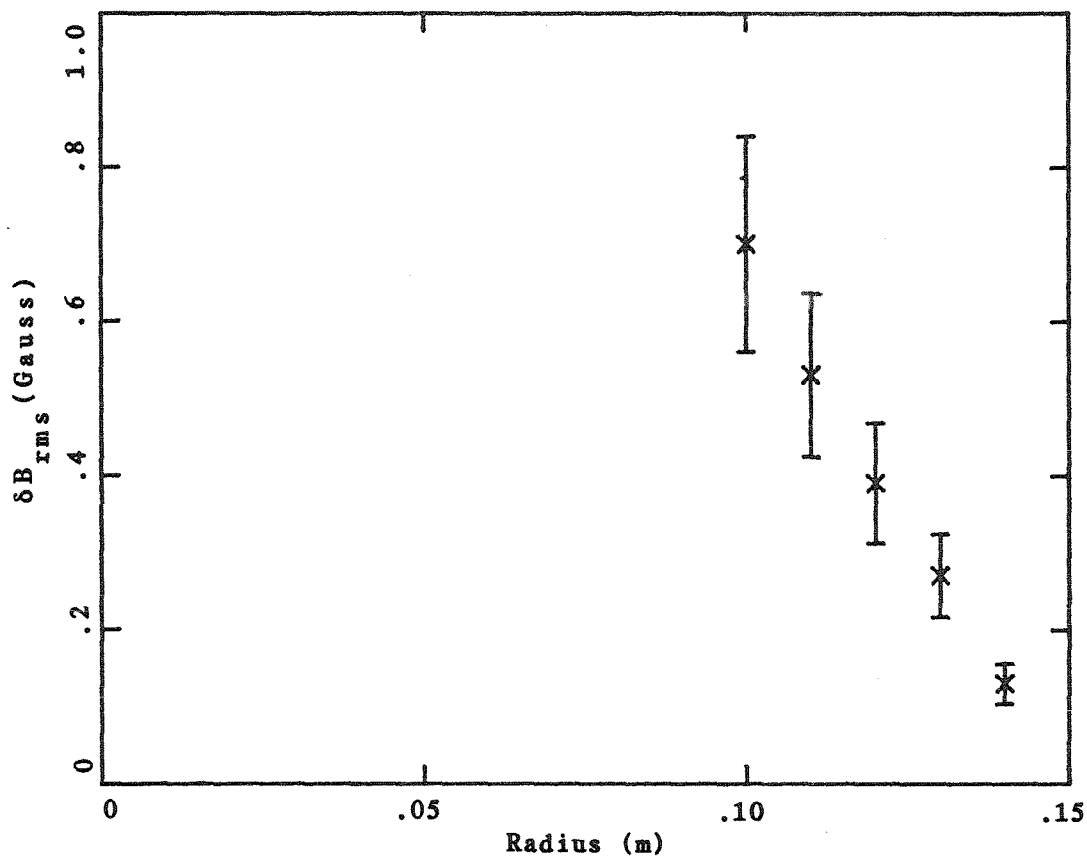

Figure 19. The fluctuating field strength of the radial component versus radius at the time of maximum current (t = 7 msec).

obtained. This is a factor of six smaller than the level estimated in equation 4.13 to be necessary to explain the observed energy confinement time in BIGMAK.

C. Probability Density Estimates

Figure 20 shows the probability density as computed for a typical 1 Kbyte record of raw data. The distribution is very indicative of Gaussian random noise. Distributions of this sort are observed throughout the discharge, with the width of the distribution dependent on the signal strength and amplifier gain settings.

D. Correlation Estimates

The magnetic field fluctuation diffusion coefficients, while being strongly dependent on the fluctuating field strength, are also dependent on the toroidal correlation length of the fluctuations. Measurements of the correlation lengths of the fluctuations in the poloidal, radial, and toroidal directions are presented here as well as the results of correlating a radial signal with a poloidal signal. All correlations presented in this section are from signals recorded near the time of maximum plasma current. Figure 21 shows a series of correlations between two coils measuring the radial component of fluctuating field separated poloidally from .01 m to .04 m. Figure 21a-d shows the correlation function for signals where no dominant low frequency was

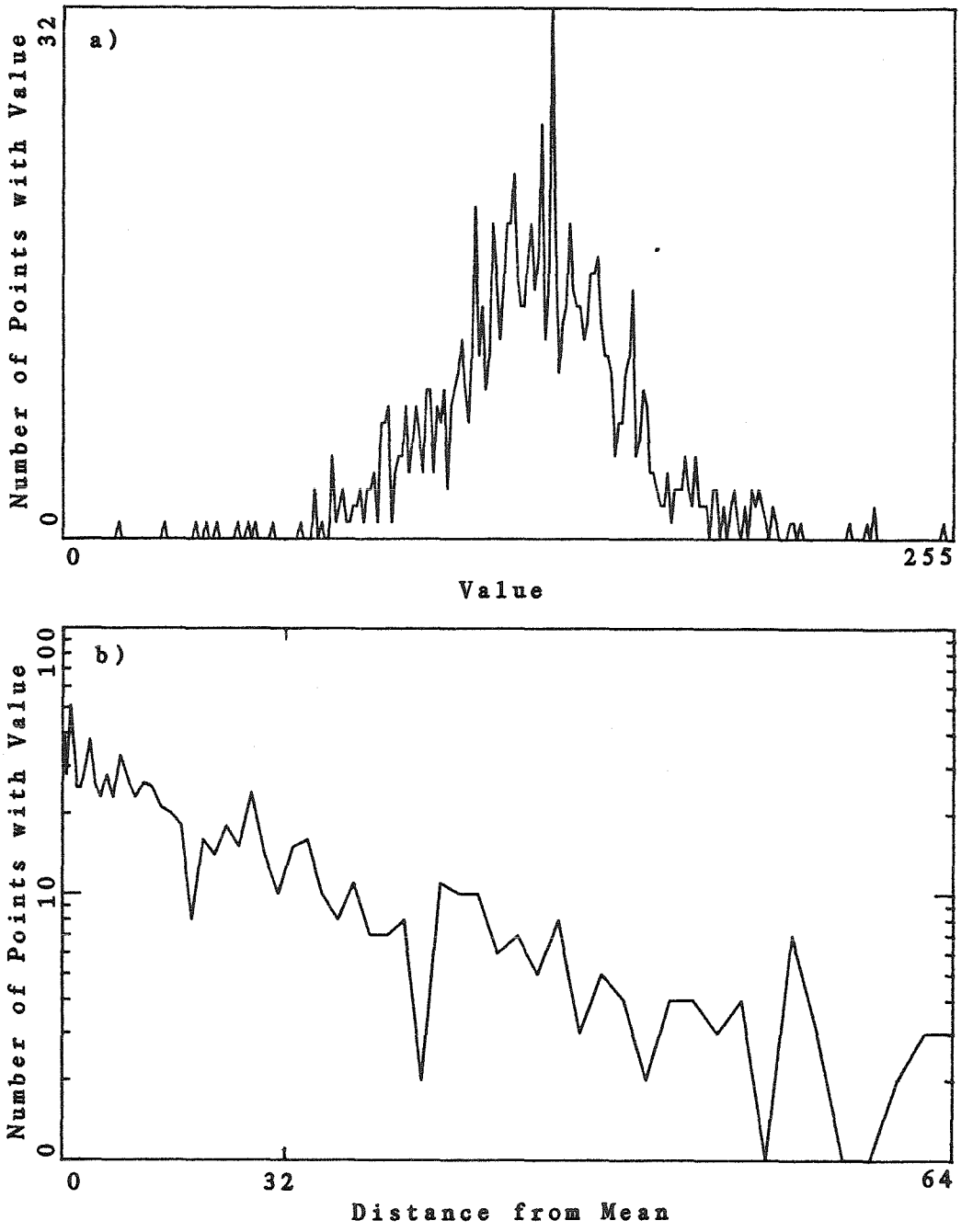

Figure 20. a) The probability density function for a typical signal. b) The logarithm of the probability density function versus the square of the distance away from the mean. A straight line fit indicates a Gaussian profile.

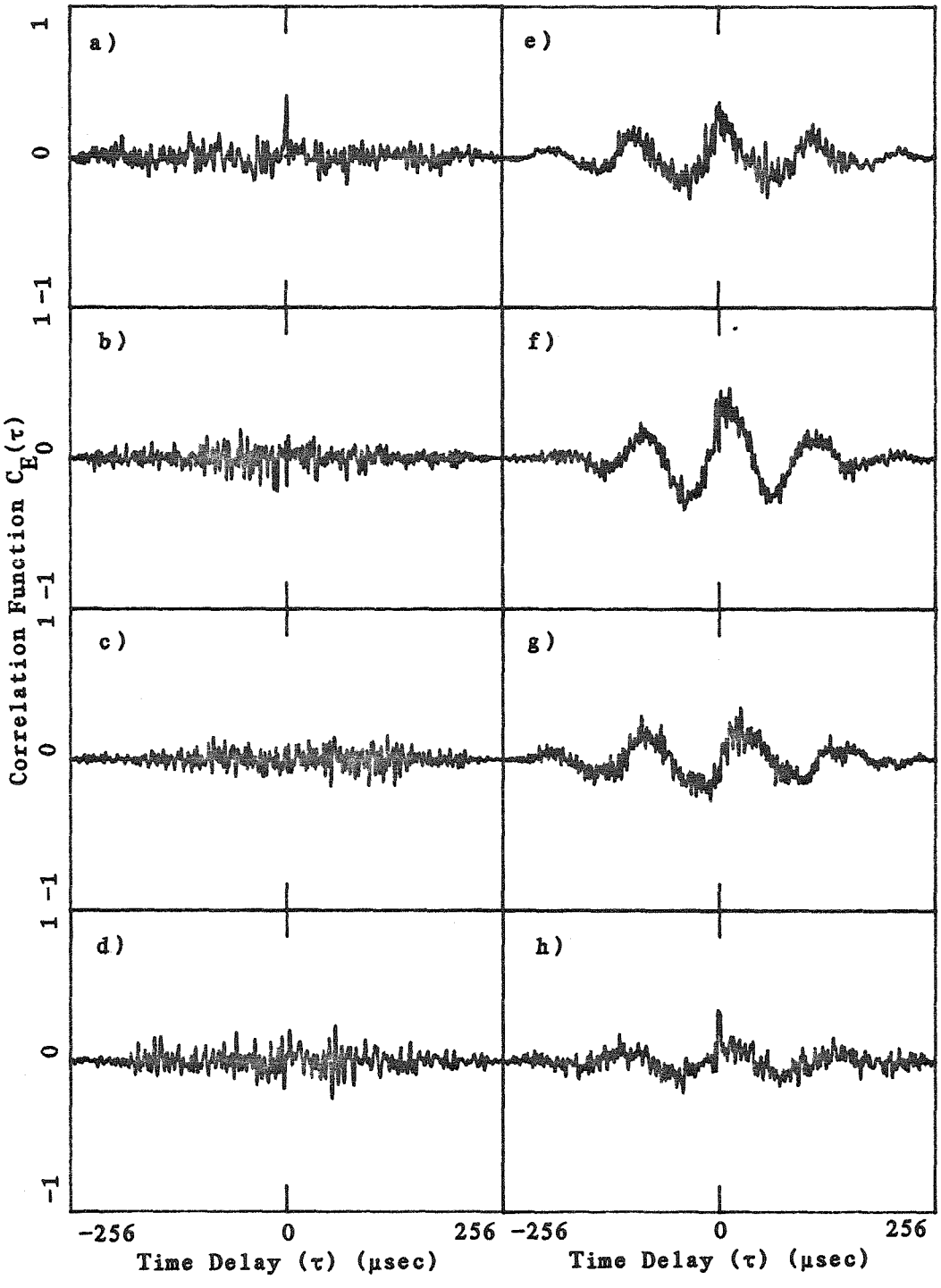

Figure 21. The correlation function for signals from probes separated poloidally a) .01 m, b) .02 m, c) .03 m, d) .04 m, e) .01 m, f) .02 m, g) .03 m, and h) .01 m. No low frequency mode is present in the signals for a)-d). A low frequency mode of approximately 20 kHz is present in the signals for e)-g). In h), a low frequency mode of 16 kHz is present, and a broadband correlation peak is also present.

present in the signal. The signal shows mild correlation at .01 m and no correlation for .02, .03, and .04 m separation, indicating a poloidal correlation length of the order of .01 m. Figure 21e-g shows the correlation function for signals with a low frequency component of approximately 20 kHz. The strength of the correlation depends on the relative strength of the low frequency mode with respect to the background signal. The shift in the peak as the probes are separated indicates an apparent poloidal rotation velocity of 2.4×10^3 m/sec in the electron diamagnetic drift direction. The term "apparent" is appropriate since the measurements made have not differentiated between a poloidal rotation of the plasma and a toroidal rotation of the plasma. If a large-scale MHD disturbance such as a magnetic island were to be observed with 2 probes, the observation would be similar to that of viewing a moving screw through a narrow slot. One cannot ascertain whether the screw is rotating on its axis or is moving longitudinally along its axis or both. Figure 21h shows the correlation function for signals from probes separated .01 m poloidally. In this case correlation of both a low frequency mode, at approximately 16 kHz, and the broadband signal can be seen. The peak in the function due to the broadband signal is not shifted from zero time, while the low frequency peak is shifted 7.7 μsec corresponding to an apparent poloidal rotation velocity of 1.3×10^3 m/sec.

The correlation function for the radial component of signals from coils separated .04 m radially is shown in figure 22. Since severe probe damage occurs for probes without a stainless shield inserted more than .02 m into the plasma, these signals are obtained from two coils inside a probe with a slotted stainless steel shield as shown in figure 8. The peak in the correlation function for a .04 m coil separation would appear to indicate a long correlation length in the radial direction, which is in contrast to the shorter correlation lengths for poloidal separation of coils as shown in figure 21. However, this apparent correlation is probably due to a coupling of the measurement coils due to the presence of the stainless steel shield. This can be demonstrated quite simply with the following test. Consider an experiment in which the fluctuating field is provided not by the plasma, but by a simple wire loop 25 mm in diameter whose axis coincides with the longitudinal axis of the probe. The following table presents the results of such an experiment in which a signal of arbitrary amplitude at 100 kHz (the results have been observed to be the same over the range 100 kHz - 1 MHz) is imposed on the loop. The voltages are those measured across the coils at various longitudinal distances from the loop with and without the shield present.

Distance along axis from loop	Without shield	With shield
0 m	150 mV	100 mV

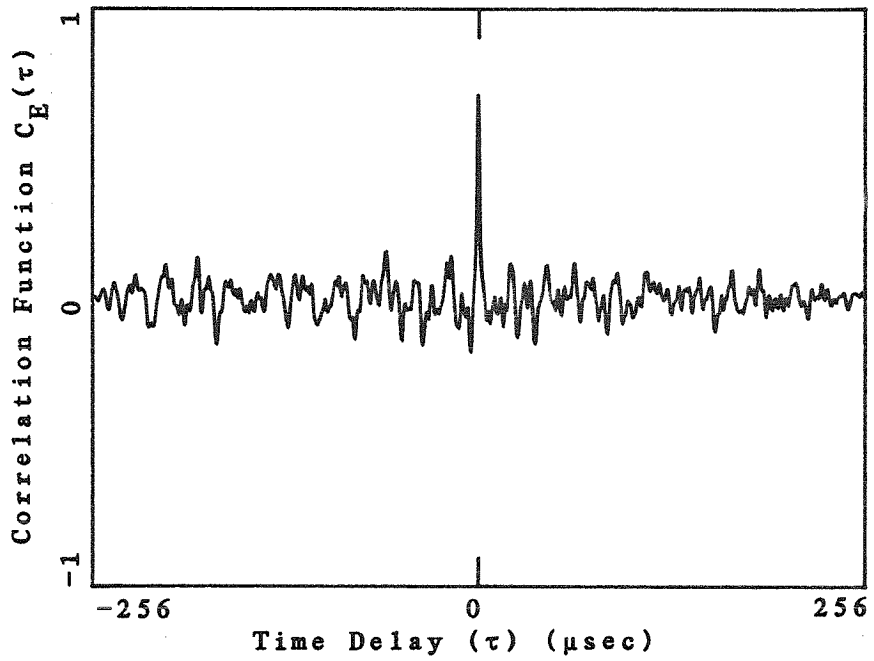

Figure 22. The correlation function for radial component signals from coils separated radially .04 m. The apparent correlation is probably due to distortion of the measured fields by the slotted stainless steel shield.

0.01 m	85 mV	76 mV
0.02 m	36 mV	50 mV
0.03 m	18 mV	30 mV
0.04 m	10 mV	18 mV

These results can be explained in terms of a spreading of the induced eddy currents on the inside surface of the shield. These eddy currents provide the field seen by the coils. The distortion of the field by the shield could couple the coils in such a way that the fluctuations appear well correlated over distances of .04 m when, in fact, they may not be. Thus, the probe is not appropriate for measuring radial correlation lengths.

The case of toroidal separation of probes measuring the radial component of fluctuating magnetic field is illustrated in figure 23. As in the case of poloidal separation >.01 m, there appears to be correlation only for low frequency modes (38 kHz for the case shown). A scan of correlation amplitude versus toroidal separation has not been made due to the limited port access on BIGMAK. The two probes from which the signals of figure 23 are taken are separated by .36 m ($\pi R/4$), which is the distance between adjacent ports. For q(a)=4, the unperturbed field lines twist .025 m poloidally between the ports, so that the lack of correlation may be related to an effective poloidal separation of .025 m.

Figure 24 shows the results of correlating a radial component signal with a poloidal component signal at the

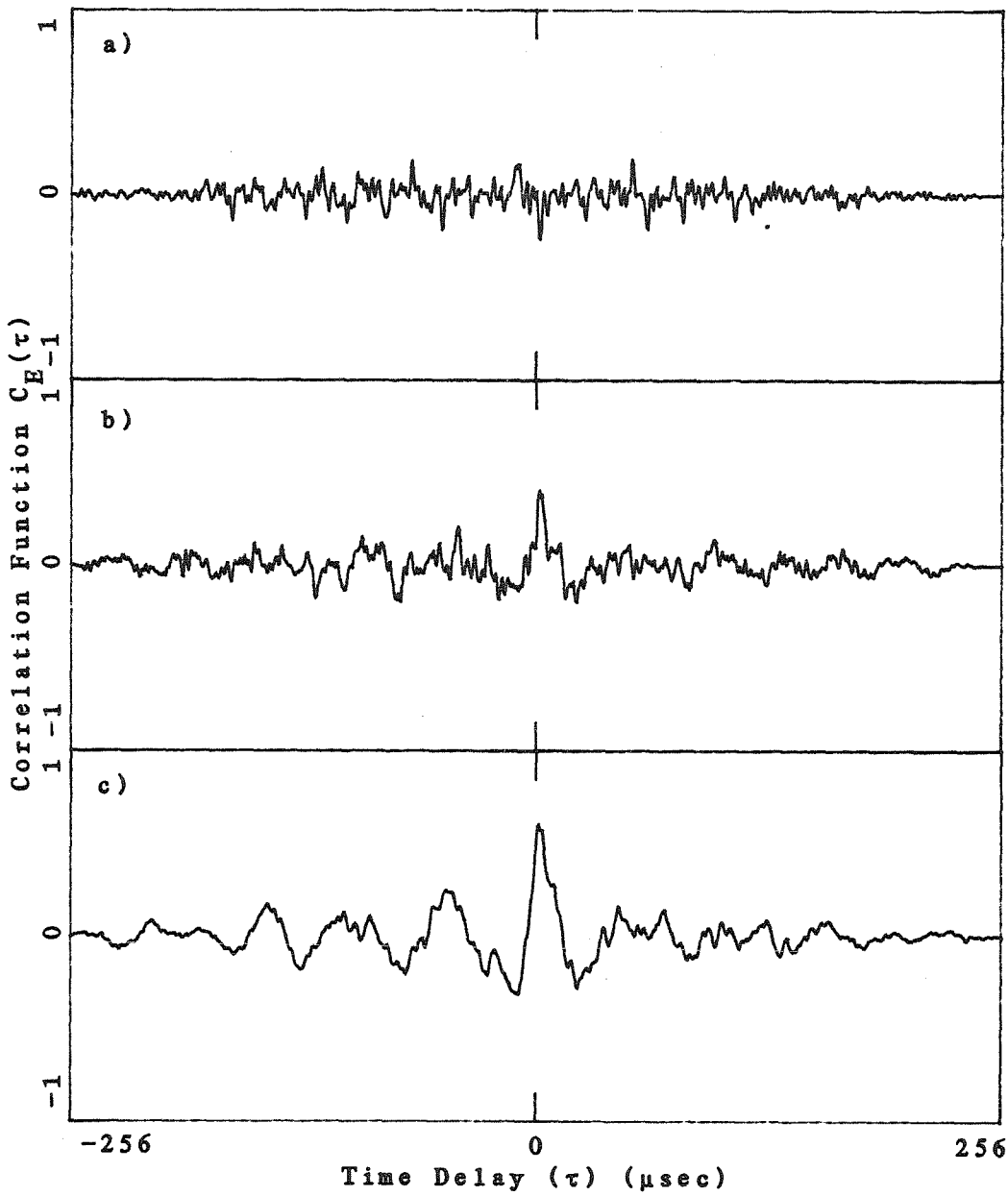

Figure 23. The correlation function for signals from probes separated toroidally .36 m, with a) no low frequency present in the signals, b) a small amplitude low frequency present in the signals, and c) a 38 kHz mode present in the signals.

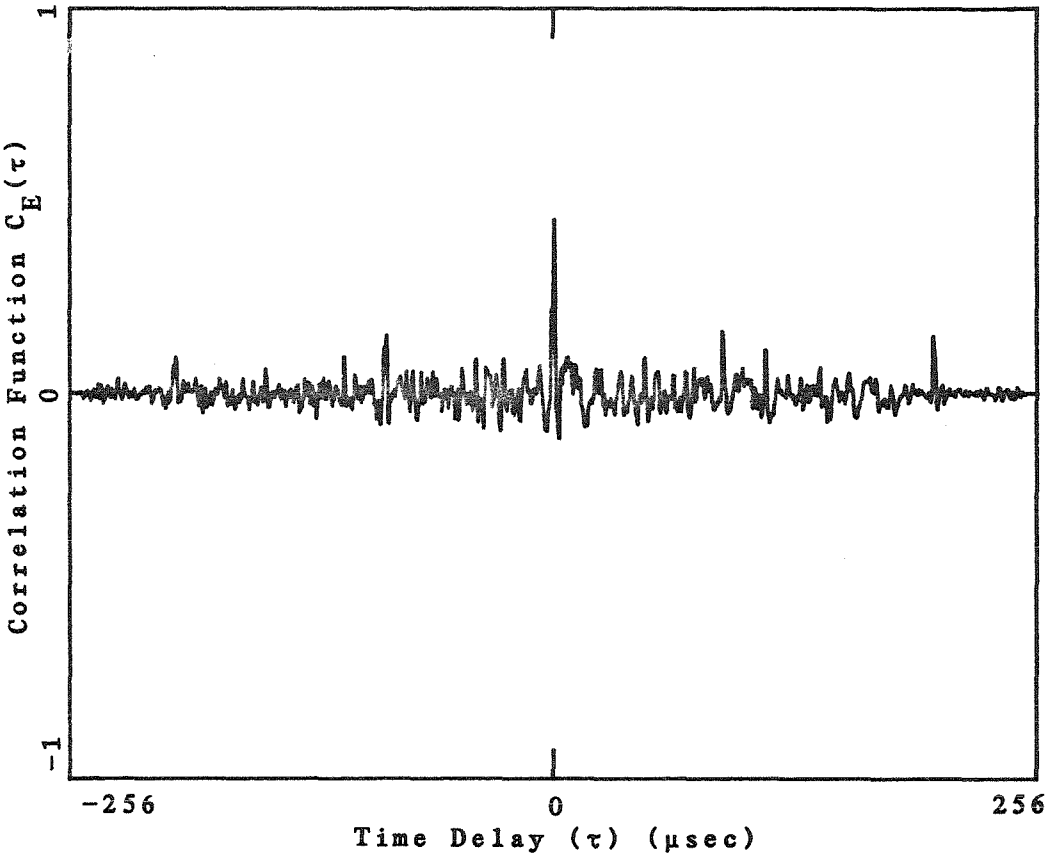

Figure 24. The correlation function for two signals, one of which is the radial component of fluctuating field and the other of which is the poloidal component at the same location.

same point. The signals exhibit a mild correlation. Although the axes of the coils may not be exactly perpendicular to each other due to coil winding errors, this effect would not account for the peak in the correlation function. If the radial and poloidal components were totally uncorrelated, a misalignment of 30^{o} would be required to explain the observed correlation amplitude.

Some further interpretation of these correlation results will be given in the next section along with the discussion of the coherence function.

E. Power Spectral Density Estimates

Estimates of the fluctuation power spectral density amplitude, phase, and coherence versus various parameters are presented in this section. Evidence is presented near the end of the section to divide the spectral density into two portions - a low frequency portion up to approximately 100 kHz normally dominated by large-scale MHD modes, and a high frequency portion which in noiselike in character.

The time development of the spectral density amplitude is shown in figure 25. Since the signals are of $\dot{B}(t)$, the spectral density is of $\delta\dot{B}^2(f)$. For this particular discharge, a strong 50 kHz mode can be seen to decay as the discharge progresses. The high frequency portion of the spectral density also decreases in amplitude with time. However, if this portion of the spectrum is

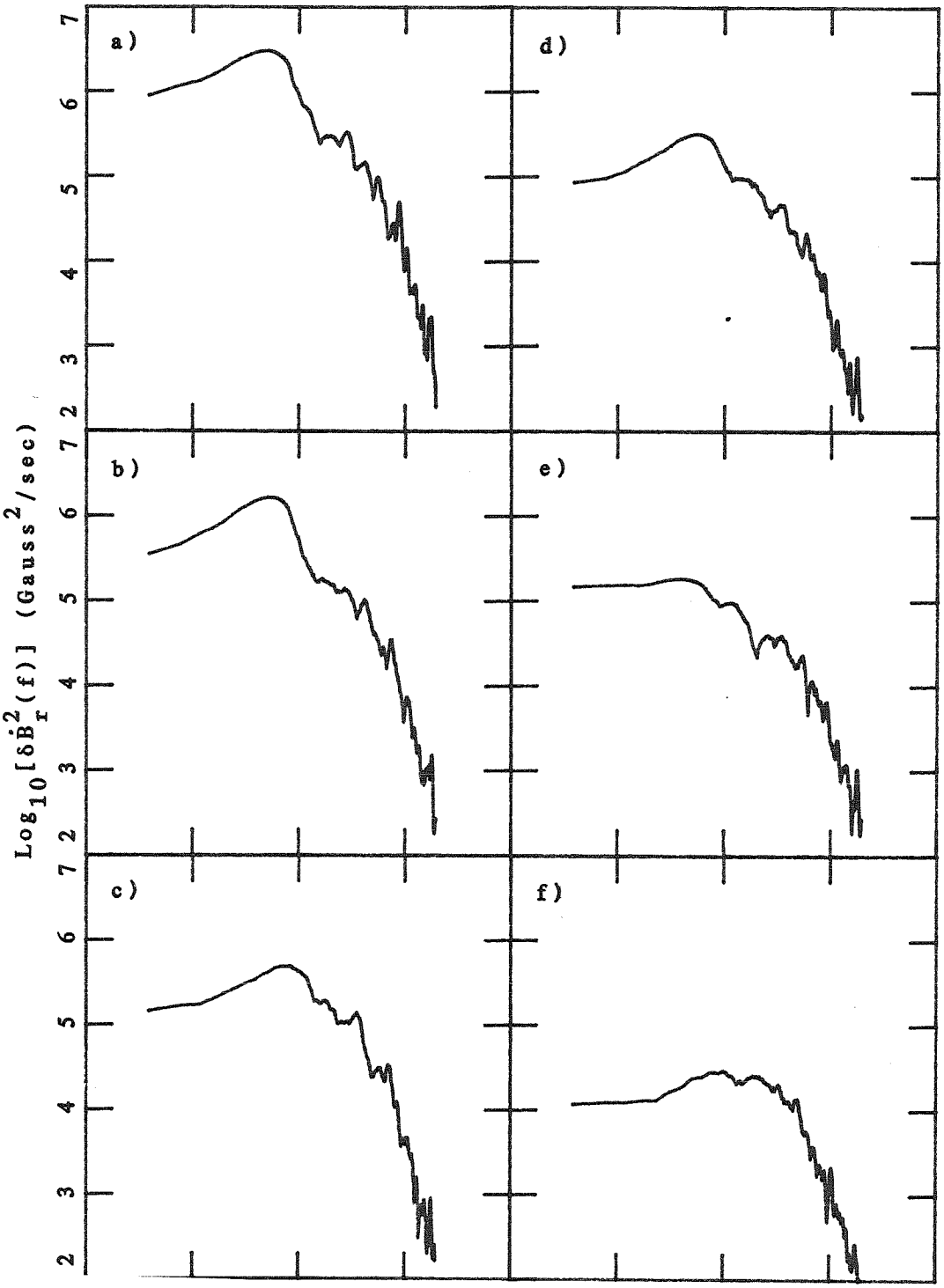

Figure 25. The spectral density amplitude versus time into the discharge for a radial component signal .02 m from the wall, with t = a) 3.9 msec, b) 4.9 msec, c) 6.2 msec, d) 7.2 msec, e) 8.5 msec, and f) 11.3 msec.

characterized by its slope, then it remains essentially unchanged. The slope of the 300 kHz - 1 MHz region corresponds to a dependence of δB_r on frequency of $f^{-\alpha}$ with $\alpha = 2.7$ for all the cases shown. This frequency range is chosen to be well above the low frequency MHD modes yet below the frequency at which the instrumentation rolls off. The slope has been seen to vary from $\alpha = 2$ to $\alpha = 4$. However, $\alpha = 2.3 - 2.7$ is most frequently observed.

In figure 26, the spectrum of figure 25c has been converted to a spectrum of $\delta B(f)$ and $\delta B^2(f)$ by multiplying by the function $(2\pi f)^{-2}$, since $\dot{B} = \omega B$, and in the former case, taking the square root. The fluctuating field magnitude can be obtained from figure 26b quite simply by applying Parseval's theorem,

$$\int_{-T}^{T} B^2(t)dt = 2\int_{0}^{f_{max}} |B(f)|^2 df \qquad (5.1)$$

The point of this discussion is that most of the fluctuating field strength can be seen to originate in the low frequency portion of the spectrum. If the low frequency portion of the spectrum is attributable to well correlated MHD modes, then it will not contribute to transport as predicted by stochastic field theories. Typically 90 per cent of the fluctuating field strength is due to coherent low frequency phenomena.

Figure 27 shows several spectra derived from discharges with different values of I_p and $q(a)$. There

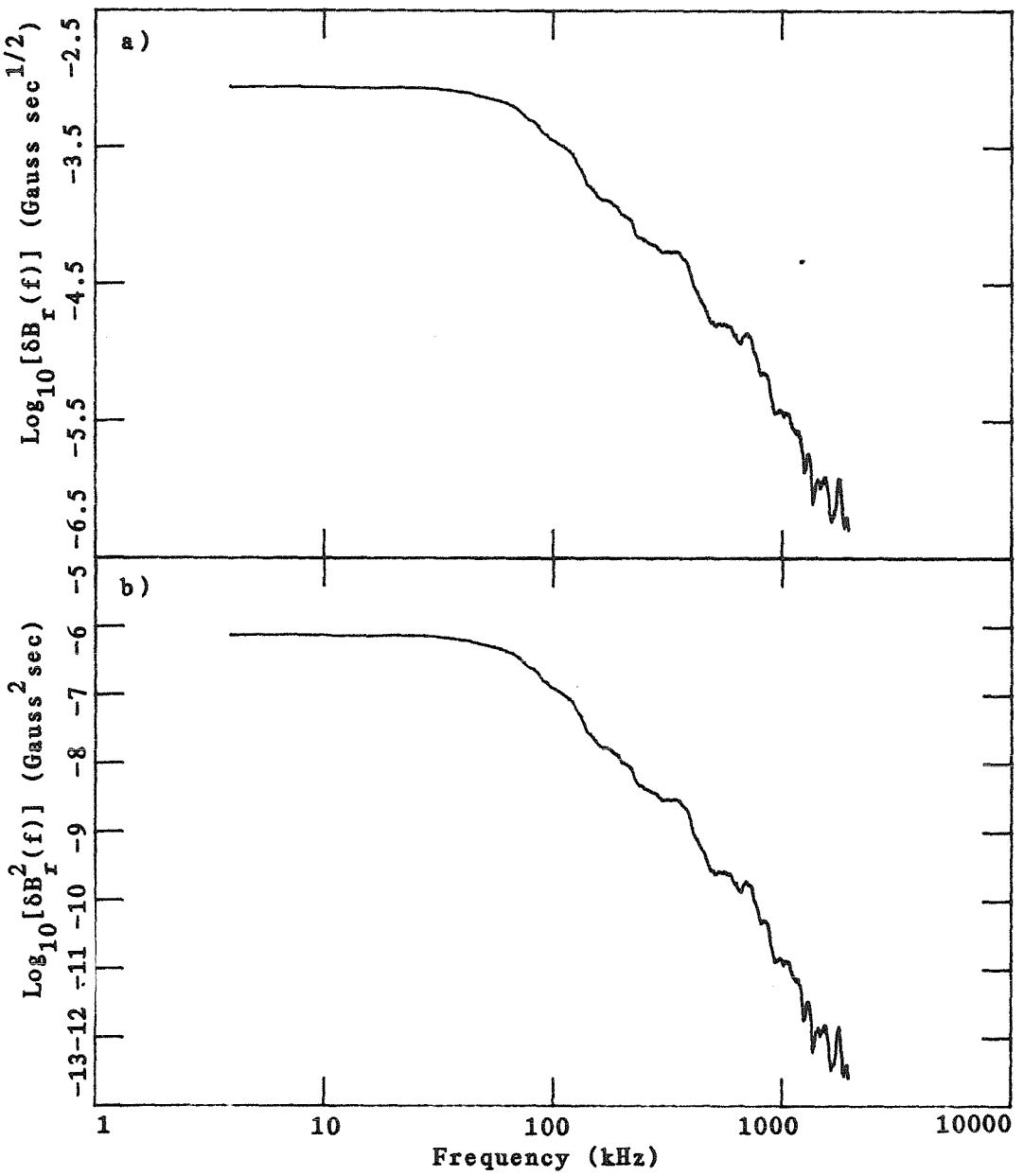

Figure 26. The spectral density amplitude for $\delta B(f)$ and $\delta B^2(f)$ for the radial component of field. The frequency roll-off of δB in the 300 kHz - 1 MHz range is $f^{-2.7}$.

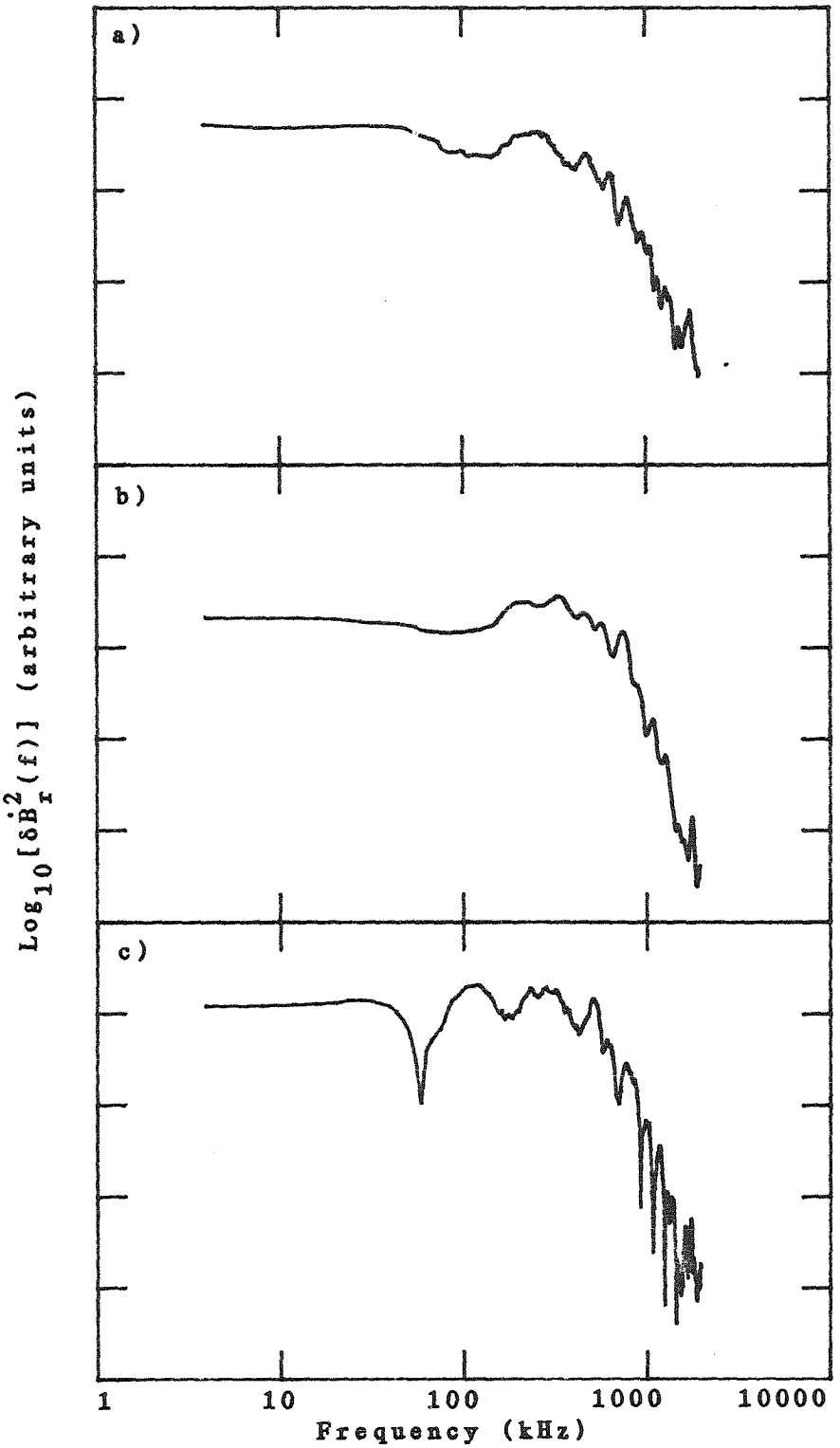

Figure 27. The spectral density amplitude for a) I_p = 22 kA, q(a) = 4.1, b) I_p = 22 kA, q(a) = 3.0, and c) I = 14 kA, q(a) = 5.9. The vertical units are arbitrary in order to compare at equal amplitudes.

is no obvious dependence of the spectra on these parameters for I_p varying from 14 kA to 25 kA and q(a) varying from 3.0 to 5.9. All the spectra shown are from a radial coil located .02 m from the wall.

A comparison of the spectral density amplitude of the radial and poloidal components of fluctuating field is shown in figure 28. A strong peak near 26 kHz can be seen in both spectra, with the poloidal component stronger than the radial component. This peak is probably a coherent MHD mode, although a firm identification is not possible from the experimental setup. The portions of the spectra above 100 kHz, however, are similar, with a dependence of δB on frequency of $f^{-2.6}$ for the region 300 kHz - 1 MHz.

The dependence of the spectral density amplitude on $\bar{n}_e$ is illustrated in figure 29. The amplitude for all frequencies decreases with time until the onset of the gas puff. As the density increases, the fluctuations are dominated by the low frequencies below 30 kHz. Low frequency modes in the 20 kHz - 50 kHz range normally dominate until the density has decayed to near pre-puff levels. However, the amplitude of the high frequency portion of the spectrum also rises, so that the basic spectral shape above 100 kHz is unchanged. The dependence of δB_r on frequency in the 300 kHz - 1 MHz range is approximately $f^{-2.3}$ throughout most of the discharge shown in figure 29.

The dependence of the spectral density amplitude on

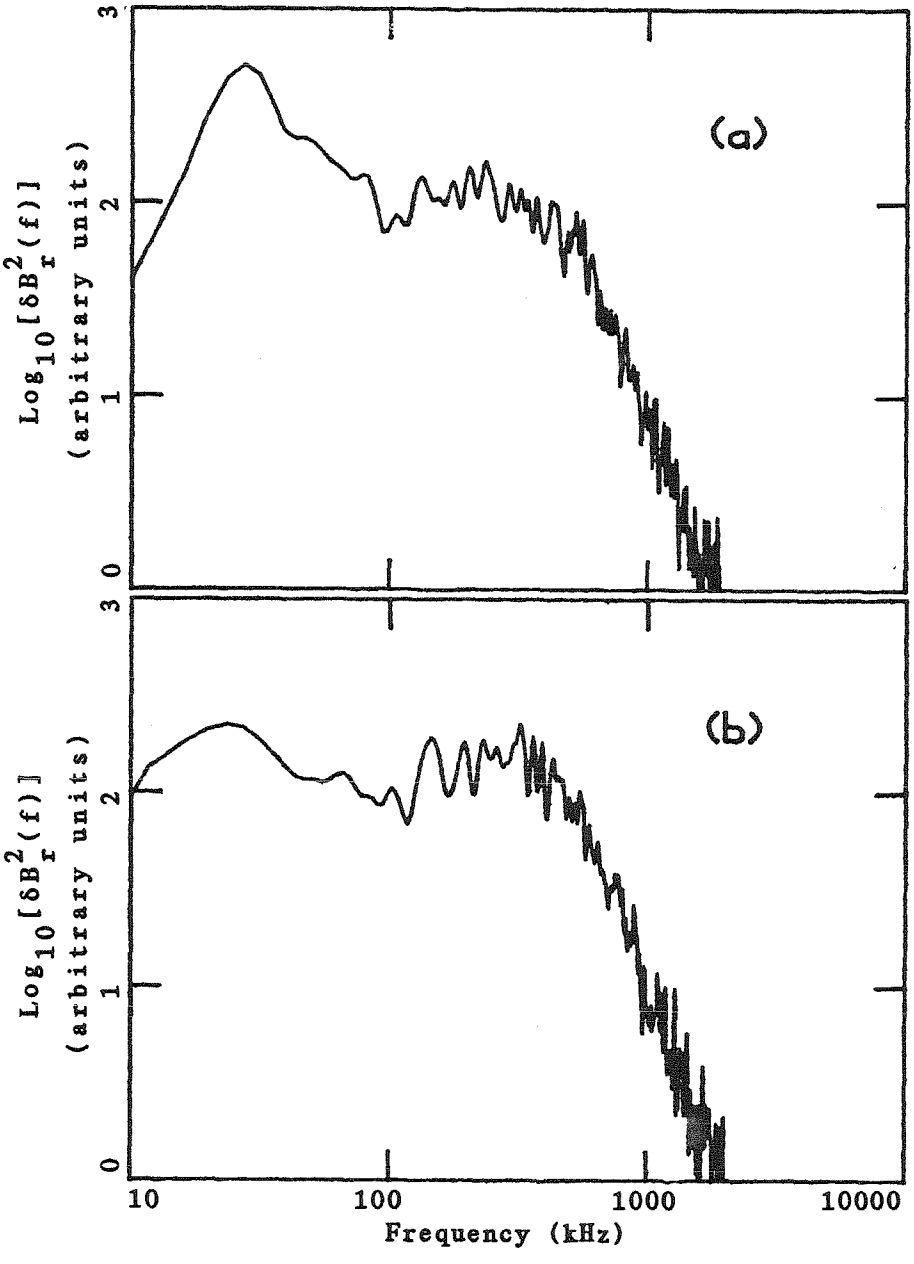

Figure 28. The spectral density amplitude for a) the poloidal component of signal and b) the radial component of signal.

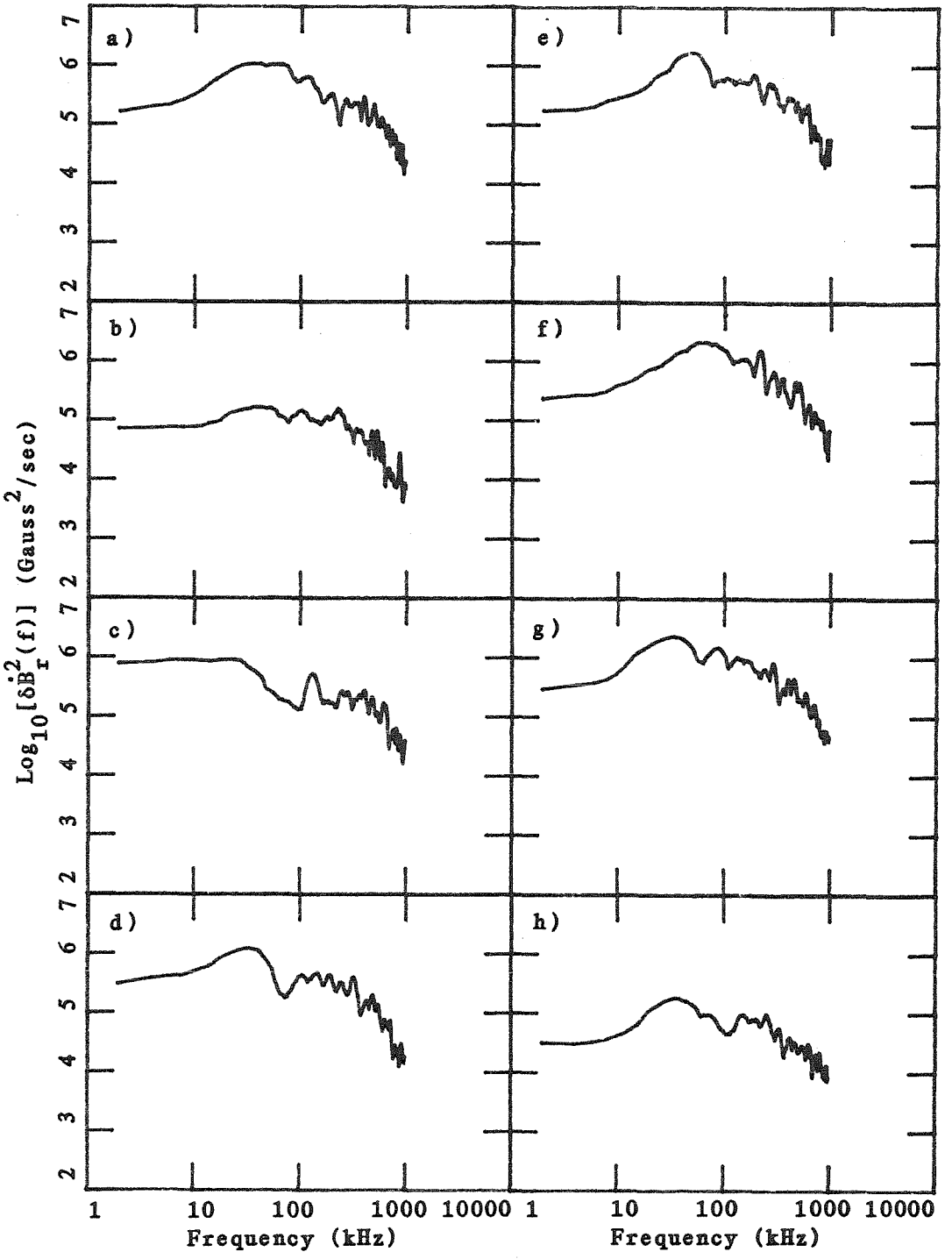

Figure 29. The spectral density amplitude of the radial component of signal versus time for a discharge with gas puffing. The times are t = a) 2.9 msec, b) 3.4 msec, c) 4.0 msec, d) 4.5 msec, e) 5.0 msec, f) 5.5 msec, g) 6.0 msec, and h) 10.0 msec. The spectra are from the same discharge from which the density versus time trace of figure 18b is developed.

radius is illustrated in figure 30. The amplitude at all frequencies increases as the radius decreases, including the strong peak at 50 kHz. The high frequency portion of the spectrum, while changing in amplitude, does not change in shape. For the case shown, the dependence of δB_r on frequency in the range 300 kHz - 1 MHz is approximately $f^{-2.4}$.

All of the spectra presented so far have been very similar. Although the amplitudes vary, and some spectra have been more dominated by low frequency modes than others, all of the spectra exhibit a roll-off at high frequencies corresponding to a dependence of δB_r on frequency of $f^{-\alpha}$ with $\alpha = 2 - 4$. A series of experiments was carried out in which the coil size, probe size, probe surface presented to the plasma, and frequency response of the acquisition system were varied in order to eliminate these factors as agents causing the observed roll-off. Figure 31 shows the results of varying the coil diameter by a factor of 2. The spectra, obtained during the same discharge, are nearly identical. Figure 32 shows the results of varying the probe size and surface. Increasing the probe diameter by a factor of 2.5 and changing the surface in contact with the plasma from Pyrex to stainless steel does not affect the roll-off characteristics of the spectra. Finally, figure 33 shows the results of obtaining the data with an acquisition system in which the response of the probe, preamplifier,

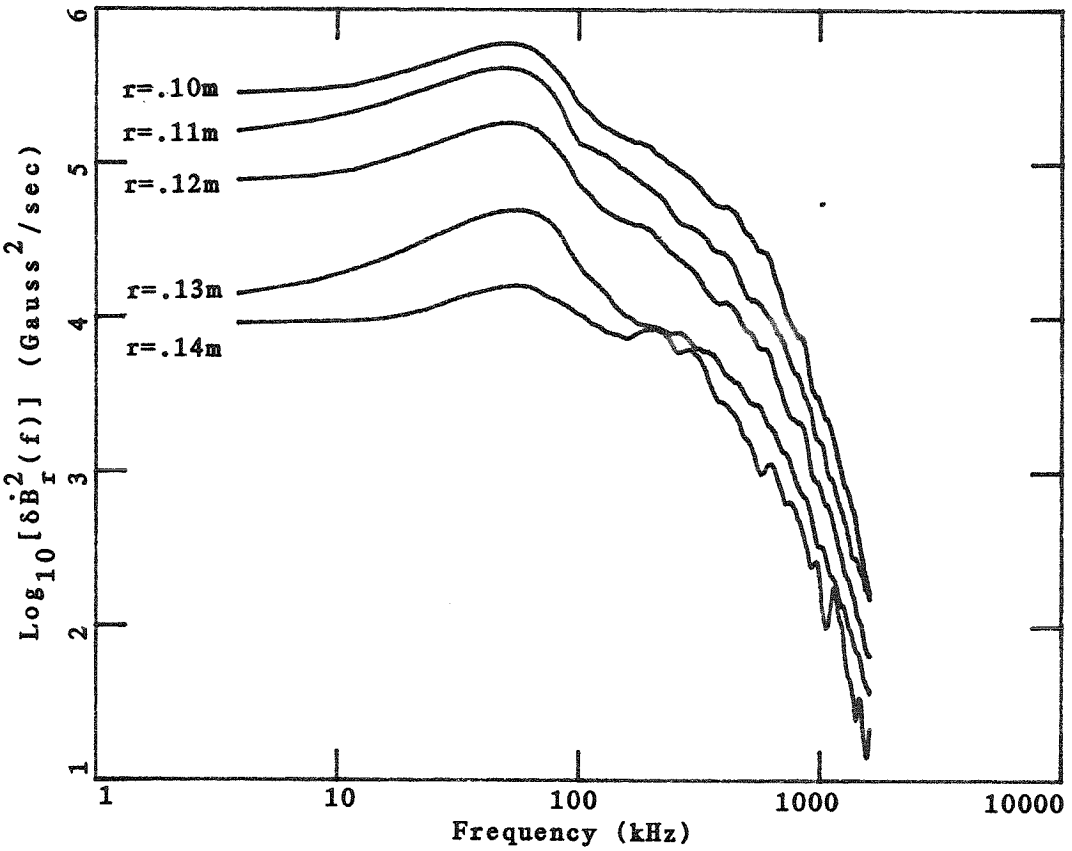

Figure 30. The spectral density amplitude of the radial component of signal versus radius at the time of maximum plasma current (t = 7 msec).

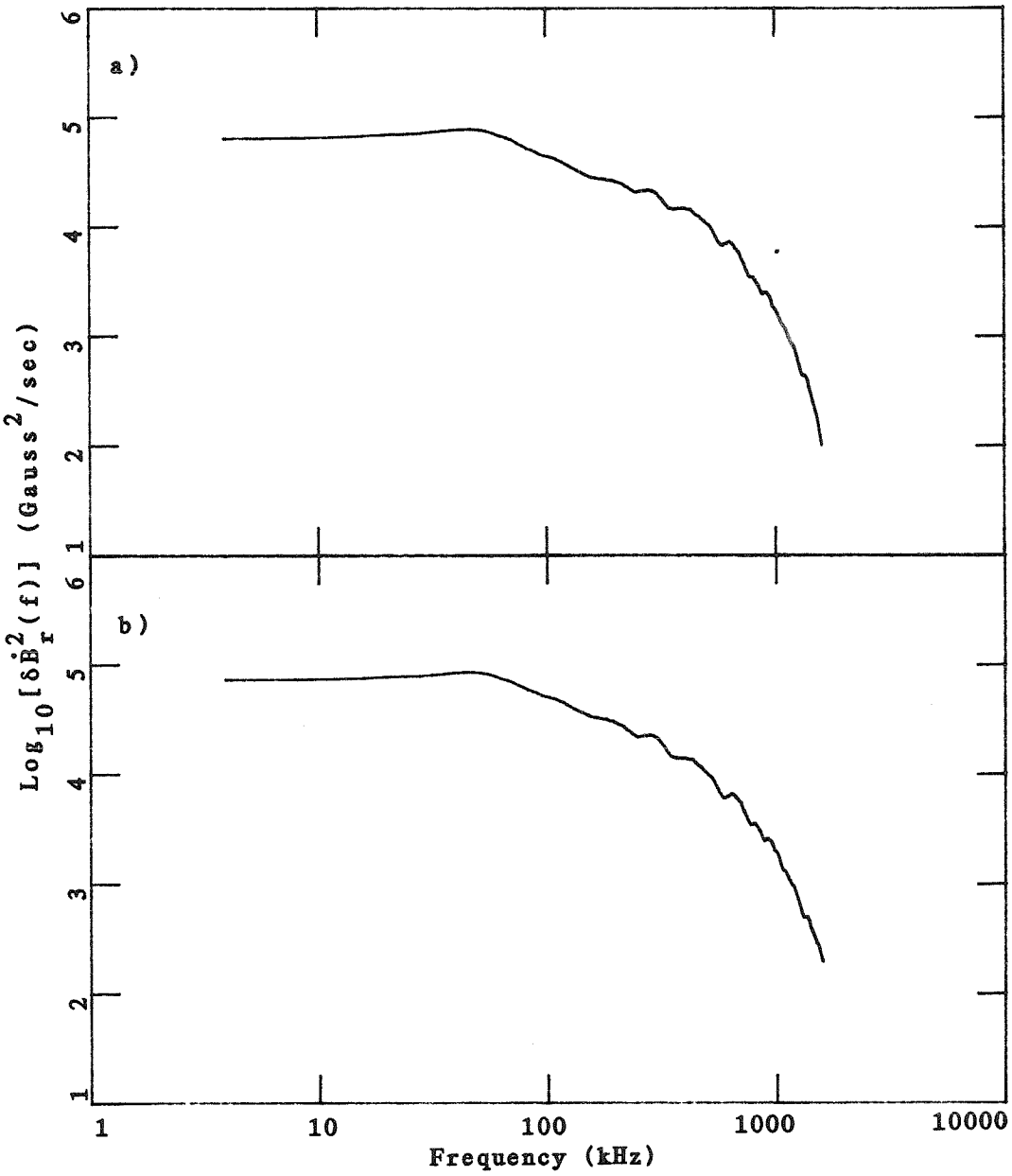

Figure 31. The spectral density amplitude for the radial component of signal for a) a coil 3 mm in diameter, and b) a coil 6 mm in diameter.

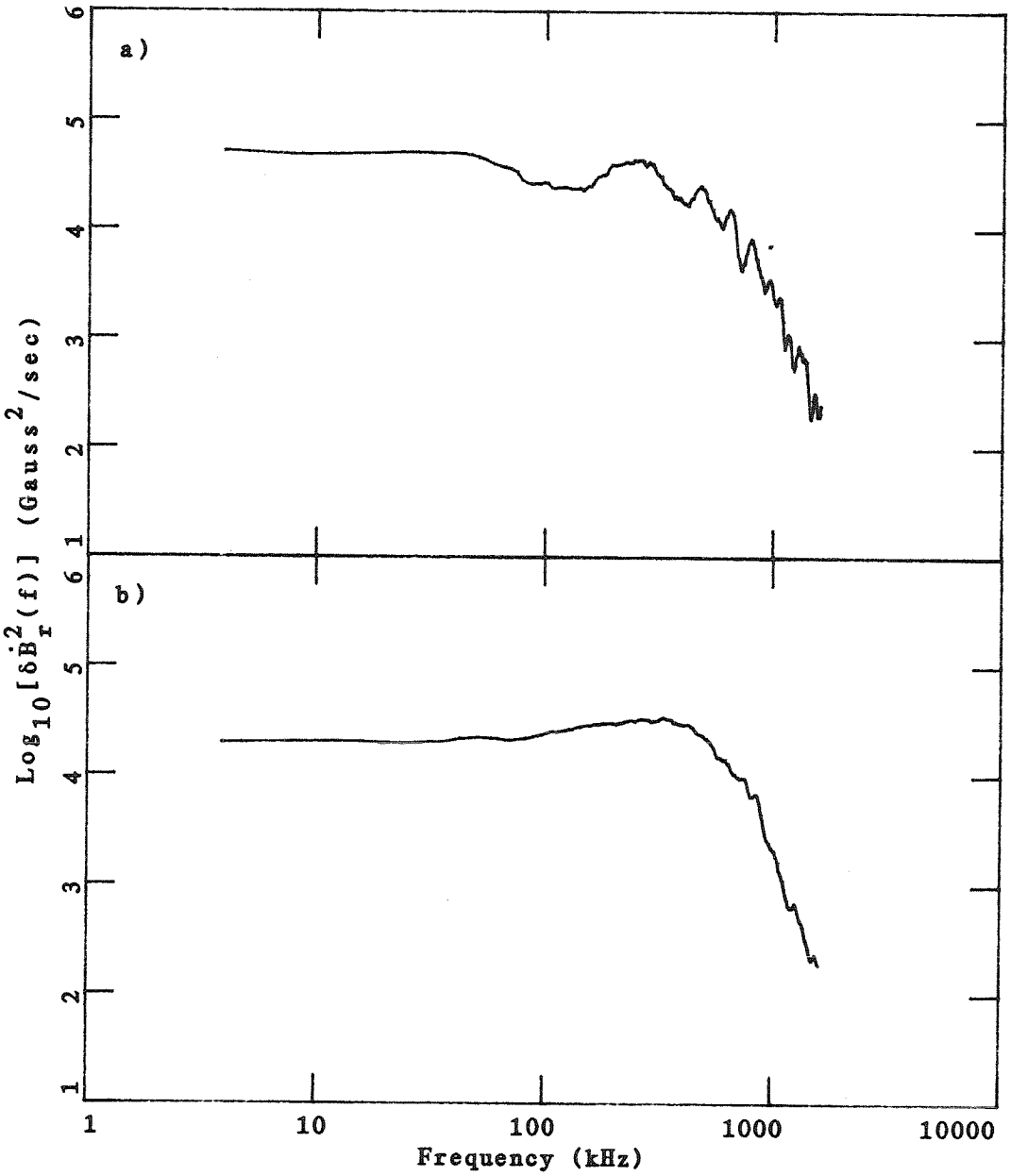

Figure 32. The spectral density amplitude for the radial component of signal for a) a probe 6 mm in diameter with Pyrex in contact with the plasma, and b) a probe 15 mm in diameter with a slotted stainless steel jacket in contact with the plasma.

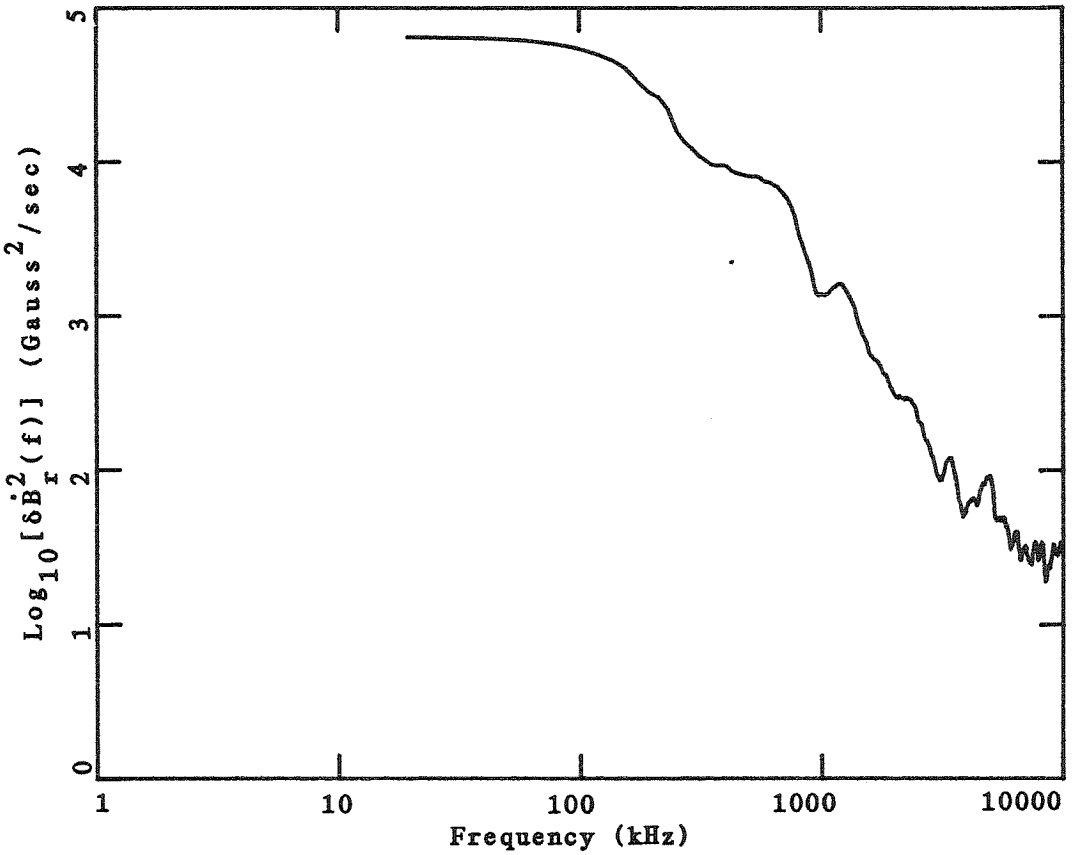

Figure 33. The spectral density amplitude for the radial component of signal obtained using an acquisition system with a flat response to within 5 per cent up to 10 MHz. The value at 10 MHz is approximately equal to the noise level of the system.

and digitizer combination is flat within 5 per cent to 10 MHz. Such a system has a higher noise level than the system normally employed. For the case shown in figure 33, the spectral density amplitude at 10 MHz is approximately equal to the system noise level. The roll-off, however, is not changed from the cases in which the system bandwidth is less by a factor of 6. Hence, the roll-off is a roll-off in the fluctuations and not a roll-off in the instrumentation.

When the spectral density is computed from two different probe signals, the phase and coherence (provided frequency or ensemble averaging is performed) can become non-constant functions of frequency. In figure 34, the spectral density amplitude, phase, and coherence are shown for signals from two radial probes separated .01 m poloidally. For the amount of frequency averaging employed (56 kHz full width half maximum), a coherence value of approximately .3 indicates incoherence. The coherence function is significantly higher than this only in the low range of frequencies, particularly at 32 kHz. The phase becomes a more nearly random function of frequency as the coherence function decreases. The various peaks in the amplitude spectrum are not reproducible except for the peak at 32 kHz. A series of coherence functions for various poloidal probe separations is shown in figure 35, and the value of the coherence function for the peak and various frequency bands has been reduced to figure 36. If a value

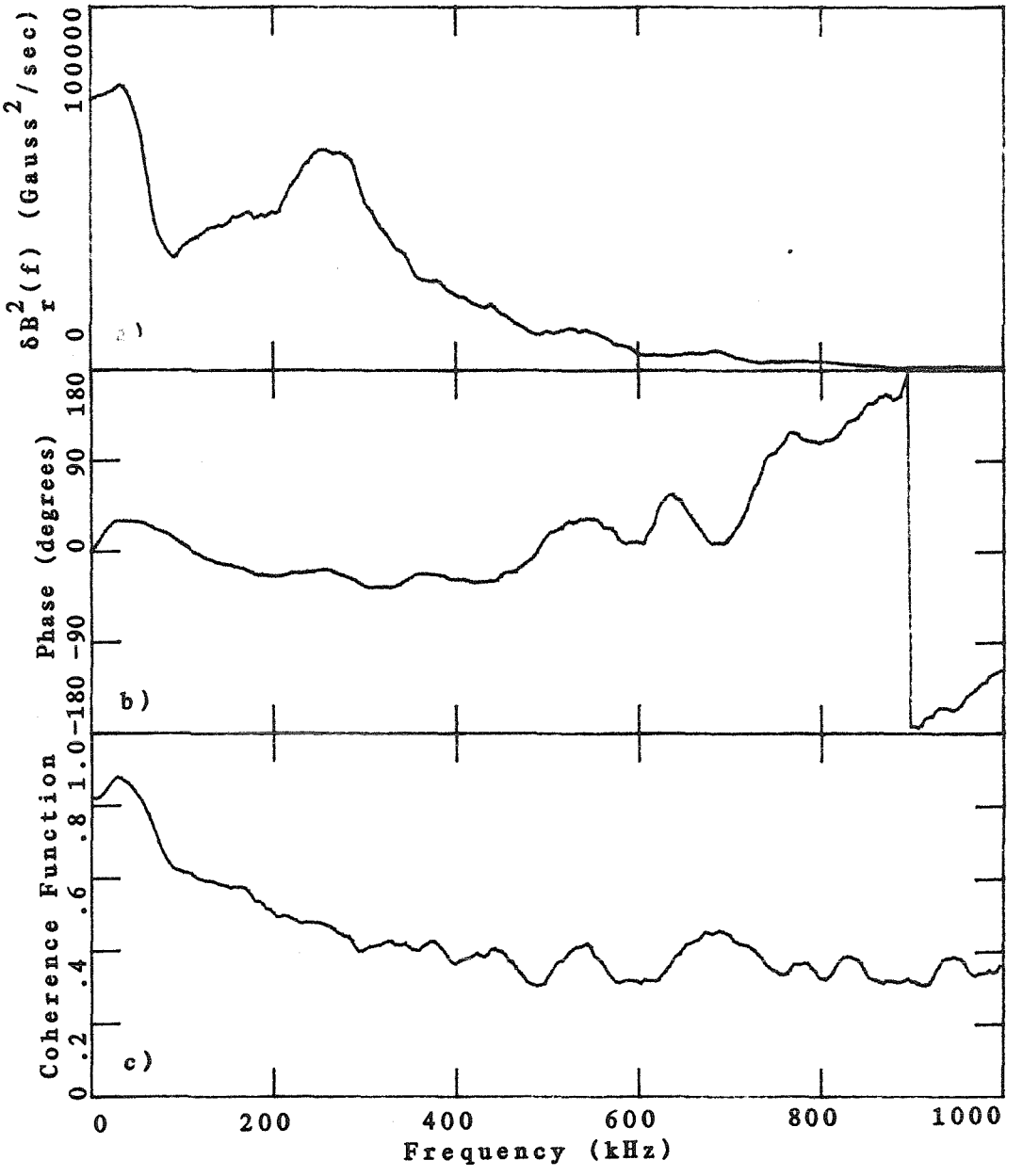

Figure 34. The spectral density amplitude (linear scale), phase, and coherence function computed from two radial component signals from probes separated .01 m poloidally .02 m from the wall. The peak near 250 kHz has a low coherence value and is not reproducible. A coherence value of .3 indicates total incoherence for the amount of averaging employed.

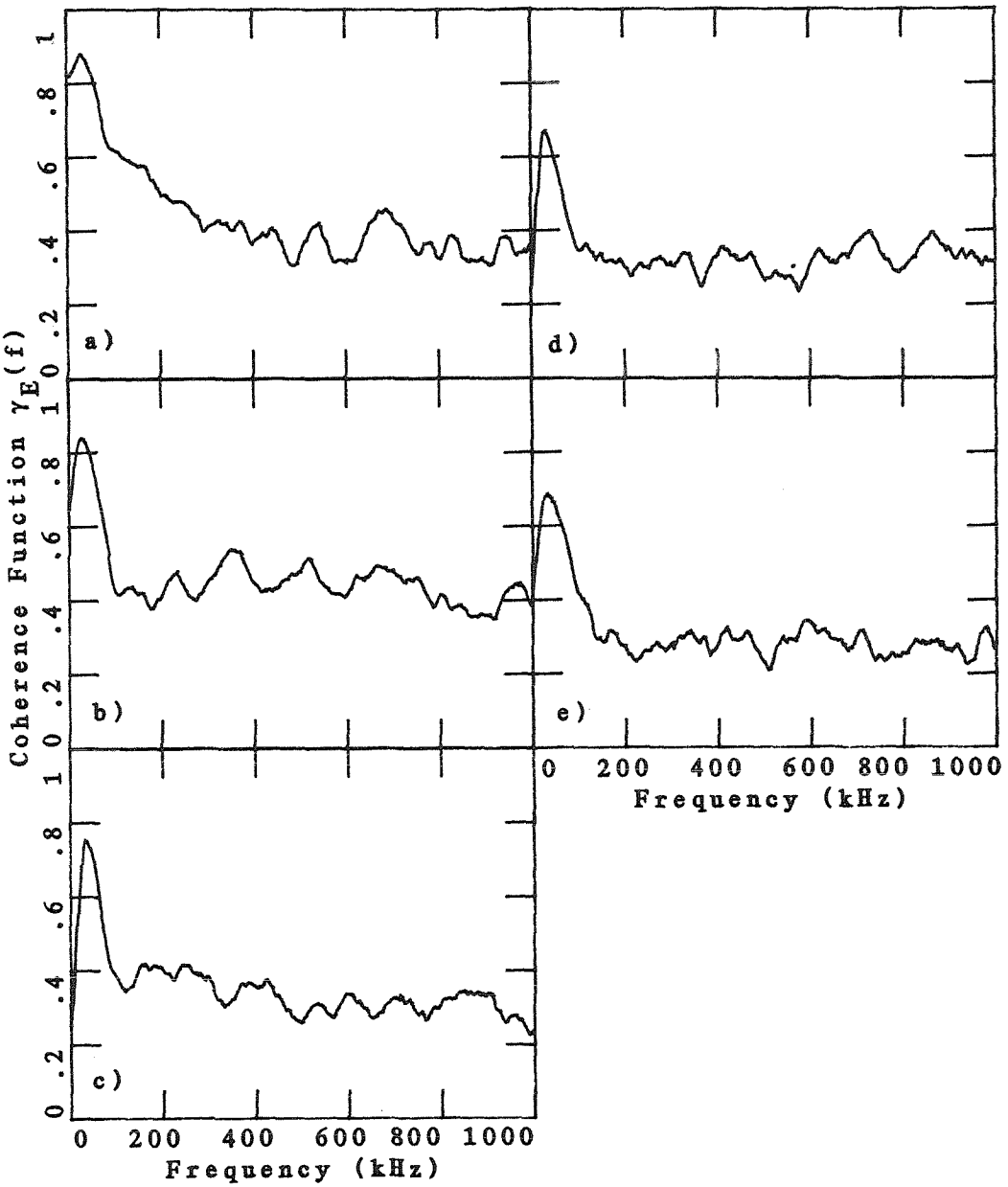

Figure 35. The coherence function for the radial component of signal from two probes separated poloidally a) .01 m, b) .02 m, c) .03 m, d) .04 m, and e) .05 m.

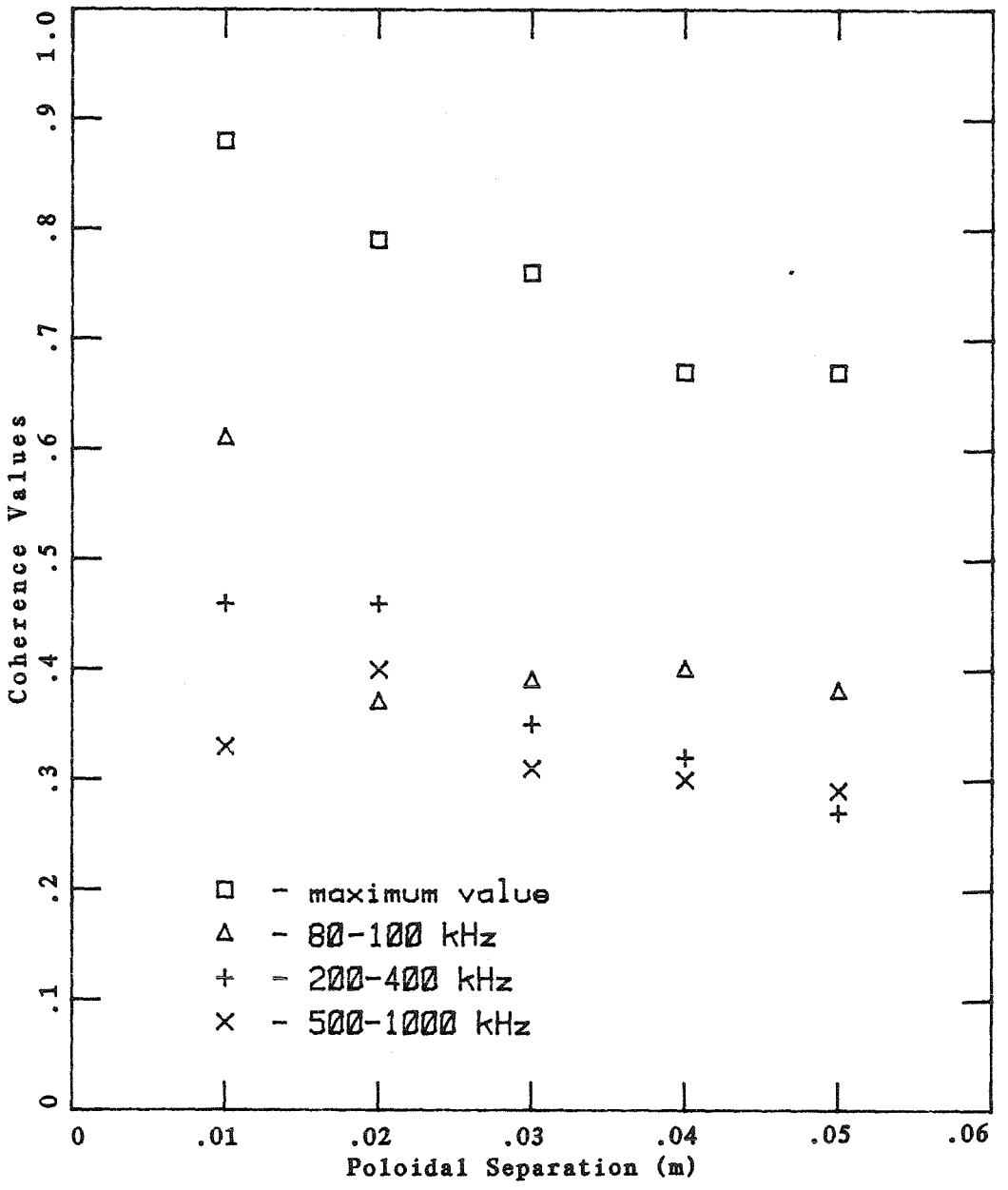

Figure 36. The coherence function values from various frequency bands from figure 35.

of .5 is taken as the separation between correlated and uncorrelated signals, then the 32 kHz peak is seen to be correlated for poloidal separations much greater than .05 m and can be described as a large-scale mode of the plasma. The frequency band near 100 kHz has a poloidal correlation length of approximately .015 m, while higher frequency signals decorrelate over a poloidal distance of less than .01 m. The behavior of the correlation function in figure 21 for cases with and without a low frequency mode present follows directly from the frequency dependence of the coherence function.

In figure 37, the phase of the 32 kHz mode is plotted versus poloidal separation. The scatter from a linear dependence is due to variability between discharges, as the phase for only one separation was measured per discharge. The slope of the line fit to the points corresponds to an apparent poloidal velocity of 5×10^3 m/sec in the electron diamagnetic drift direction. The electron diamagnetic drift velocity is approximately 3×10^3 m/sec. The $\underset{\sim}{E} \times \underset{\sim}{B}$ velocity, however, is not known. The linear dependence of the phase on separation supports the identification of the peak as a large-scale mode.

The coherence function for toroidal separation is shown in figure 38a. As in the poloidal separation case, the signal is well correlated only at low frequencies. The high frequency portion of the spectrum, which would be

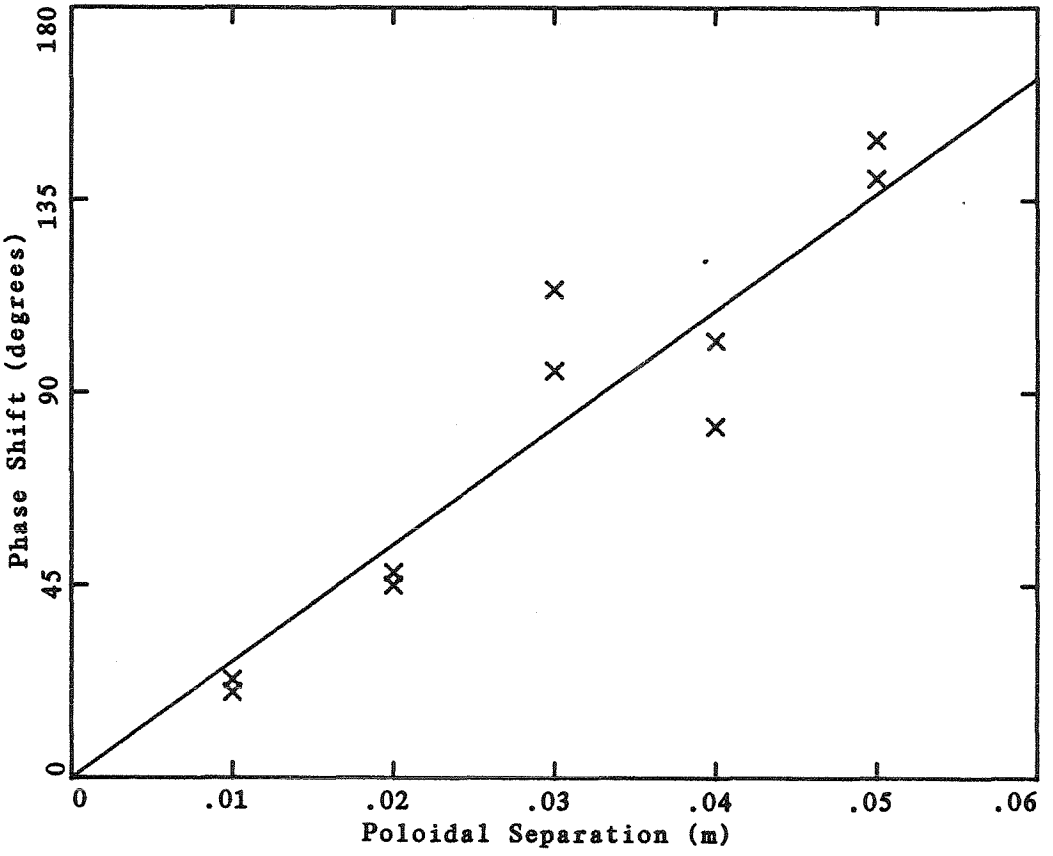

Figure 37. The phase at 32 kHz of the radial component of signals from the cross power spectral density for various discharges at the poloidal probe separations shown, .02 m from the wall. The straight line fit implies an apparent poloidal velocity in the electron diamagnetic drift direction of 4.2×10^3 m/sec.

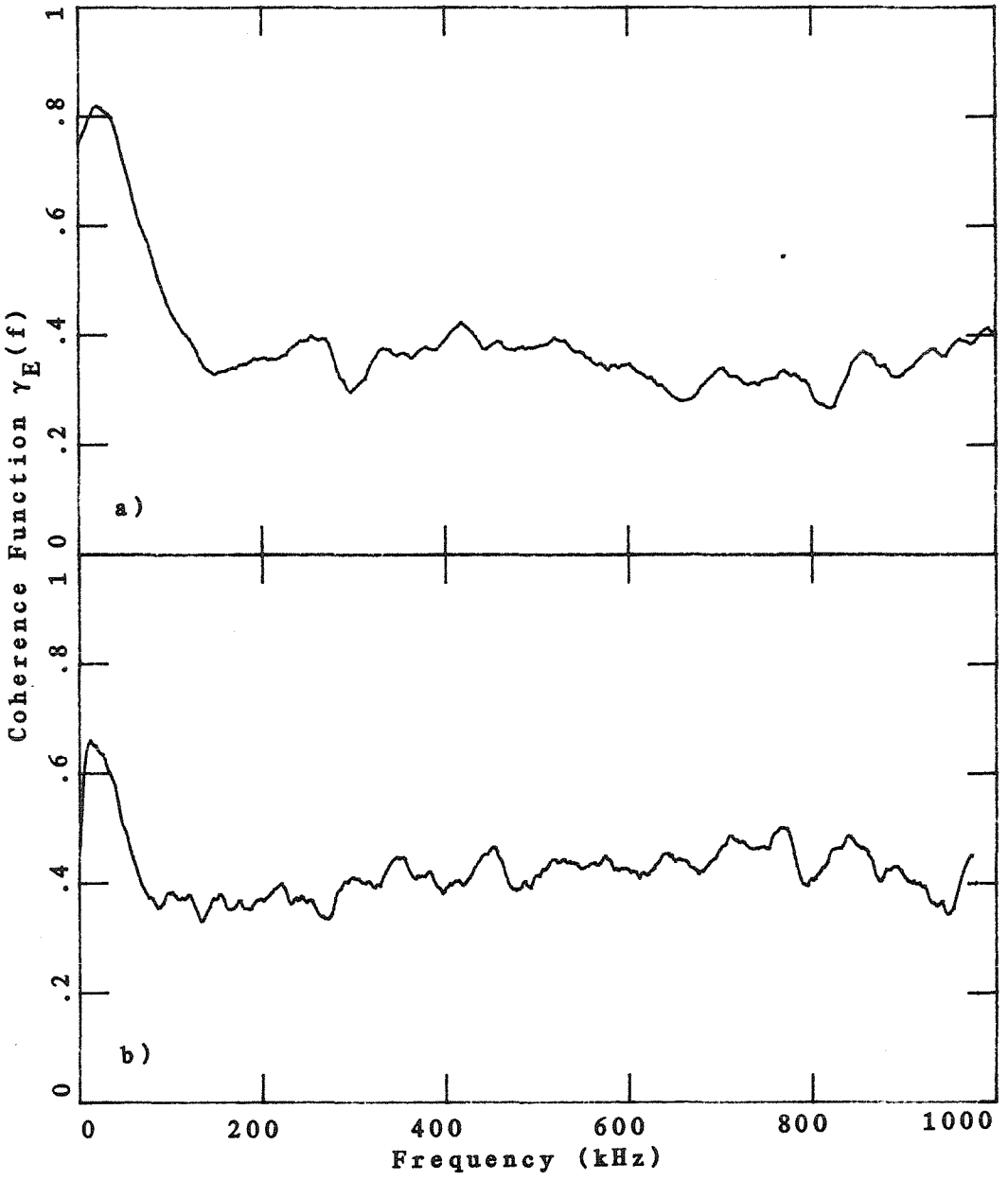

Figure 38. The coherence function for a) the radial component of signal from two probes separated toroidally .02 m from the wall, and b) the radial and poloidal components of fluctuating field at one point .02 m from the wall.

related to transport through stochastic field theory, shows no correlation. However, as was noted in the previous section, the measurements do not preclude longer toroidal correlation lengths than those observed since the probe alignment was not along the unperturbed field lines.

Figure 38b shows the coherence function for the case of two signals which are the radial and poloidal components of fluctuating field at the same spatial location. Again, the coherence is high at 25 kHz corresponding to a large peak in the amplitude spectrum. The phase at 25 kHz is approximately 90^{o}, indicating a coherent MHD mode. The higher frequencies are not well correlated.

VI. SUMMARY AND CONCLUSIONS

The results of the experimental survey of magnetic field fluctuations on BIGMAK are summarized in the following list.

1. δB_{rms}, the fluctuating field strength, is equal in the radial and poloidal directions, and is at least a factor of 5 less in the toroidal direction.
2. Assuming toroidal correlation lengths on the order of the major circumference of BIGMAK for the high frequency fluctuations, the fluctuating field strength is more than an order of magnitude too low to explain the observed anomalous electron thermal transport.
3. δB_{rms} decreases rapidly after the initial breakdown of the plasma, and continues to decrease slowly after 3 msec into the discharge.
4. δB_{rms} shows no dependence on I_p and q(a).
5. δB_{rms} increases as $\bar{n}_e$ increases during gas puffing and decreases as $\bar{n}_e$ decreases after the peak density is achieved.
6. The probability density function indicates the signals are noiselike in character.
7. The correlation function has a large peak for:
   a. poloidal separation of radial coils up to .05 m when a low frequency mode is present.
   b. poloidal separation of radial coils of $<.01$ m with no low frequency mode present.
   c. toroidal separation of radial coils when a low

frequency mode is present.

8. The correlation function does not have a large peak for:
   a. poloidal separation of radial coils >.01 m when no low frequency mode is present.
   b. toroidal separation of radial coils when no low frequency mode is present.
9. A mild correlation is observed when signals from a radial coil and a poloidal coil are correlated.
10. A shift in the peak of the correlation function with a low frequency mode present for poloidal separation of radial coils indicates a propagation of the disturbance in the direction of, and at approximately the magnitude of, the electron diamagnetic drift velocity.
11. The low frequency (<100 kHz) and high frequency (>100 kHz) fluctuations appear to be independent phenomena.
12. The low frequency fluctuations are dominated by large-scale coherent MHD modes which are well correlated in all spatial directions.
13. From the phase of the spectral density, the low frequency modes appear to propagate with a velocity near the electron diamagnetic drift velocity in the electron diamagnetic drift direction. The radial and poloidal components are 90^{o} out of phase with each other, as expected for MHD modes.
14. The coherence function for the high frequency fluctuations (>100 kHz) indicates correlation lengths

$\lesssim$.01 m in the poloidal direction and less than the separation between ports ($\pi R/4$ = .36 m) in the toroidal direction. No conclusions can be drawn from the measurements of radial correlation lengths due to the effects of the probe shield.

15. The dependence of δB_r and δB_θ on frequency is $f^{-\alpha}$ with α = 2 - 4. In most cases, α lies between 2.2 and 2.7.

16. The frequency dependence of δB_r and δB_θ is unaffected by changes in I_p, q(a), $\bar{n}_e$, and r. The amplitude in all frequency bands increases as $\bar{n}_e$ increases and as r is decreased.

It is of interest to compare the observed fluctuations to the theory of sources of fluctuations. The measurements of the low frequency fluctuations, as previously stated, are consistent with the presence of magnetic islands of low m and n numbers in BIGMAK. This is supported by the long correlation lengths in all directions, the apparent poloidal propagation in the electron diamagnetic drift direction, and the 90^o phase shift between the radial and poloidal components.

The comparison of the high frequency fluctuations to microtearing mode theory is not as straightforward. In the first approximation, the microtearing mode theory predicts unstable modes for frequencies below ν_{ei} with the maximum growth rate near $.1\nu_{ei}$ [19]. In BIGMAK, for typical parameters, ν_{ei} varies from approximately

300 kHz at r = 0 to 600 kHz near the edge. The maximum growth rate region of 30 kHz - 60 kHz overlaps the frequency range in which large-scale MHD modes are observed. The theory also does not predict the amplitude of the spectrum when the modes saturate. The observed spectrum also does not change appreciably during gas puffing even though ν_{ei} varies proportional to $\bar{n}_e$. A more careful study of microtearing modes on MACROTOR [64] indicated that the modes would be stable at low density and unstable at high density. Since the fluctuations were observed in both regimes, they were found not to be caused by microtearing modes.

The best fit to the observed spectra is provided by the statistical theory of Chu [21] as illustrated in figure 39. The parameter ω_T in equation 4.11 is computed according to the theory from τ_E, and the amplitude of the spectrum is adjusted to match the measured spectrum at 200 kHz. The dependence of δB_r on frequency in the range 300 kHz - 1 MHz is $f^{-2.8}$, in agreement with the measurement. It is also obvious from figure 39 that fluctuations other than the statistical fluctuations of this theory must dominate the low frequency regime.

Since the problem of anomalous electron thermal transport is a major problem in the confinement of plasmas for fusion power production, several suggestions for continued research are in order. The stochastic field theory diffusion coefficient depends strongly on the

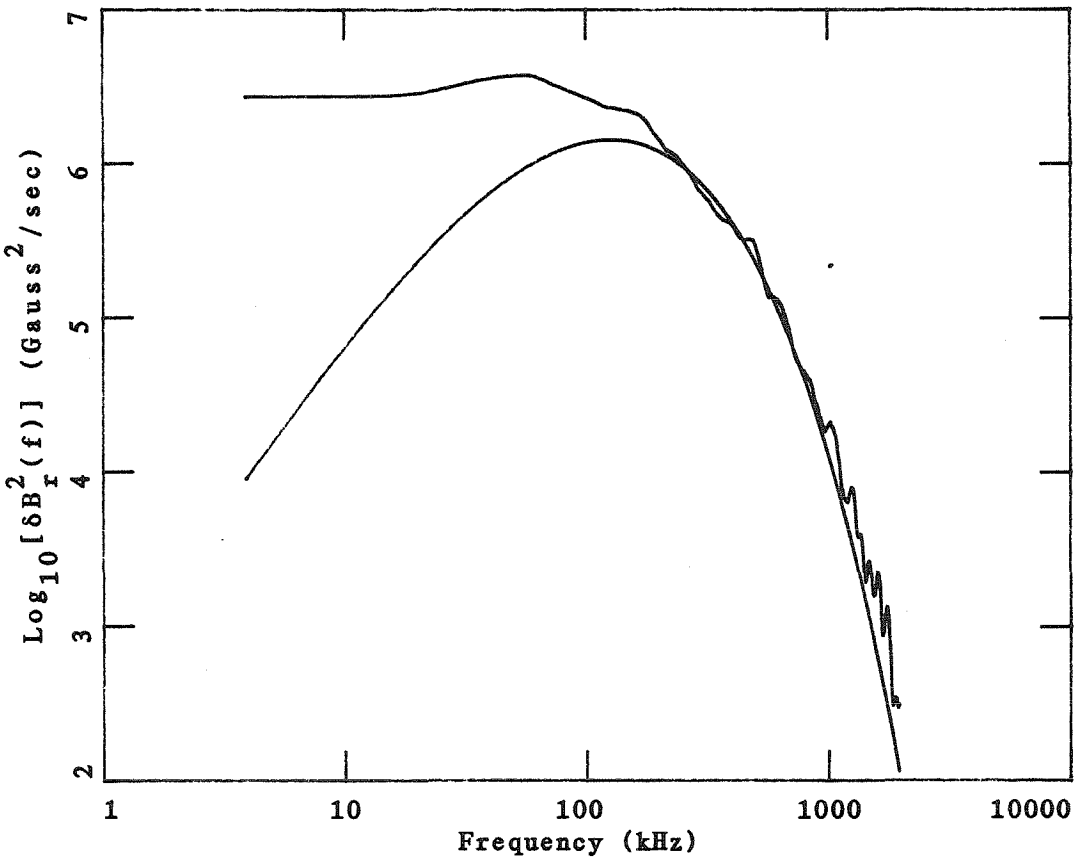

Figure 39. A typical spectral density amplitude of the radial component of signal and a theoretical fit from equation 4.11 from Chu [21] matched in amplitude at f = 200 kHz.

correlation length of the perturbations along the field lines. A more careful measurement could be made with appropriately constructed probes. These probes should be constructed so as to allow measurements for toroidal separations intermediate between the width of the ports and the distance between the ports.

A direct comparison of the stochastic field theory and the observed confinement time requires better measurements of parameters other than the fluctuating fields. The comparisons made in this thesis used typical plasma values for density, temperature, etc. To make a proper comparison, radial profiles of density, temperature, and radiation from the plasma must be known as well as the radial profiles of the fluctuating field strength and toroidal correlation length.

Finally, the magnetic fluctuations may be responsible for only a portion of the observed transport. One particularly interesting candidate to explain the observed diffusion may be poloidal electric field fluctuations which would lead to radial fluctuating $\underset{\sim}{E} \times \underset{\sim}{B}$ velocities for the plasma particles. Preliminary measurements of electric field fluctuations in BIGMAK show broadband fluctuations with a root mean square value near 1000 V/m at r = .13 m. The fluctuating δv_r is then roughly 2.5×10^3 m/sec compared to 4×10^2 m/sec computed from the fluctuating magnetic fields. A more careful study of the electric field fluctuations is certainly justified.

REFERENCES

1. Bishop, A.S., Project Sherwood (Addison-Wesley, Reading, Mass., 1958), passim.
2. Bateman, G., MHD Instabilities (MIT Press, Cambridge, Mass., 1978), passim.
3. Chen, F.F., Introduction to Plasma Physics (Plenum Press, New York, 1974), passim.
4. Boyd, T.J.M., and Sanderson, J.J., Plasma Dynamics (Barnes and Noble, New York, 1969), passim.
5. Rawls, J.M., ed., Status of Tokamak Research (U.S. Dept. of Energy, 1979), passim.
6. Apgar, E., et al.,IAEA-6,Vol. 1, (1977) p.247.
7. Gondhaleker, A., et al., "Study of the Energy Balance in Alcator," IAEA-7,Vol. 1, (1979) p.199.
8. Stix, T.H., "Magnetic Braiding in a Toroidal Plasma," Phys. Rev. Lett. 30, 833 (1973).
9. Rechester, A.B., and Stix, T.H., "Magnetic Braiding Due to Weak Asymmetry," Phys. Rev. Lett. 36, 587 (1976).
10. Rechester, A.B., and Rosenbluth, M.N., "Electron Heat Transport in a Tokamak with Destroyed Magnetic Surfaces," Phys. Rev. Lett. 40, 38 (1978).
11. Harvey, R.W., McCoy, M.G., Hsu, J.Y., and Mirin, A.A., "Electron Dynamics Associated with Stochastic Magnetic Fields," General Atomic Co. Report GA-A16114 (1980).
12. Callen, J.D., et al., "Plasma Transport and Impurity Behavior in the Edge and Divertor Regions of a Tokamak," Plasma Physics and Controlled Fusion Research

Eighth Conf. Proc., IAEA-CN-38/Y-3, Brussels (1980).

13. Rechester, A.B., and White, R.B., "Calculation of Turbulent Diffusion for the Chirikov-Taylor Model," Phys. Rev. Lett. 44, 1586 (1980).

14. Callen, J.D., "Drift-Wave Turbulence Effects on Magnetic Structure and Plasma Transport in Tokamaks," Phys. Rev. Lett. 39, 1540 (1977).

15. Ohkawa, T., "A Transport Model For Alcator Scaling in Tokamaks," General Atomic Co. Report GA-A14433 (1977).

16. Hirshman, S.P., and Molvig, K., "Turbulent Destabilization and Saturation of the Universal Drift Mode in a Sheared Magnetic Field," Phys. Rev. Lett. 42, 648 (1979).

17. Molvig, K., Hirshman, S.P., and Whitson, J.C., "Finite-β_e Universal-Mode Turbulence and Alcator Scaling," Phys. Rev. Lett. 43, 582 (1979).

18. Fussmann, G., Green, B.J., and Zehrfeld, H.P., "The Magnetic Field of Toroidal Helical Surface Currents and its Effect on Island Formation and Ergodization in Tokamaks," Plasma Physics and Controlled Fusion Research Eighth Conf. Proc., IAEA-CN-38/M-1-3, Brussels (1980).

19. Drake, J.F., Gladd, N.T., Liu, C.S., and Chang, C.L., "Microtearing Modes and Anomalous Transport in Tokamaks," Phys. Rev. Lett. 44, 994 (1980).

20. Dominguez, R.R., Rosenberg, M., and Chang, C.S., "Nonlinear theory of high-m tearing modes," Phys.

Fluids 24, 472 (1981).

21. Chu, C., "Magnetic Spectra and Electron Transport of Current Carrying Plasmas," General Atomic Co. Report GA-A16320 (1981).
22. Liewer, P.C., "A Survey of Fluctuation Measurements in Tokamaks and Comparison with Various Theories of Anomalous Electron Transport," presented at the Annual Controlled Fusion Theory Conference, Austin, Texas, April 8, 1981
23. Drake, J.F., and Lee, Y.C., "Nonlinear Evolution of Collisionless and Semicollisional Tearing Modes," Phys. Rev. Lett. 39, 453 (1977).
24. Chen, L., Rutherford, P.H., and Tang, W.M., "Drift-Modified Tearing Instabilities Due to Trapped Electrons," Phys. Rev. Lett. 39, 460 (1977).
25. Gladd, N.T., Drake, J.F., Chang, C.L., and Liu, C.S., "Electron temperature gradient driven microtearing mode," Phys. Fluids 23, 1182 (1980).
26. Biskamp, D., and Welter, H., "Coalescence of Magnetic Islands," Phys. Rev. Lett. 44, 1069 (1980).
27. Zweben, S.J., and Taylor, R.J.,"Filtered and Unfiltered Vacuum Photodiode Detectors for VUV Monitoring of Tokamak Plasmas," UCLA Report PPG-451 (1980).
28. Bendat, J.S., and Pierso., A.G., Random Data: Analysis and Measurement Procedures (Wiley-Interscience, New York, 1971), passim.
29. Blackman, R.B., and Tukey, J.W., The Measurement of

Power Spectra (Dover, New York, 1958), passim.

30. Brigham, E.O., The Fast Fourier Transform (Prentice-Hall, Englewood Cliffs, New Jersey, 1974), passim.
31. Mazzucato, E., "Small-Scale Density Fluctuations in the Adiabatic Toroidal Compressor," Phys. Rev. Lett. 36, 792 (1976).
32. Mazzucato, E., "Low-frequency microinstabilities in the PLT tokamak," Phys. Fluids 21, 1063 (1978).
33. Surko, C.M., and Slusher, R.E., "Study of the Density Fluctuations in the Adiabatic Toroidal Compressor Tokamak Using CO_2 Laser Scattering," Phys. Rev. Lett. 37, 1747 (1976).
34. Slusher, R.E., and Surko, C.M., "Study of Density Fluctuations in the Alcator Tokamak Using CO_2 Laser Scattering," Phys. Rev. Lett. 40, 400 (1978).
35. Surko, C.M., and Slusher, R.E., "Study of plasma density fluctuations by the correlation of crossed CO_2 laser beams," Phys. Fluids 23, 2425 (1980).
36. Semet, A., Mase, A., Peebles, W.A., Luhmann, Jr., N.C., and Zweben, S., "Study of Low-Frequency Microturbulence in the Microtor Tokamak by Far-Infrared Laser Scattering," Phys. Rev. Lett. 45, 445 (1980).
37. TFR Group, "TFR Experiments on Superbanana Particle Diffusion, Small Scale Turbulence and Transport," Plasma Physics and Controlled Fusion Research Eighth Conf. Proc., IAEA-CN-38/N-5, Brussels (1980).

38. Johnson, J.L., Oberman, C.R., Kulsrud, R.M., and Frieman, E.A., IAEA Geneva Conf., 31, 198 (1958).

39. Suydam, B.R., IAEA Geneva Conf., 31, 157 (1958).

40. Kadomtsev, B.B., Reviews of Plasma Physics 2 (Plenum, New York, 1966), p.153.

41. Shafranov, V.D., Sov. Phys. - Tech. Phys. 15, 175 (1970).

42. Lowder, R.S., and Thomassen, K.I., "Model of kink modes and their feedback stabilization," Phys. Fluids 16, 1497 (1973).

43. Goedbloed, J.P., and Sakanaka, P.H., "New Approach to magnetohydrodynamic stability: I. A practical stability concept," Phys. Fluids 17, 908 (1974).

44. Furth, H.P., Killeen, J., and Rosenbluth, M.N., "Finite-Resistivity Instabilities of a Sheet Pinch," Phys. Fluids 6, 459 (1963).

45. Furth, H.P., Rutherford, P.H., and Selberg, H., "Tearing mode in the cylindrical tokamak," Phys. Fluids 16, 1054 (1973).

46. Glasser, A.H., Furth, H.P., and Rutherford, P.H., "Stabilization of Resistive Kink Modes in the Tokamak," Phys. Rev. Lett. 38, 234 (1977).

47. Hastie, R.J., Sykes, A., Turner, M., and Wesson, J.A., "Stabilization of Tearing Modes in Tokamaks," Nuc. Fusion 17, 515 (1977).

48. Rutherford, P.H., "Nonlinear growth of the tearing mode," Phys. Fluids 16, 1903 (1973).

49. White, R.B., Monticello, D.A., Rosenbluth, M.N., and Waddell, B.V., "Saturation of the tearing mode," Phys. Fluids 20, 800 (1977).

50. Biskamp, D., and Welter, H., IAEA 1, 579 (1976).

51. Finn, J.M., "Coupling of tearing modes in tokamaks," Phys. Fluids 20, 1749 (1977).

52. Wesson, J.A., "Finite Resistivity Instabilities of a Sheet Pinch," Nuc. Fusion 6, 130 (1966).

53. Barston, E.M., "Stability of the Resistive Sheet Pinch," Phys. Fluids 12, 2162 (1969).

54. Rutherford, P.H., and Furth, H.P., Princeton Plasma Physics Laboratory Report MATT-872 (1971).

55. Mirnov, S.V., and Semenov, I.B., "Investigation of the Instabilities of the Plasma String in the Tokamak-3 System by means of a Correlation Method," Sov. J. of Atomic Energy, 30, 22 (1971).

56. Ware, A.A., IAEA Salzburg Conf. 1961, Nuclear Fusion Supplement part 3, 869 (1962).

57. Glasser, A.H., Greene, J.M., and Johnson, J.L., "Resistive instabilities in a tokamak," Phys. Fluids 19, 567 (1976).

58. Makishima, K., Tominaga, T., Tohyama, H., and Yoshikawa, S., "Simultaneous Measurements of the Plasma Current Profile and Instabilities in a Tokamak," Phys. Rev. Lett. 36, 142 (1976).

59. Hutchinson, I.H., "Magnetic Probe Investigation of the Disruptive Instability in Tokamak LT-3," Phys. Rev.

Lett. 37, 338 (1976).

60. Robinson, D.C., and McGuire, K., "Magnetic Islands and Disruptions in the Tosca Tokamak," Nuc. Fusion 19, 115 (1979).

61. Fredrickson, E.D., and Bellan, P.M., "Observation of Magnetic Islands in the ENCORE Tokamak," Bull. Am. Phys. Soc. 25, 901 (1980).

62. Zweben, S.J., Menyuk, C.R., and Taylor, R.J., "Small-Scale Magnetic Fluctuations Inside the Macrotor Tokamak," Phys. Rev. Lett. 42, 1270 (1979).

63. Zweben, S.J., and Taylor, R.J., "Phenomenological Comparison of Magnetic and Electrostatic Fluctuations in the Macrotor Tokamak," Nuc. Fusion 21, 193 (1981).

64. Liewer, P.C.,"Comparison of Experimental and Theoretical Magnetic Fluctuation Spectra for the Macrotor Tokamak," Bull. Am. Phys. Soc. 25, 847 (1980).